JYU DISSERTATIONS 649

Heidi Rytkönen

Simulated π^0–π^0 Correlation and Test Beam Performance of the Future Forward Calorimeter in the ALICE Experiment

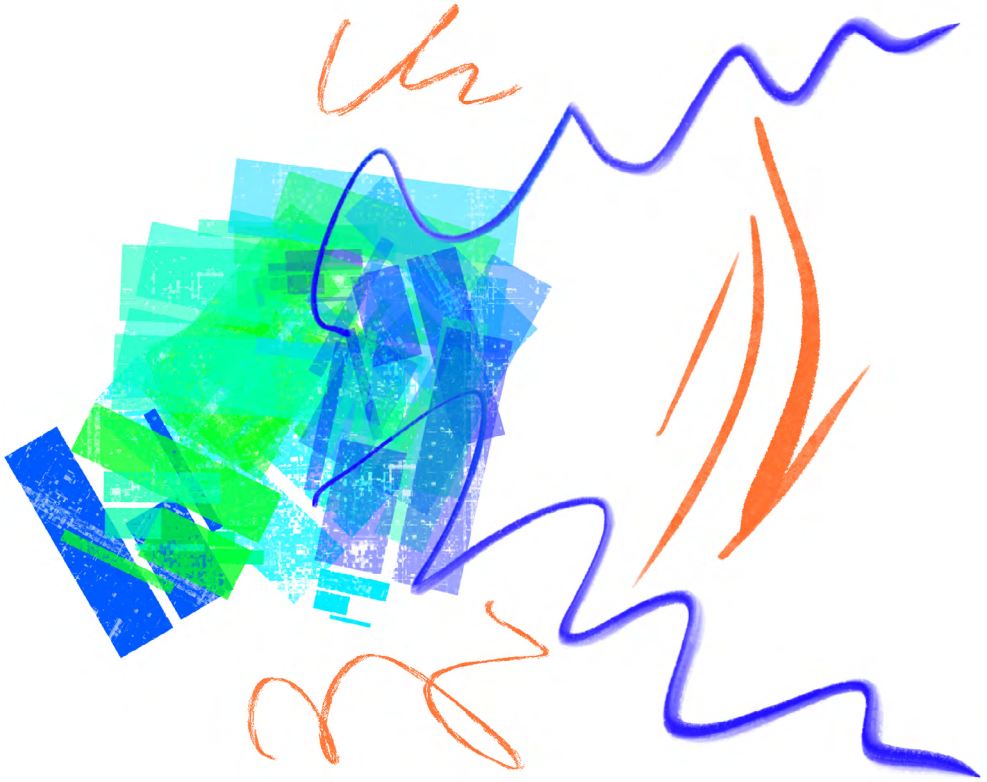

UNIVERSITY OF JYVÄSKYLÄ
FACULTY OF MATHEMATICS
AND SCIENCE

JYU DISSERTATIONS 649

Heidi Rytkönen

Simulated π^0–π^0 Correlation and Test Beam Performance of the Future Forward Calorimeter in the ALICE Experiment

Esitetään Jyväskylän yliopiston matemaattis-luonnontieteellisen tiedekunnan suostumuksella
julkisesti tarkastettavaksi Ylistönrinteen auditoriossa FYS1
toukokuun 26. päivänä 2023 kello 12.

Academic dissertation to be publicly discussed, by permission of
the Faculty of Mathematics and Science of the University of Jyväskylä,
in Ylistönrinne, auditorium FYS1, on May 26, 2023, at 12 o'clock.

JYVÄSKYLÄN YLIOPISTO
UNIVERSITY OF JYVÄSKYLÄ

JYVÄSKYLÄ 2023

Editors
Ilari Maasilta
Department of Physics, University of Jyväskylä
Päivi Vuorio
Open Science Centre, University of Jyväskylä

Cover picture by Heidi Rytkönen.

ISBN 978-951-39-9618-5 (PDF)
URN:ISBN:978-951-39-9618-5
ISSN 2489-9003

Permanent link to this publication: http://urn.fi/URN:ISBN:978-951-39-9618-5

ABSTRACT

Rytkönen, Heidi
Simulated π^0–π^0 Correlation and Test Beam Performance of the Future Forward Calorimeter in the ALICE experiment

Since the start of Large Hadron Collider (LHC) particle collisions in 2008 all LHC experiments have provided data to understand the interactions between the fundamental particles. Out of the LHC experiments ALICE (A Large Ion Collider Experiment) is the dedicated heavy ion experiment, focusing on the study of Quark-Gluon Plasma (QGP) formed in the collisions between heavy ions.

After extensive upgrade efforts to the detector setup to withstand the conditions set by the increased particle beam luminosity for the next physics run (Run 3), the ALICE experiment started collecting data again in 2022. After Run 3 there will be another upgrade that will include replacing the three innermost layers in the inner tracking system with a more precise tracker (ITS3) and adding a new forward calorimeter (FoCal) to the experiment. FoCal extends the physics analyses to the forward rapidities (near beam pipe) and includes the gluon saturation physics to the ALICE physics program. The gluon saturation is expected happen at low gluon momenta but it has not been observed experimentally yet. FoCal is expected to probe the saturation region and provide constraints to the theory calculations related to gluon distributions going near the saturation limit.

In this thesis, I present the performance characterization of FoCal silicon pad sensors from two first FoCal test beams carried on during 2021 and 2022. For the main analysis in this thesis I have simulated the physics performance of π^0–π^0 correlations measured in FoCal. In addition, simulation results regarding the event plane performance of Fast Interaction Trigger (FIT), the new forward trigger installed for Run 3 are presented. The event plane is an estimator for the heavy ion collision reaction plane and is provided by FIT Run 3 onwards.

Keywords: The ALICE experiment, neutral pion correlations, Forward Calorimeter, Fast Interaction Trigger

TIIVISTELMÄ (ABSTRACT IN FINNISH)

Large Hadron Collider (LHC) on tuottanut dataa hadronien ja raskaiden ionien törmäyksistä vuodesta 2008 lähtien. Suurien LHC-kokeiden analyysit törmäyksistä ovat auttaneet ymmärtämään paremmin hadronien välisiä vuorovaikutuksia. Kokeista ALICE (A Large Ion Collider Experiment) on rakentanut fysiikkaohjelmansa erityisesti raskasionitörmäysten tutkimukselle. Raskasionitörmäyksissä muodostuu kuumaa kvarkki-gluoni plasmaa (QGP), joka täytti maailmankaikkeuden sen ensimmäisten mikrosekuntien aikana.

ALICE-kokeen laitteisto kävi läpi suuren päivityksen, koska LHC kasvatti tuottamiensa hiukkassuihkujen luminositeettia seuraavalle ajoperiodilleen (ajo 3), joka alkoi 2022. Päivitys oli tarpeen, jotta laitteistoon kuuluvat ilmaisimet pystyisivät vastaanottamaan suuremman määrän törmäyksiä ja siten myös dataa. Kolmannen fysiikka-ajon jälkeen ALICE:een on tulossa seuraava päivitys kahden uuden hiukkasilmaisimen muodossa. Nykyisen ITS:n (Inner Tracking System) kolme sisintä kerrosta korvataan uutta teknologiaa hyödyntävällä ITS3:lla ja kokeeseen asennetaan etusuunnan kalorimetri FoCal. FoCal mahdollistaa fysiikka-analyysien laajentamisen etusuuntaan ja tuo ALICE:n fysiikka-ohjelmaan mukaan gluonien saturaatiofysiikan. Gluonien saturaationa tunnettua ilmiötä ei olla vielä vahvistettu kokeellisesti. FoCal ylettyy mittauksissaan niille kinemaattisille alueille, jossa saturaation odotetaan olevan havaittavissa. Nämä mittaukset tarjoavat myös rajoituksia gluonien jakaumia ennustaville teorialaskuille.

Tähän väitöskirjaan olen koonnut testimittaus- ja simulaatioanalyysejä liittyen FoCal:in suorituskyvyn tutkimiseen. Vuonna 2021 ja 2022 järjestetyissä mittauksissa testasimme FoCal:in sensorien toimintaa ja tässä esitelty tekemäni data-analyysi liittyy FoCal:in elektromagneettisen kalorimetrin silikonisensorien karakterisointiin. Fysikaalisiin tavoitteisiin liittyen FoCal:in kykyä mitatta neutraalien pionien korrelaatioita. Suuri osa tästä analyysista liittyy korrelaatioihin liittyvän taustan tutkimiseen ja taustanpoistomenetelmien kehittämiseen. Lisäksi työpanokseni liittyen ALICE:n uuden FIT-ilmaisimen (Fast Interaction Trigger) kykyyn mitata arvio raskasionitörmäysten törmäystasolle on sisällytetty tähän kirjaan.

Author

Heidi Rytkönen
Department of Physics
University of Jyväskylä
Finland

Supervisors

Dr. Sami Räsänen
Department of Physics
University of Jyväskylä
Finland

Dr. Norbert Novitzky
Oak Ridge National Laboratory
USA

Dr. DongJo Kim
Department of Physics
University of Jyväskylä
Finland

Reviewers

Dr. Astrid Morreale
U.S. Department of Energy (DOE)
USA

Prof. Saskia Mioduszewski
Texas A&M
USA

Opponent

Dr. Gabor David
Brookhaven National Laboratory
USA

PREFACE

I started to work towards the dissertion in 2018 and these years have been eventful. Though the work has been quite independent this thesis would not have been possible without others. Therefore here I want to show my appreciation to people who have helped me to achieve this goal.

Firstly, my deepest graditude goes to my supervisor Sami Räsänen. Your guidance has been everything and I've always appreciated your patience and the easiness to talk with you about anything. Whenever I was doubtful about the research, a discussion with you always helped to move forward and boost my motivation. I thank Norbert Novitzky for the invaluable help with the pad analysis; without you this thesis would definitely be one chapter shorter. I also want to express my gratitude to DongJo Kim for the guidance in the thesis work, from helping me to structure codes and thesis to discussions about the topics. I also thank pre-reviewers Astrid Morreale and Saskia Mioduszewski for the insightful comments and questions I received.

The people I've had pleasure to meet and work with at the university and CERN have given me a lot of perspective to life, thank you. I thank the people of FoCal and FIT collaborations whose output has been essential for this thesis. Special thanks goes to the ALICE juniors in our group; Oskari, Anna, Andreas, Laura, Maxim, Cindy and Hadi. I appreciate all the support I've gotten from you, and the good laughs and discussions we've had in the office and outside of it.

I thank my family and friends, even though the past couple of years have been challenging I feel lucky to have you in my life. I'm thankful to the group in which I started my studies years ago, naisfyysikot/fyysiot, I've had many great adventures and evening gatherings with you. We've done many activities (e.g. the 'running-in-the-woods-like-blind-chickens') together and I hope that will continue for the years to come. Last but not least, I would've not been able to push this through without Joni Tanttu, I'm grateful to have you in my life. Kiitos teille kaikille.

I acknowledge Vilho, Yrjö and Kalle Väisälä fund, which funded this work for three years, and University of Jyväskylä through Center of Excellence in Quark Matter and Helsinki Institute of Physics (HIP) for the additional funding. My graditude goes also to the CSC - IT Center for Science which provided the computational resources for the simulations presented in this thesis.

In Jyväskylä, May 2023

CONTENTS

ABSTRACT
TIIVISTELMÄ (ABSTRACT IN FINNISH)
PREFACE
CONTENTS

1 INTRODUCTION 1
1.1 Heavy Ion Physics 2
1.2 Gluon Saturation 8

2 ALICE UPGRADES 11
2.1 ALICE Run 3 upgrade 11
2.2 ALICE beyond Run 3 15
2.3 FoCal 16
2.3.1 Physics observables 18

3 FIT EVENT PLANE PERFORMANCE 25
3.1 Collision geometry 25
3.2 Event plane determination methods 27
3.2.1 Q-vector corrections 29
3.3 Simulations 31
3.4 Results 33
3.4.1 Recovery of elliptic flow v_2 35
3.4.2 Effect of dead channels on FT0 event plane performance 35

4 FOCAL TEST BEAMS 38
4.1 Calorimeter characterization 38
4.1.1 Minimum Ionizing Particle 41
4.1.2 Energy resolution 42
4.2 FoCal readout 44
4.3 Analysis procedure 46
4.3.1 Pedestal and noise removal 46
4.3.2 Clusterization 47
4.3.3 Simulation 47
4.4 Results 48
4.4.1 2021 SPS test beam 49
4.4.2 2022 PS test beam 55

5 FOCAL PERFORMANCE IN π^0–π^0 CORRELATIONS 63
5.1 Neutral pion reconstruction & reconstruction efficiency 65
5.1.1 Geometrical efficiency 67
5.1.2 Detector efficiency 68
5.1.3 Event mixing 71
5.2 Background subtraction 72
5.2.1 Asymmetry cut 72

5.2.2 Sideband method 75
5.2.3 Sideband method validation in pp and pPb..... 79
5.2.4 Low mass background..... 84
5.3 FoCal performance on π^0–π^0 correlation 85

6 SUMMARY 90

BIBLIOGRAPHY 92

Appendices 101

APPENDIX A VOLTAGE SCAN RESULTS (2022 TEST BEAM) 103

APPENDIX B POSITION SCAN RESULTS (2022 TEST BEAM) 105

APPENDIX C ELECTRON SHOWERS LAYER-BY-LAYER (2022 TEST BEAM) 109

1 INTRODUCTION

The most fundamental parts of the universe are the elementary particles. Seemingly simple everyday phenomena such as electricity and sunlight can be traced back to the interactions between them. Together they are the basis of the Standard Model of particle physics, a theory that describes the three known forces in nature: strong, electromagnetic, and electroweak interaction. The fourth force, gravity, is successfully described at large scales by the general relativity but cannot be explained in the current Standard Model framework. The discovery of the Higgs boson in 2012 [1, 2] after almost 50 years of its initial prediction by the Standard Model was the landmark in validation of the theory.

The building blocks of the Standard Model are presented in Figure 1. The particles can be divided into different groups based on their relations with each other and the forces they expe-

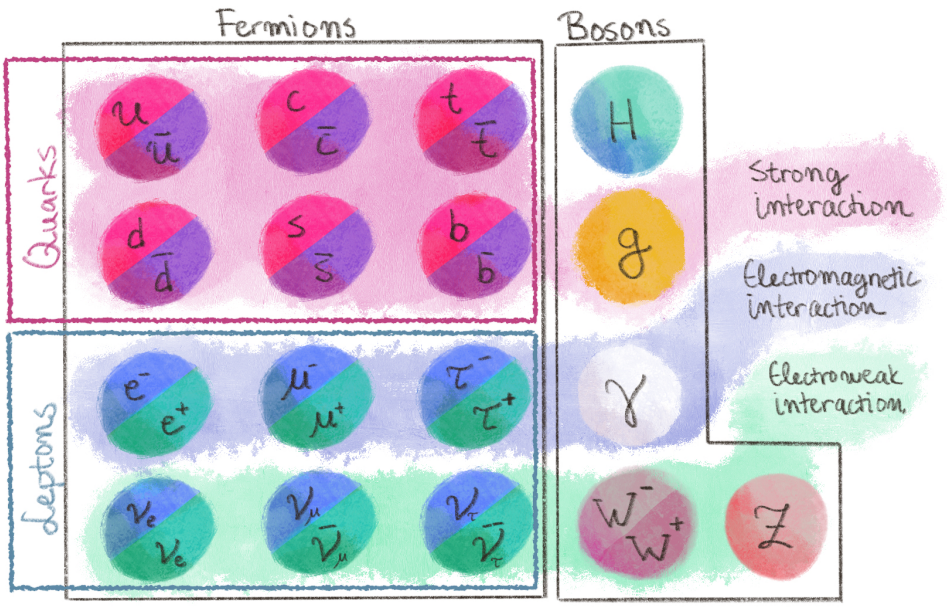

FIGURE 1 Elementary particles that are currently part of the Standard Model, with their antiparticles. The three forces mediated by the gauge bosons (gluon, photon, and $W^{\pm}$ and Z bosons) to the particles are indicated by colored areas. The existence of the Higgs boson explains why particles have a mass.

rience. The topics in this thesis revolve around strong interaction i.e. the interactions between quarks and gluons, together referred to as partons. Unlike other elementary particles, partons do not exist freely but form bound states, hadrons. However, in extreme conditions the bounds can be broken and partons can roam as free particles, forming strongly interacting Quark-Gluon Plasma (QGP). These kinds of conditions were dominating in the early universe: during the first microseconds the universe was filled with QGP. The formation of QGP in laboratory conditions is possible through heavy ion collisions and since its discovery, the experiments together with theory have improved our understanding of the mechanisms behind the strong interaction.

1.1 Heavy Ion Physics

Strong interaction is described by Quantum Chromo Dynamics (QCD), a gauge theory that successfully explains the interactions between quarks and gluons by introducing the concept of color charge [4]. Direct evidence of the color charge comes from the measurement of the ratio of cross sections from electron-positron annihilation $R = \sigma(e^+e^- \rightarrow hadrons) / \sigma(e^+e^- \rightarrow \mu^+\mu^-)$ [5] and measurement of $\pi^0 \rightarrow \gamma\gamma$ decay width [6, 7]. These measurements support the argument that quarks possess an additional quantum number of three possible values. The color charge can be thought analogous to the electric charge in QED but instead of negative and positive values, there are three colors ('red', 'blue', and 'green') and three anti-colors. Interaction between partons is based on the exchange of color via gluon that itself also carries color. For that reason gluons can interact directly with other gluons, contrary to photons, mediators of the electromagnetic charge.

QCD is a complex theory to solve directly, even for a proton, and for that reason approximation schemes such as perturbative QCD (pQCD) [8] at high energies are needed to perform the

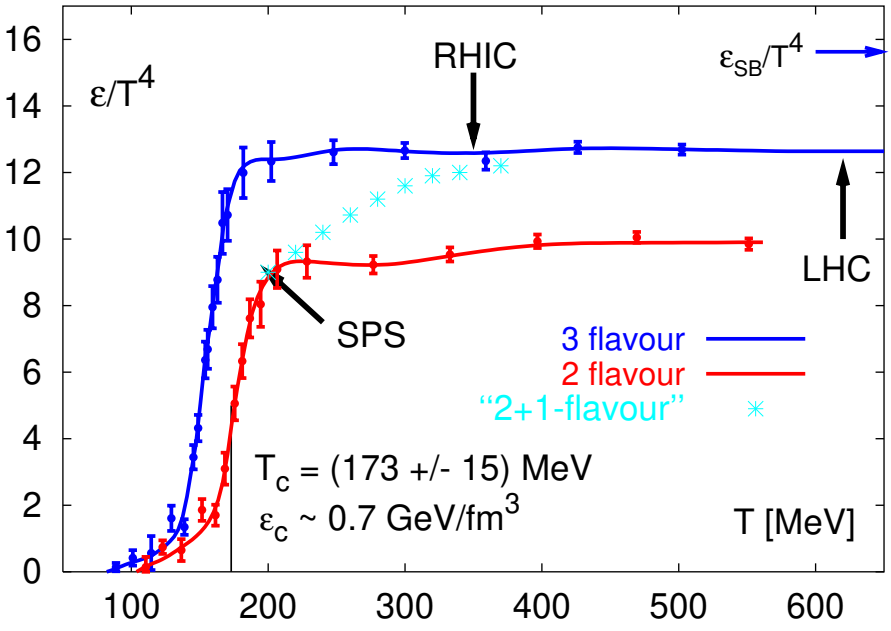

FIGURE 2 Lattice QCD prediction for energy density, as a function of temperature. Reprinted with permission from [3], 2009, Springer.

calculations. The situation gets more complicated when nuclei containing several protons and neutrons are considered. At large densities, which can be achieved by colliding heavy ions together, the quarks and gluons inside these systems can exist freely as a very low-viscosity fluid, QGP. The necessary conditions for the phase transition to happen are calculated via lattice QCD, non-perturbative calculations in which QCD is formulated in discrete Euclidean space-time points [9]. Figure 2 shows results of such a calculation [10]. The phase transition from hadronic gas to fluid takes place around critical temperature T_c where a sharp increase in energy density can be observed.

The phase diagram of QGP in relation to baryon chemical potential can be seen in Figure 3. At large μ_B where the quark/anti-quark imbalance is large, it is predicted that QGP becomes superconductive. Only neutron stars could provide such densities that matter in this phase could exist [11, 12]. The low μ_B can be accessed by colliding heavy ions together, as is done at Relativistic Heavy Ion Collider (RHIC) in Brookhaven National Laboratory (BNL) in the US and at Large Hadron Collider (LHC) in CERN Switzerland. With lower beam energies, RHIC Beam Energy Scan (BES) program has focused on scanning the phase diagram around the assumed critical point [13]. LHC reaches larger energies which corresponds to the lower μ_B in the phase diagram. Altogether the phase transition is not fully understood and in addition to LHC and RHIC, there are other facilities (e.g. FAIR, Facility for Antiproton and Ion Research [14]) having programs to explore it further.

The different stages of a heavy ion collision can be seen in Figure 4. The phases are presented here based on reference [15], from which a more detailed review can be found. When the heavy ion beams are accelerated to have nearly the speed of light the nuclei shape is a flat disk due to Lorentz contraction. In the pre-equilibrium stage, partonic level collisions take place. After

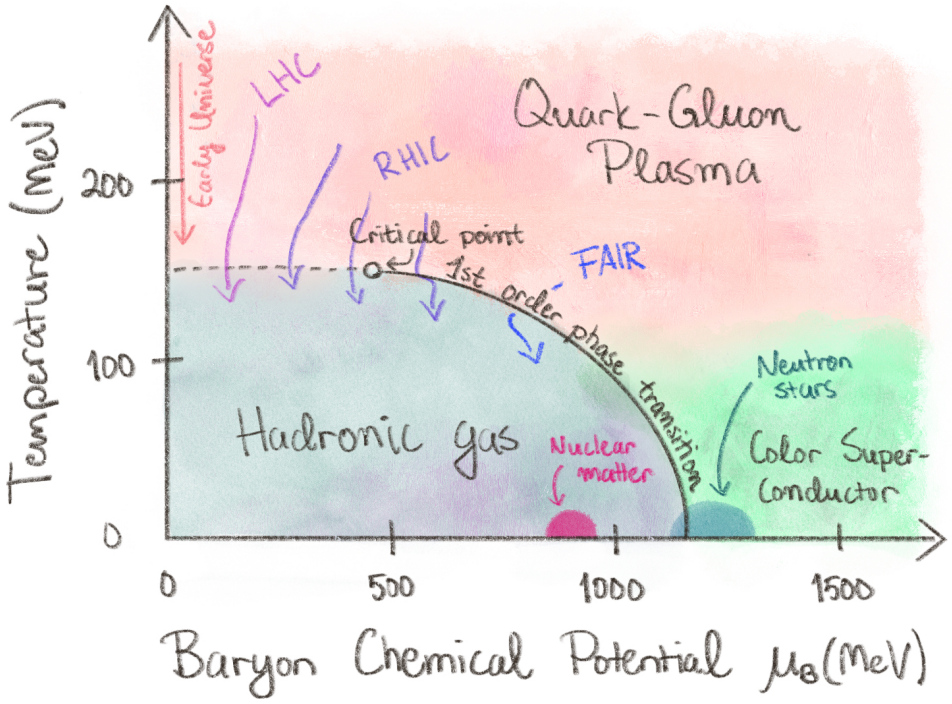

FIGURE 3 The phase diagram for Quark-Gluon Plasma. Colliders such as LHC and RHIC can be used to study the phase transition at low μ_B while neutron stars could provide useful information to better understand the phase diagram at higher chemical potentials.

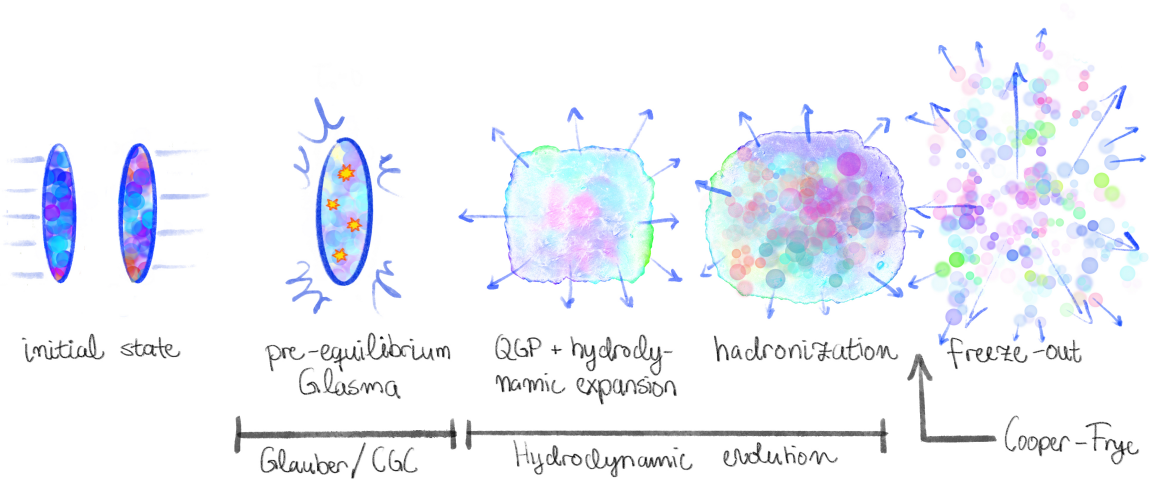

FIGURE 4 The stages of heavy ion collision include the initial state from which the pre-equilibrium and hydrodynamic expansion of QGP can be derived. After the expansion hadronization will take place and quarks and gluons will again form hadrons.

the pre-equilibrium stage, the system will reach local thermodynamical equilibrium which then leads to the formation of QGP and hydrodynamic expansion. The partons are deconfined and act as a collective fluid during this stage. Due to the expansion density decreases which leads to the cooldown of the system. When the system has cooled down to the critical temperature hadronization will take place. In this stage hadrons are formed through recombination and fragmentation of the partons. Then the evolution will continue to a point where the abundances of the hadrons born from the collision stay fixed (chemical freeze-out) and will lead to a state where the system is not in thermal equilibrium any more (kinematic freeze-out). How the QGP fluid is then broken into different particle species in the freeze-out is determined by Cooper-Frye formula [16]. After the freeze-out, the final state particles, including resonance decays, will continue to travel through space with the momentum they have gained from the collision.

The final state particles are our key to experimentally research the different stages of the collision. Compelling evidence for QGP and its fluidic nature comes from the measured azimuthal distribution of different final state particle species. The distribution is anisotropic and can be described as Fourier series [17]

$$\frac{\mathrm{d}N}{\mathrm{d}\phi} \propto 1 + 2\sum_{n=1}^{\infty} v_n \cos\left[n(\phi - \psi_n)\right], \tag{1}$$

where the sum is calculated over different harmonics starting from $n = 1$. Flow coefficients v_n represent the strength of the nth component while ψ_n the nth symmetry plane. The different anisotropies are a result of the collision geometry. The second harmonic v_2 is produced due to the elliptic shape of the overlapping region in the collision. The odd harmonics such as v_3 and v_5 are generated by event-by-event fluctuation in the nucleon placement inside the heavy ions [18]. In the case of flow low order harmonics, v_n exhibit linear correlation to the initial state anisotropies (described by eccentricities ε_n) but non-linear modes start to become important already at $n = 4$ [19, 20].

The flow coefficients, especially the second harmonic that is usually referred to as elliptic flow, have been measured extensively at RHIC in $\sqrt{s_{\mathrm{NN}}} = 200$ GeV [21] Au+Au collisions and at LHC in $\sqrt{s_{\mathrm{NN}}} = 2.76$ TeV [18] and $\sqrt{s_{\mathrm{NN}}} = 5.02$ TeV [22] Pb+Pb collisions. Hydrodynamic

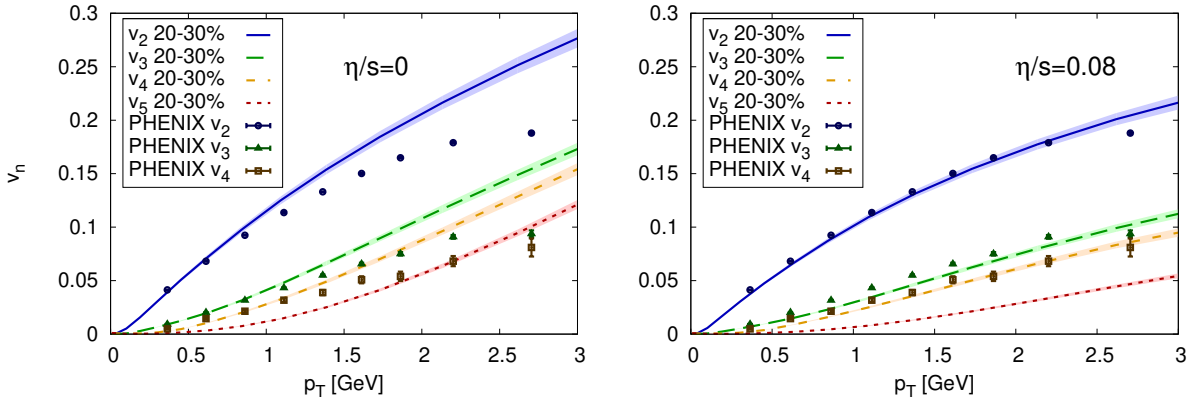

FIGURE 5 Hydrodynamic calculations compared to flow harmonics v_n, measured by the PHENIX experiment. The left figure shows the results for ideal hydrodynamics, in the right figure viscous hydrodynamics with $\eta/s = 0.08$ is used. Reprinted with permission from [25], 2012, American Physical Society.

calculations for zero viscosity fluid, describing the evolution from the QGP expansion until the freeze-out have proven to produce flow signal compatible with the measurements. The viscosity of a fluid describes its ability to return to local thermal equilibrium after being driven away from the equilibrium [23]. When comparing the shear viscosity over entropy ratio η/s, honey, for example, has a large viscosity compared to water since water reaches a still state faster than honey. Compared to water, QGP has even two orders of magnitude lower η/s [24]. The hydro calculations support the picture that almost near-perfect fluid is created in the form of QGP in the collision.

Although ideal hydrodynamic models explain the data with very good accuracy the models start to diverge from the data at large transverse momentum [25]. This can be seen in Figure 5 in which hydrodynamic calculations in the ideal and viscous cases are compared to measured flow harmonics. The ideal models do not produce the v_2 saturation that has been observed with larger transverse momentum particles and the p_T spectra start to deviate from the measurements after $p_T > 1.5$ GeV. Also, the success of the ideal hydrodynamic description depends on the centrality of the collision. Ideal models work well in central collisions where most of the colliding nuclei participate in the collision. The models, however, start to deviate the more peripheral the event is i.e. the nuclei will only partially collide. During recent years large developments have been made to better constrain the hydro models by studying the temperature dependence of shear and bulk viscosities of QGP, for example, Bayesian analyses taking a large number of measured flow observables as an input have sharpened the understanding of these properties [24, 26].

In addition to low momentum particles produced by flow mechanisms, so-called hard probes i.e. the high-energy jets of particles coming from the initial parton level collision are an important tool to study QGP. The measurements of nuclear modification factor for jets [28] and charged particles in general [29, 30]

$$R_{AA}(p_T) = \frac{1}{\langle N_{\text{coll}} \rangle} \frac{dN^{AA}/dp_T}{dN^{pp}/dp_T} \tag{2}$$

suggest that QGP is formed in collisions. In R_{AA}, the p_T spectrum measuref in heavy ion collision, normalized to the average number of binary collisions, is divided by the same spectrum

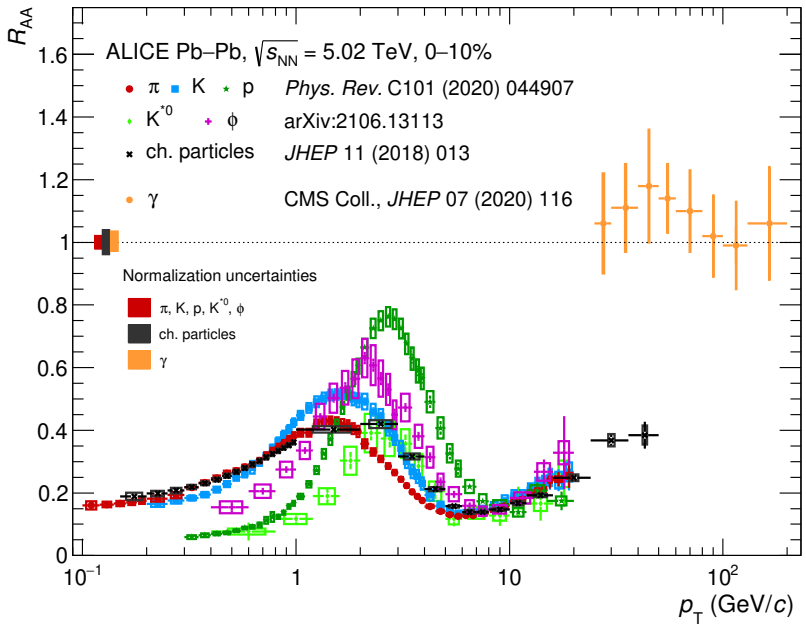

FIGURE 6 The isolated photon modification factor R_{AA} measured in CMS, plotted alongside R_{AA} of several different particle species measured in ALICE. Figure is taken from [27], reproduced under the license CC BY 4.0.

measured in pp collision. Figure 6 presents R_{AA} for several different particle species. In the case of no modification, R_{AA} would be equal to one but measurements show R_{AA} to be smaller which can be interpreted as strongly interacting particles losing energy due to interaction between the medium. For color neutral objects such as photons R_{AA} resides near 1 which supports the picture of strongly interacting matter [31].

In addition to constraining the hydrodynamics, the particle flow anisotropy is useful in studies of hard probes. The relation of jet production to the symmetry planes ψ_n allows to study the path-length dependence of jet energy loss in the medium. Since the overlapping area in a collision has an elliptic shape, the jets travelling in the direction of the minor axis (in-plane) of the ellipse are expected to travel a shorter distance in the medium and thus lose less energy than jets along the major axis (out-of-plane). This can be quantified by v_2^{jet} which is jet equivalent

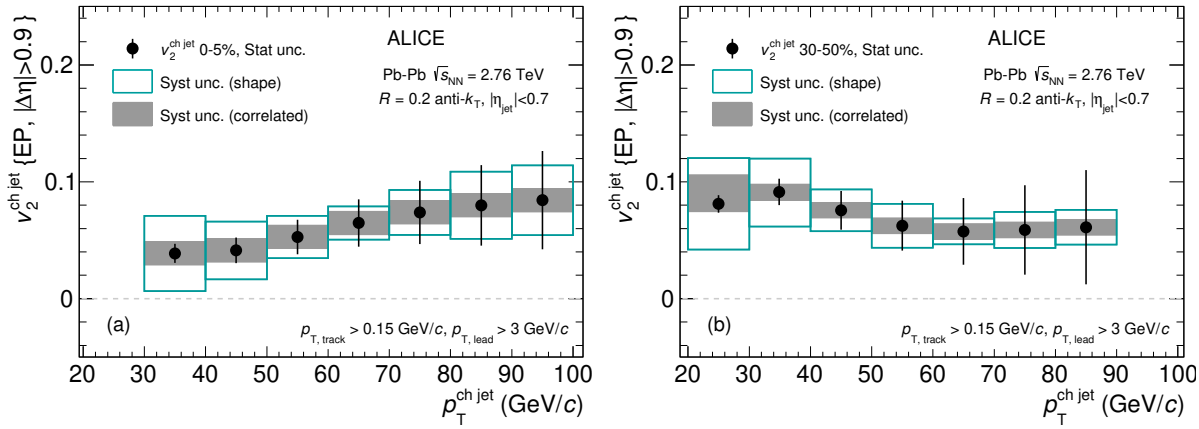

FIGURE 7 The second order coefficient $v_2^{\text{ch jet}}$ of Fourier expansion for charged jet azimuthal distribution, presented as the function of $p_{\text{T}}^{\text{ch jet}}$ at centrality $0-5\%$ (left) and $30-50\%$ (right). Figure from [32], reproduced under the license CC BY 4.0.

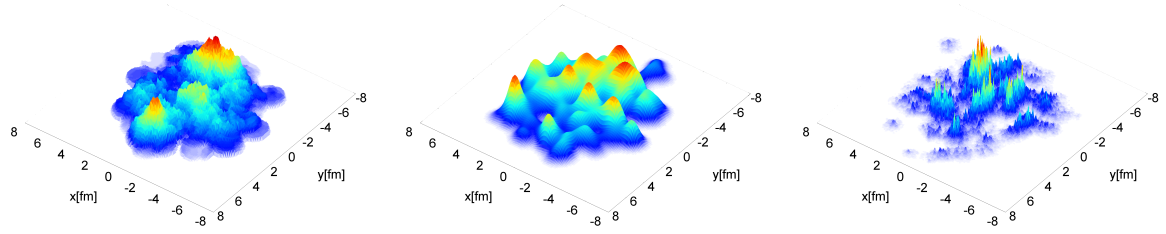

(a) MC-Glauber **(b)** MC-KLN **(c)** IP-Glasma

FIGURE 8 Initial energy density for a heavy ion collision, calculated in three different initial stage models. Reprinted with permission from [38], 2012, American Physical Society.

to the second-order flow harmonic v_2 in Equation 1. Measurement of $v_2^{\text{ch jet}}$ for charged jets is presented in Figure 7 [32]. v_2^{jet} is measured by comparing the jet orientation to the second-order symmetry plane ψ_2 in the event. In the central collisions the overlapping area is more symmetric and therefore the jets in-plane and out-of-plane are expected to travel similar lengths in the medium. This would lead a smaller value of $v_2^{\text{ch jet}}$ in central collisions compared to more peripheral collisions. In these results conclusion can not be made between the two centrality classes due to large uncertainties. However, the positive v_2^{jet} indicates that jet suppression, similarly to the anisotropic flow, is sensitive to the initial geometry in the collision. Because uncertainties in hydrodynamic calculations comes from the initial conditions, it is important to define such sensitive observables to constrain the models better [33].

Figure 8 shows heavy ion collision initial energy densities in transverse plain, calculated via three different models. As can be seen, different initial condition models produce very different initial profiles. In Monte Carlo Glauber models [34] the energy density is parametrized with transverse profiles of participant nucleons and binary collisions. The positions of nucleons are calculated based on the nuclear density distribution. Monte Carlo Kharzeev-Levin-Nardi (MC-KLN) [35] model similarly defines the nucleon positions from the Glauber model but takes also into account the gluon production based on Color Glass Condensate (CGC) model [36]. Similarly, the gluon contribution is relevant in IP-Glasma in which the initial fluctuating color fields are generated from impact parameter dependent saturation model (IP-Sat) [37] for the colliding nuclei [38]. The difficulty in choosing the initial stage model is that no single model produces all the final states that are measured in the experiments. For example, MC-KLN does not describe measured v_2 and v_3 simultaneously [39]. Therefore, as mentioned, measurements are needed to constrain these models better.

As can be noticed, the CGC framework plays a large role in the initial stage modelling. The gluon contribution becomes even more relevant when the low momentum scales in the strongly interacting particles are considered. The key property of CGC is the so-called gluon saturation phenomenon which is discussed in the next section.

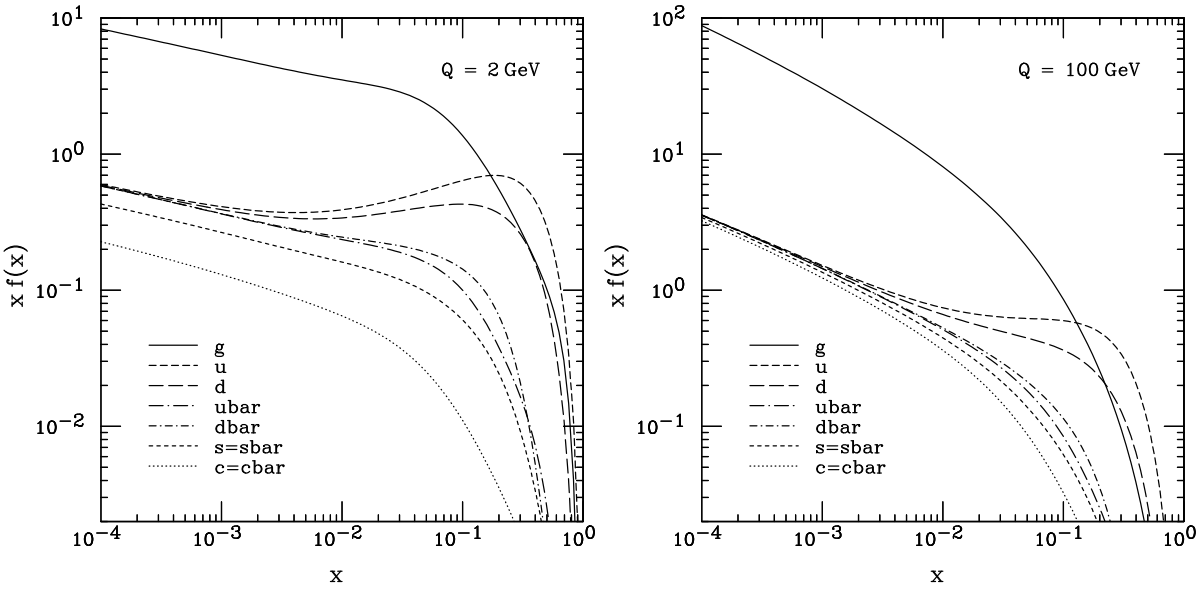

FIGURE 9 CTEQ6M PDFs at $Q = 2$ GeV and $Q = 100$ GeV extracted from global fits. At decreasing x the gluons and sea quarks start to become more probable than at higher x, the increase being stronger at the larger scale of $Q = 100$ GeV. Reprinted with permission from [41], 2002, IOP Publishing.

1.2 Gluon Saturation

To understand the properties related to gluon saturation it is necessary to take a step back from heavy ions and focus on a single proton first. According to the quark model proton consist of two u quarks and one d quark. However, the structure of proton is not stationary but the constituents fluctuate, gluons splitting into virtual quark-anti quark pairs and recombining back to gluon again. One way to understand the hadron structure better is to study their parton distribution functions (PDFs) [40] which describe the proton contents at different scales: when the proton is probed at smaller wavelength the smaller details in the structure start to unfold.

PDFs are presented as (number) density function over x, the momentum fraction of the parton taking part in the initial collision to the whole nucleon. PDFs also depend on virtuality Q^2 which quantifies the momentum transfer in the collision. Figure 9 shows a global PDF analysis from the CTEQ collaboration at $Q = 2$ GeV and $Q = 100$ GeV [41]. At higher values of x the valence quarks mostly make up the proton and thus have higher probabilities. Moving towards smaller x values the sea quarks start to also contribute as the gluon density increases. The Q-dependence can be seen in the significantly higher gluon density at the larger scale.

The increase in the gluon density low x region happens because the gluon splitting process becomes more and more relevant as we start to reach lower values of x. Gluon splitting is a linear process, meaning that it's proportional to the gluon density. The QCD evolution can then be described by models that only take into account the linear increase of the splittings. When taking a look at the (x, Q^2) phase space (see Figure 10) the evolution in respect of Q^2 is described by the DGLAP (Dokshitzer–Gribov–Lipatov–Altarelli–Parisi)) equations [42] and the evolution along x is calculated via the BFKL (Balitsky–Fadin–Kuraev–Lipatov) equation [43]. These equations describe the linear gluon density evolution but at very small x and Q^2 values i.e. at very large gluon densities the non-linear effects become prominent.

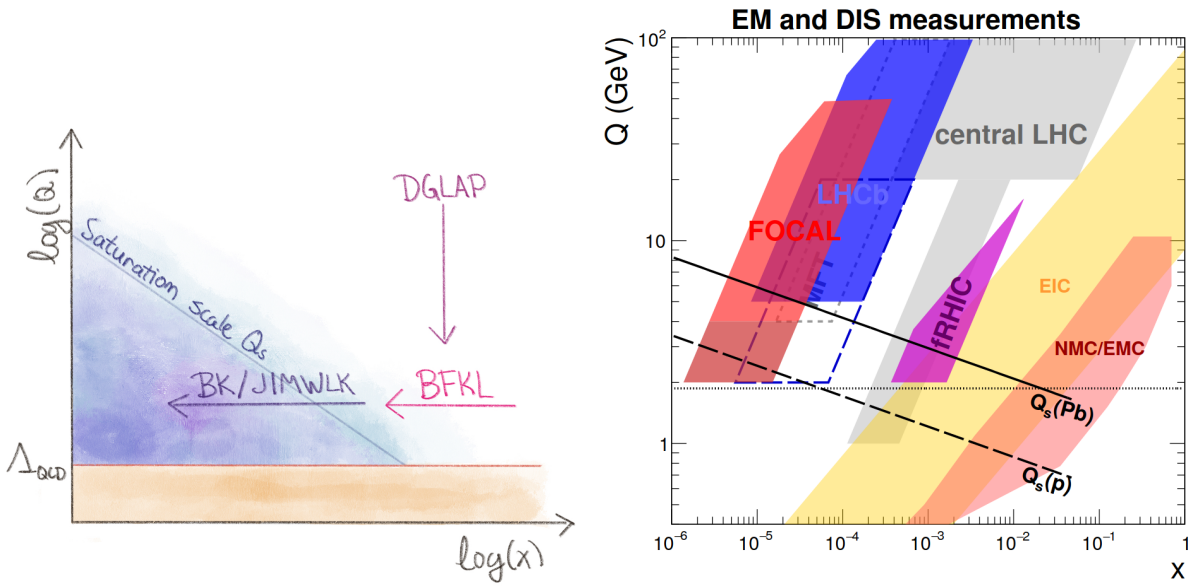

FIGURE 10 Expected gluon behaviour in x–Q plane and how the equations follow the evolution (left). Kinematic coverages of several current and future high energy experiments for EM and DIS measurements (right). The two black lines are estimations for saturation scales for proton and lead. Figure from [46], reproduced under the license CC BY 4.0.

As the gluon density rises the gluons start to recombine due to finite space. Gluon recombinations start to halt the growth of gluon density when they becomes as relevant processes as the gluon splitting. The point where both processes are equally likely to take place is called the saturation limit Q_s. Unlike gluon splitting, recombination is a non-linear process. This complicates the calculations and the gluon density evolution cannot be described exclusively via DGLAP and BFKL when the recombination starts to take part. The limitation of gluon density growth can be handled with JIMWLK (Jalilian-Marian–Iancu–McLerran–Weigert–Leonidov–Kovner) equation which generalization is BK (Balitsky–Kovchegov) equation [44, 45].

Strong experimental evidence for gluon saturation has yet to be found. This is due to the lack of experiments that reach the kinematic regions with necessary precision. Experimentally low x region can be explored by performing measurements at forward rapidity. This is because the momentum fraction x of incoming parton depends on the transverse momenta p_{T} and rapidity y of the emitted partons [46],

$$x \approx \frac{2p_{\mathrm{T}}}{\sqrt{s}} \exp(\pm y). \tag{3}$$

Therefore measuring observables at low as possible p_{T} at high rapidity then allows to probe high gluon densities. To illustrate what kind of values of x can be experimentally reached the kinematic regions covered by different high-energy experiments are plotted in Figure 10. The upgrade of LHCb will allow measurements at lower Q and x in the near future. The current coverage of LHCb is plotted with dark blue while the expected coverage after the upgrade is lined with the dashed line. The ALICE experiment also aims to expand its forward physics program in the form of forward calorimeter FoCal [46] during the same upgrade period. FoCal will be able to reach smaller values of x than any current (or near future) experiment, reaching as low as $\sim 10^{-6}$. Upgraded LHCb has similar coverage in Q with FoCal but due to the smaller rapidity range does not reach as low as FoCal.

When probing the saturation region it is of interest to probe targets of varying sizes. This is because the saturation scale grows in large nuclei [46] as

$$Q_s^2 \approx A^{1/3} x^{-\lambda}, \tag{4}$$

where A is the mass number of the nucleus and $\lambda = 0.2 - 0.3$ [47]. For this reason the saturation is expected to be reached at higher x and Q^2 in larger nuclei compared to pp collisions. In Figure 10 the estimated saturation scales in lead and proton are marked with the two lines in the (Q,x) plane. According to the expected coverages of LHCb and FoCal, both experiments are expected to observe saturation in proton. Also, Electron Ion Collider (EIC) [48], currently under construction in BNL, will be able to cover new kinematic regions via DIS measurements.

On the contents of this thesis

The work presented in this thesis covers performance studies for new detectors of the ALICE experiment included during Long Shutdowns (LS) 2 and 3. The studies include simulations of detector response in both proton and heavy ion collisions, and test measurements of sensor developed for the future ALICE calorimeter FoCal. The main analysis is simulation of FoCal's performance of π^0–π^0 correlations which is an interesting measurement regarding gluon saturation physics.

2 ALICE UPGRADES

ALICE [49] is one of the four large experiments, alongside ATLAS [50], CMS [51] and LHCb [52], at the Large Hadron Collider (LHC). ALICE is the dedicated heavy ion experiment optimized for measuring signals from the QGP phase, and for that reason, its detectors specialize to detect low momentum particles and to identify the different particle species emerging from the collisions. The physics goals for ALICE were to demonstrate the phase transition and verify the theory predictions while quantifying the properties of QGP [53]. Though first the focus was the study of low momentum phenomena such as flow, the discovery of jet quenching at RHIC [54, 55] expanded the physics program to hard probes and lead to the inclusion of EMCal [56]. While the phase transition and the existence of QGP were confirmed at CERN SPS [57] and at RHIC [54, 55, 58, 59] in early 2000, ALICE would then continue to produce additional proof for QGP and to investigate its properties at higher temperatures. The key results from the original running of ALICE (Run 1 & Run 2) are collected in [27].

Although the ALICE experiment has produced a lot of quality data and analyses from different collision systems, in order to determine QGP properties with even higher precision, the experiment underwent significant upgrades to continue data taking during the next run. LHC physics endeavors were stopped for the Long Shutdown 2 (LS2) in 2018-2022 during which the LHC was prepared to produce larger beam luminosities for Run 3 [60]. For ALICE there are plans also beyond Run 3. The following sections give an overview of the future physics goals of ALICE and what kind of upgrades are needed to meet these goals.

2.1 ALICE Run 3 upgrade

The increase in LHC beam luminosity means that detectors need to cope with higher collision rate. For ALICE the upgrade meant adjusting to measure PbPb collisions at 50 kHz rate (Luminosity of $\mathscr{L} = 6 \times 10^{27}\ 1/(\mathrm{cm}^2\,\mathrm{s})$), 50 times more collisions compared to the previous runs. This gives ALICE the possibility to study rare probes that were not possible to measure during past runs due to the lack of statistics. The measurements include heavy-flavour (charm and beauty quark) production, low-momentum quarkonium, thermal photons and di-leptons emitted by QGP, jets measurements to study in-medium parton energy loss, and search of heavy

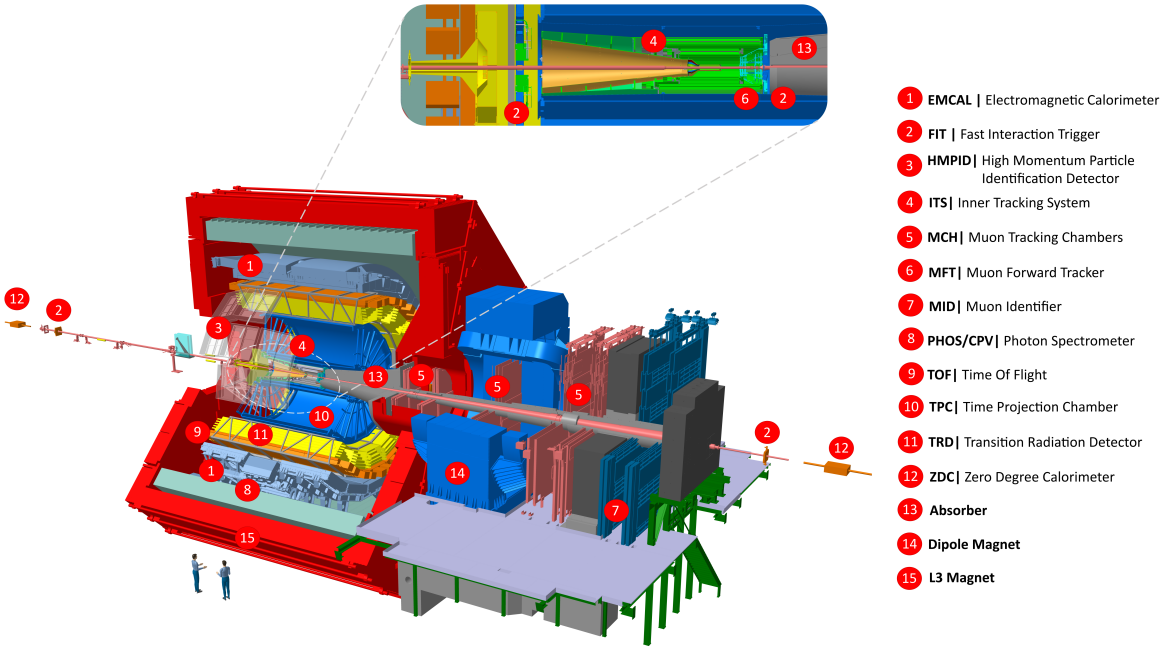

FIGURE 11 The ALICE setup for Run 3. The placements of different sub detector are denoted with numbers. Compared to the old setup most detectors have remained same (although upgraded), new inclusions are the forward detectors (Fast Interaction Trigger and Muon Forward Tracker). Figure from [60], reproduced under the license CC BY 4.0.

nuclear states [61]. The goal in heavy flavour measurements is to understand the charm and beauty quark thermalization in QGP via measuring baryon-to-meson ratios and heavy-quark flow. Low-momentum quarkonia such as $\psi(2S)$ and J/ψ are presumed to experience suppression in QGP and this would be evidence for the models predicting that. Photons and di-leptons are produced in every stage of the collision and are free of the modification by the medium which makes them invaluable probes for all stages. Jets provide information on fragmentation functions and the energy loss of partons in the medium.

The ALICE setup after the LS2 upgrade is shown in Figure 11. To meet the physics goals the ALICE sub-detector readouts needed to be upgraded to be able to withstand the higher collision rates. The readout electronics of Muon CHamber System (MCH), Muon IDentifier (MID), Transition Radiation Detector (TRD), and the Time-Of-Flight (TOF) detector were revamped [62]. Higher readout rates demand also faster online data processing and efficient data compression to keep the offline data manageable. For these reasons a new Online-Offline (O^2) simulation and analysis framework [63] has been developed. In O^2 the data is reconstructed and calibrated for some parts synchronously during the data taking already. For example, in TPC the cluster finding and first track reconstruction are performed online [64]. The final, more detailed analysis is then done the traditional way offline. The offline reconstruction reduces data at the early stages of the processing which leads to more efficient data flow.

In addition to preparations for the higher data rates, many of the suggested physics analyses demand better vertex determination and measuring particles efficiently at lower momentum,

keeping the excellent particle identification capabilities. Particle tracking is handled by the mid-rapidity tracking detectors Inner Tracking System (ITS) and Time Projection Chamber (TPC) in which the prevalent detection technologies were changed to meet the requirements [65, 66]. The readout rate posed a problem to the original systems of ITS and TPC and thus the ITS silicon detector layers were changed to ALPIDEs, CMOS Monolithic Active Pixel Sensors (MAPs) [67], and the endcap wire chamber readout of TPC was replaced with GEM (Gas Electron Multiplier) foils [68]. To improve the detection of heavy-flavour hadrons, QGP emitted thermal photons via e^-e^+ conversions and low-mass di-leptons the ITS capability to measure the primary and secondary vertex positions needed to be better. This was achieved by reducing the beam pipe diameter from 29.8 mm to 19.2 mm [69] so that the first layer of the tracker can be brought closer to the interaction point (IP). Also, the material budget of the first layer dropped from an already small value of 1.1% X_0 to 0.3% X_0, further increasing the capability to separate secondary vertices from the primary vertex [65].

Completely new additions to the ALICE setup were the forward rapidity detector systems Muon Forward Tracker (MFT) [70] and Fast Interaction Trigger (FIT). MFT is located in front of the absorber (see Figure 11) and together with MUON spectrometer they cover the rapidity range of $-3.6 < \eta < -2.45$ in the forward region. Improved tracking of muons reconstructed in the spectrometer extends the muon physics program of ALICE. With the tracking, the vertex position of J/ψ and $\psi(2S)$ from their muonic decay channels can be measured at high precision. It also allows to reject semi-muonic decays of pions and kaons which present significant background in these measurements [71]. FIT is the new forward trigger system replacing the previous one. Details of FIT are important for the results of this thesis and thus it is presented in more detail.

Fast Interaction Trigger

FIT is a group of three different detector subsystems that are located in the forward region of ALICE. The three detector subsystems, FV0, FT0, and FDD, are depicted in Figure 12. The detectors are successors to previous forward detectors used during Runs 1 and 2, carrying on with the same responsibilities and, to a large extent, applying similar design choices as the older detectors. FV0 resembles VZERO detector [72] from older runs whereas FDD is upgraded version of AD detector [73]. FT0 takes the tasks of T0 detector [74] but with a different choice of sensors and significantly larger acceptance.

FV0 is a large scintillator disc with a diameter of $r = 1.44$ m. It is located at $z = 3.16$ m from the IP at the so-called A-side[1] of the ALICE detector and it covers pseudorapidity range $2.2 < \eta < 5.5$. There are 48 individually read channels in FV0: the disc is divided into five rings and radially into eight (16 in the outmost ring) sections. FV0 is complemented with FT0-A, one of the two cherenkov radiator arrays that constitute FT0 detector. The other part, FT0-C, is located at the C-side and closer to the IP at $z \approx -0.8$ m (FT0-C is curved and thus channels have varying distance at z direction). FT0-A and FT0-C cover pseudorapidities of $3.5 < \eta < 4.9$ and $-3.3 < \eta < -2.1$ respectively. The sesors used in FT0 are Microchannel Plate PMTs (MCP-PMT) and collect the photons from the quarz radiators placed on top of them. Each MCP-PMT is coupled with four radiators i.e. one MCP-PMT has four channels. Together both FT0 arrays have then 208 channels in total.

[1] A- and C-side refer to the direction of the ATLAS and CMS experiments at the LHC tunnel.

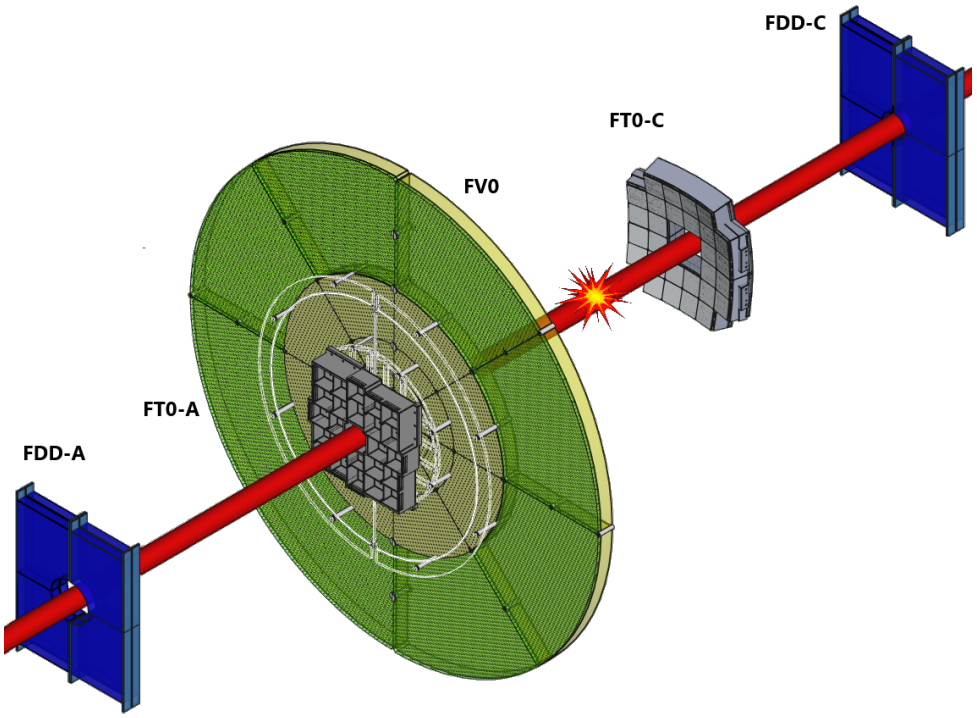

FIGURE 12 A schematic of the three FIT detectors without their support structures and cables, situated on the both sides of the IP. The distances do not reflect the real life positions of the detectors. The source of image: CERN.

FV0 and FT0 in real life can be seen in Figure 13. FV0 is divided into two halves which are placed in aluminium cases. The halves are separated by an aluminium plate in the middle. Having the large detector divided into two halves was necessary for the installation in the limited space. The smaller FT0 array structures are also made of aluminium. The signal cables are pulled to the sides and on the left side photo the cabling can be seen on the A-side.

Forward Diffractive Detector, FDD, consist of two plastic scintillator arrays at both sides of the IP. The arrays are located 17 m away from the IP on the A-side and 19.5 m on the C-side. They then reach very high pseudorapidities, FDD-A covering the range of $4.7 < \eta < 6.3$ and FDD-C $-6.9 < \eta < -4.9$ [75].

FIT has several important tasks essential for the running of ALICE. These tasks include [76]:

Trigger signal: The low level triggers are provided by FIT. Six ALICE sub-detectors (TRD, CPV, HMPID, EMCAL, DCAL, PHOS) require an external trigger for the operation because continuous readout is not feasible in their case. This makes FIT essential for the running of the experiment. FIT will also provide the important Minimum Bias (MB) trigger.

Luminosity monitoring: The LHC experiments also monitor beam luminosity and send the information to LHC. Since FIT is measuring the multiplicity in forward rapidity it is naturally suited for the task. FDD will also provide monitoring of beam-gas events, interactions between beam particles and gas atoms that produce background.

Timing: Because of excellent time resolution of FT0 FIT can provide collision time for TOF particle identification.

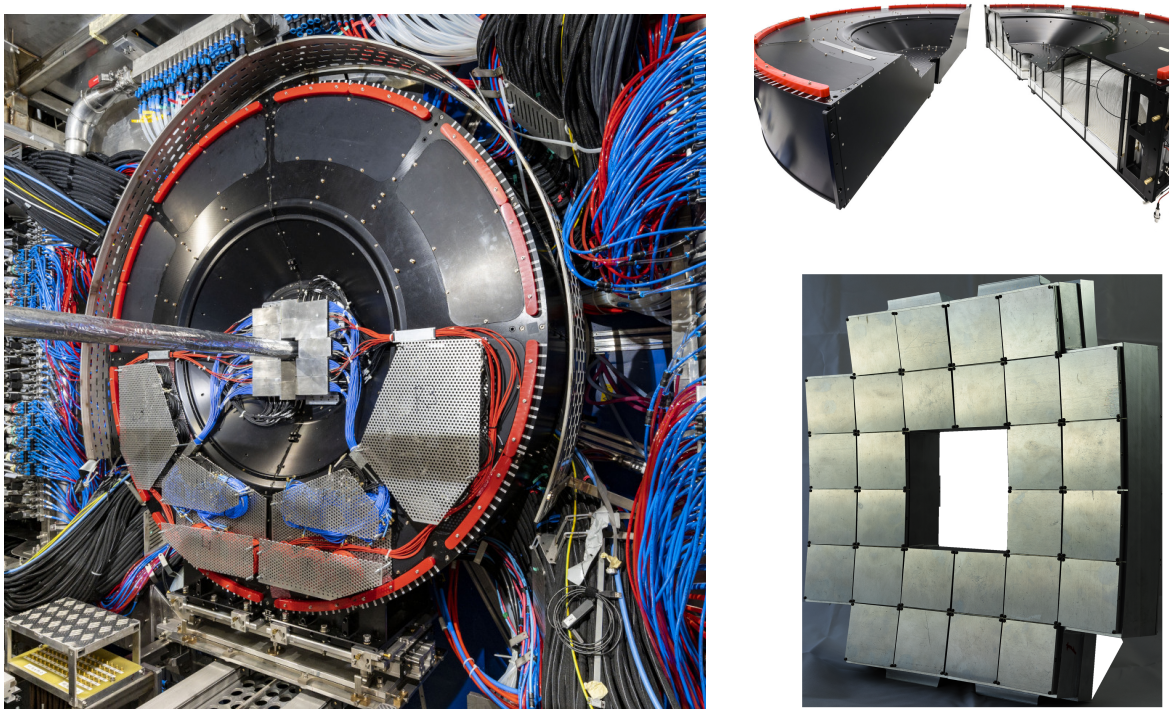

FIGURE 13 Photos of various FIT subsystems, including the mechanical structures around them. The left photo is showing the A-side detectors after installation around the beam pipe, FV0 (covered by the black aluminium case) and FT0-A (in the middle of FV0). The inner rods of the case and the light collection fibres of FV0 can be seen in the top right photo. The curved FT0-C structure is shown in the bottom right photo. Each square-shaped plate covers one MCP-PMT. The source of images: CERN.

Diffractive & UPC events: As the name suggests, FDD will measure diffractive events [77] which can be seen as event activity with a large gap in rapidity. FDD can be also used for vetoing particles in order to obtain clean samples for UPC events [75].

Centrality: FV0 and FT0 are used to determine the centrality for the event classification in physics analyses.

Event plane: Several FIT detectors can be used to estimate the collision geometry in the form of event plane.

Together with Oskari Saarimäki, I performed simulations to determine the event plane resolution of FIT for Run 3. The simulations are presented in detail in Section 3, emphasizing my contribution to the work.

2.2 ALICE beyond Run 3

The plans for the continuation of the experiment after Run 3 are already in motion. Figure 14 shows the LHC timetable at the end of the year 2038. This period will include Run 4 and 5, having the two Long Shutdown periods in between for necessary upgrades. After Run 3 the LHC will move to the high luminosity era during which the luminosity will increase significantly compared to the previous runs [78]. The next larger upgrade that concerns the whole ALICE setup will take place after Run 4. The plan is to transform ALICE into ALICE3 detector [79]

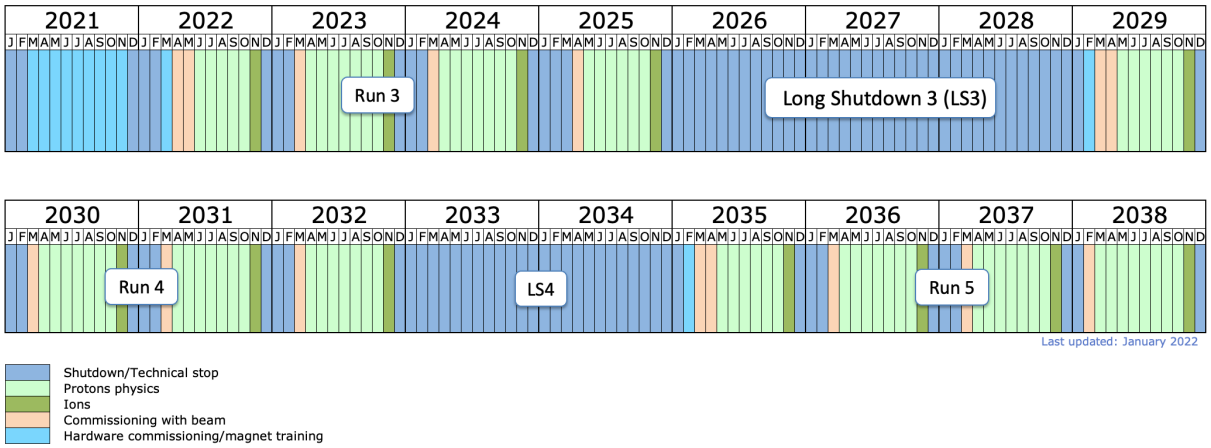

FIGURE 14 LHC timetable starting from the last year of LS2 and ending at the expected closure of the high luminosity era ALICE3 detector. Image by CERN.

in which the aim is to reduce the material budget in the central barrel as low as possible. This allows the study of ultra-low transverse momenta particles, down to tens of MeV.

Even though during LS3 ALICE will not have as an extensive upgrade program as during LS2 there will be two important upgrades to the setup. First of these is the addition of whole new Forward Calorimeter (FoCal) [46] which will provide measurements at kinematic regions never reached before. FoCal will enable measurements that would probe the saturation physics and PDFs at low momentum fraction x. The second change is the upgrade of the ALICE Inner Tracking System (ITS) into ITS3 [80]. ITS3 will have tracking layers of thin silicon sensors bent into a cylindrical shape which will reduce ITS material budget greatly. Both FoCal and ITS3 will utilize the ALPIDE technology currently used in ITS and MFT in their design which is the biggest factor enabling these detectors to fulfill the research goals.

2.3 FoCal

After Long Shutdown 3 at LHC, the ALICE experiment will extend its forward physics program further. FoCal allows measurements between $3.5 < \eta < 5.8$. FoCal will consist of a compact electromagnetic calorimeter (FoCal-E) followed by a hadronic calorimeter (FoCal-H). The dimensions of FoCal in the transverse plane are roughly 90 cm $\times$ 90 cm, depending on the gaps between different modules. For FoCal-E the length in z-direction will be between $15 - 25$ cm, the final length again depending on how closely the parts can be placed in the final design [46]. The length of FoCal-H will be longer than its electromagnetic counterpart, exceeding one meter. The length and the placement of FoCal is limited by the compensator magnet of ALICE and with these dimensions, FoCal can be placed at 7 m away from the interaction point, calculated from the front of FoCal. The geometry of FoCal at its intended location in front of the compensator magnet is shown in Figure 15.

FoCal-E is a sampling calorimeter with a sandwich structure, that is FoCal-E consists of alternating layers of active and passive material. The passive material is tungsten and the active layers are thin silicon sensors. FoCal-E will then have 20 layers of Si-W pairs which will correspond to a radiation length of $X_0 = 20$. A row of five 20 layer towers will form a super module

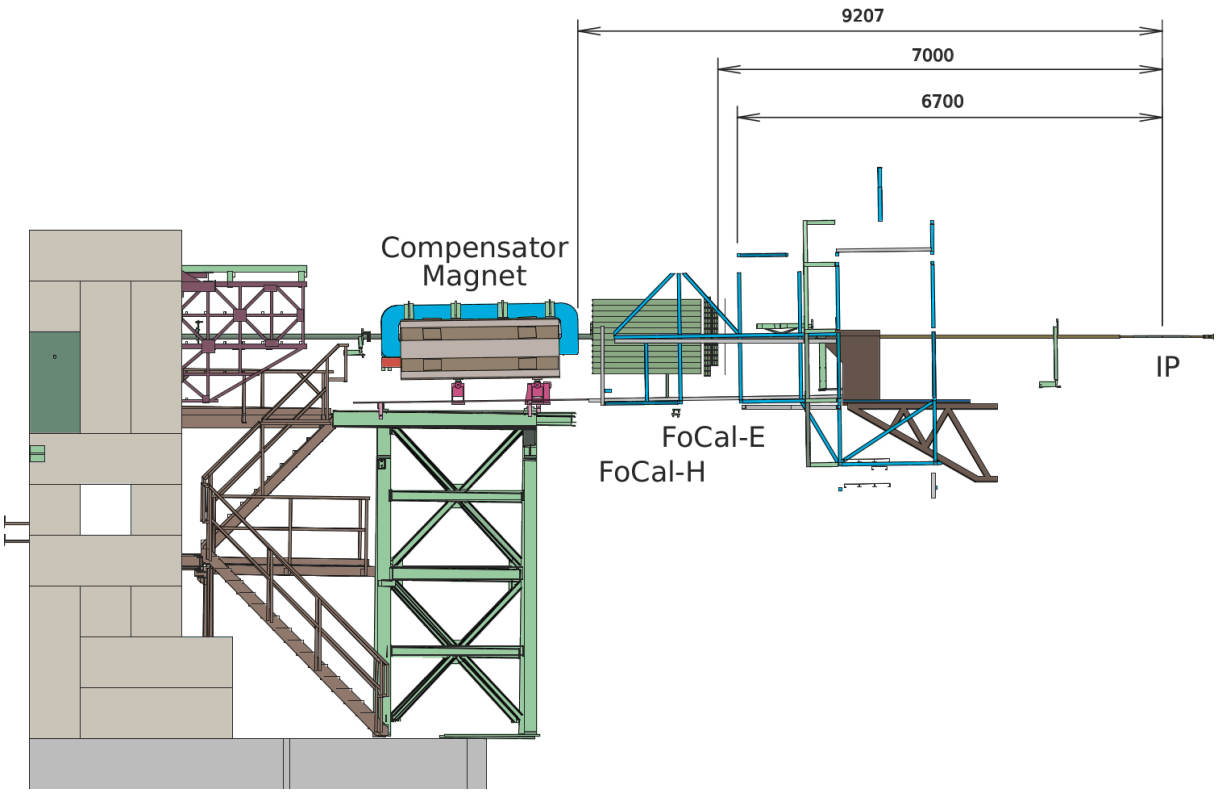

FIGURE 15 A schematic showing the placement of FoCal in the ALICE experiment. The front of FoCal will be 7 m away from the IP, between the compensator magnet and the ALICE dipole magnet door. Figure from [46], reproduced under the license CC BY 4.0.

and these super modules will be stacked to form the full detector. A schematic of one FoCal-E tower and the arrangement of the super modules is shown in Figure 16.

Two different technologies are used in the layers: high granularity ALPIDE pixel layers and pad layers. 18 out of the 20 layers make use of the pads that have 1 cm $\times$ 1 cm large silicon channels. The other two are then the pixel layers which have channels size of 30 µm $\times$ 30 µm. The pad layers provide the shower energy measurement and coarse determination of the shower spatial coordinates. Usage of the higher granularity layers allows much more precise determination of the shower center which is needed in the reconstruction of neutral mesons (π^0, η, ω). The ability to reconstruct π^0 enables, for example, correlation studies such as π^0–$\pi^0$and γ–π^0 in the forward rapidity.

The hadronic part of the calorimeter will use different kind of approach for the geometry of the detector. FoCal-H is build by grouping 110 cm copper tubes parallel to the z-axis. Scintillating fibres of same length are placed inside the copper tubes. In this case the copper will act as the passive material and the signal is measured from the fibres via photomultiplier tubes placed to the backside of the calorimeter. The light production in the fibres is propotional to the energy of the traversing particle. Without FoCal-H a clean measurement of isolated photons, which is discussed later, would not be possible. Having the hadronic calorimeter also allows the measurement of jets at the forward rapidity. The dimensions of FoCal-H alongside FoCal-E can be seen in Figure 16.

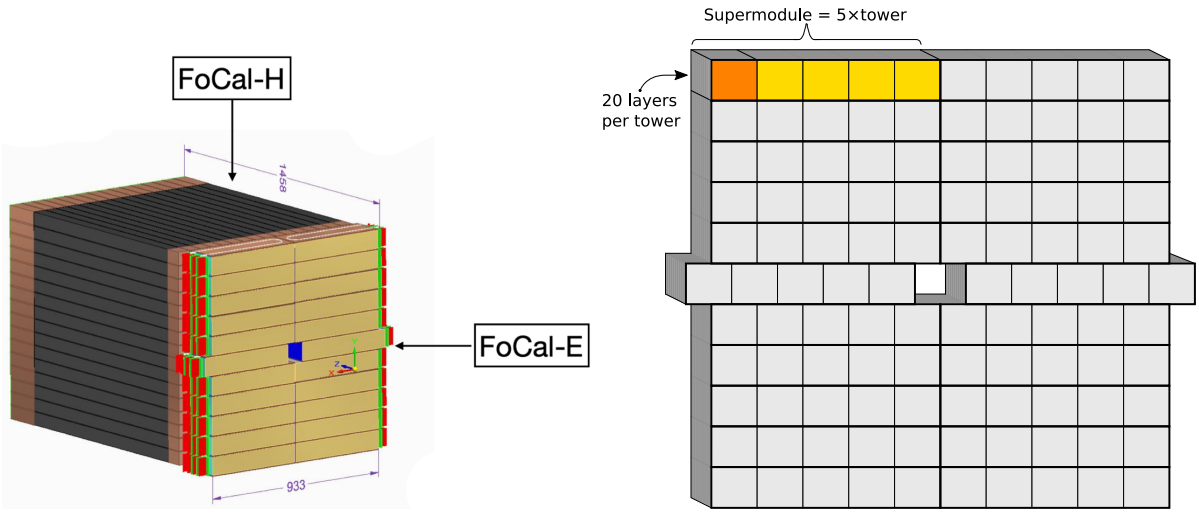

FIGURE 16 The geometry of FoCal with the dimensions in mm (left). The division of FoCal-E into individual towers is seen in the right figure.

2.3.1 Physics observables

The physics program of FoCal is quite extensive and in addition to electromagnetic probes includes, for example, jet and ultra-peripheral collision (UPC) measurements, as well as the possibility to study long-range flow correlation at forward rapidity [46]. In this section few key measurements are reviewed: direct photons, UPCs, and two-particle correlations. Out of these observable the two-particle correlation are discussed in this thesis.

Experimentally all measured photons (inclusive photons) can be divided into two categories: decay photons and direct photons. Photons from decays are produced at the later stages of the collision whereas direct photons come from the primary interaction. Direct photons can be further divided into prompt photons and fragmentation photons. Prompt photons are produced in the initial hard scattering process between the partons via $qg \rightarrow q\gamma$ (quark-gluon Compton scattering) or $q\bar{q} \rightarrow \gamma g$ (quark-antiquark annihilation) at leading order (diagrams in Figure 17a and Figure 17b), and via bremsstrahlung $qq \rightarrow qq\gamma$ at next-to-leading order (Figure 17c). Fragmentation photons are emitted in the parton fragmentation process (Figure 17d).

Prompt photons carry valuable information about the partonic kinematics since they are not affected by final state effects such as fragmentation. The challenge in the measurement is that experimentally observed photons are all the same: separation can not be made whether the signal is from a prompt or decay photon. In the end, it is always inclusive photons that are

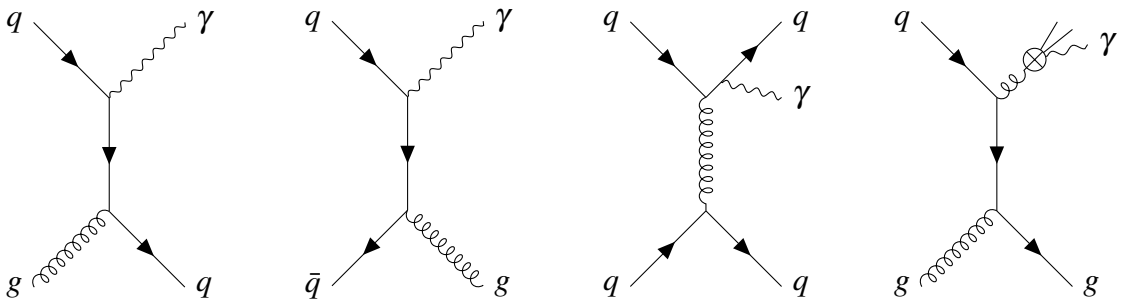

(a) Compton **(b)** Annihilation **(c)** Bremsstrahlung **(d)** Fragmentation

FIGURE 17 Different production channels of direct photons, presented as Feynman diagrams.

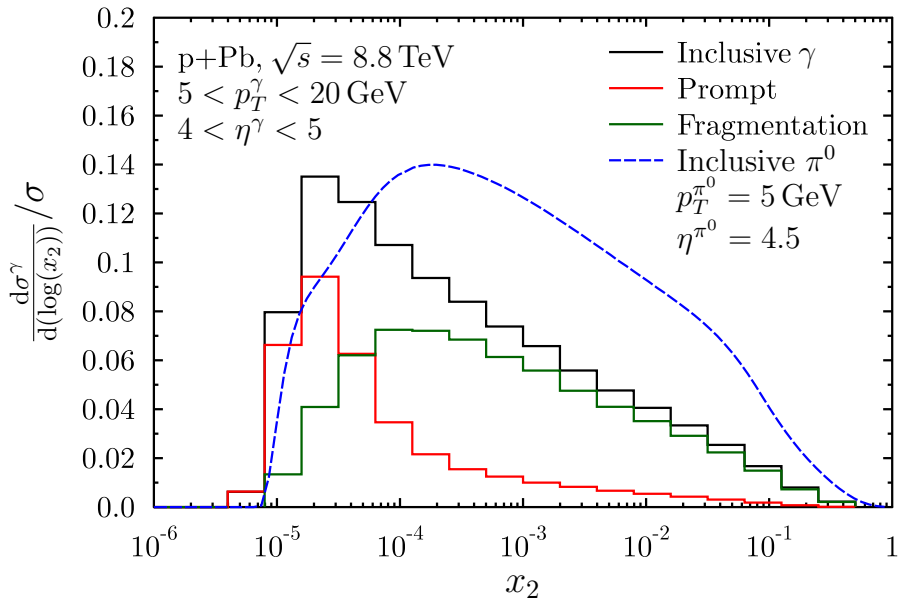

FIGURE 18 The cross section for prompt and fragmentation photons, as function of momentum fraction x_2, accompanied by the cross section of pion production. Figure taken from [82], reproduced under the license CC BY 4.0.

being measured. However, the prompt photon purity in the data sample can be enhanced by introducing different cuts. The decay photon contribution can be decreased by identifying them via shower shape analysis [81] and invariant mass method (which is relevant to this thesis and thus explained Chapter 5), and then excluded from the analysis. For the fragmentation photons isolation cut can be introduced to exclude them from the sample. The fragmentation photons are usually accompanied by the hadrons of the jet originating from the initial parton. Therefore by omitting measured photons in which there is a lot of hadronic activity present the prompt photon signal can be enhanced. The most common way to apply the isolation cut is to calculate the sum of transverse energy ΣE_{T} inside a cone of radius R. If the energy is larger than selected $E_{\mathrm{T}}^{\mathrm{max}}$ the photon is discarded. In the experimental context, the photons selected through isolation cut are then called isolated photons.

The prompt photon production has been investigated for the purpose of probing the low x region [82]. Figure 18 shows the cross section for prompt and fragmentation photons, along with cross section of pions, as function of momentum fraction x of the parton. In this theory calculation inclusive photons refer to sum of prompt and fragmentation photons and do not include decay photons. Compared to the fragmentation photons the prompt component distribution reaches lower values of x. There exist some overlap with the two components but prompt photons are more prominent at low x whereas the distribution of fragmentation photons is broader. Thus measuring prompt photons gives access to the low x kinematics.

Isolated photons, the experimental proxy for prompt photons, will then be beneficial to understand the behaviour of a gluon carrying a small momentum fraction. Measuring nuclear modification factor R_{pPb} gives an opportunity to test the boundaries of the models describing the gluon density evolution. Figure 19 presents calculations of photon R_{pPb} using the collinear factorization and DGLAP equation [82] and CGC framework [83]. The CGC calculation predicts suppression of R_{pPb} when moving to larger rapidities while weaker rapidity dependency

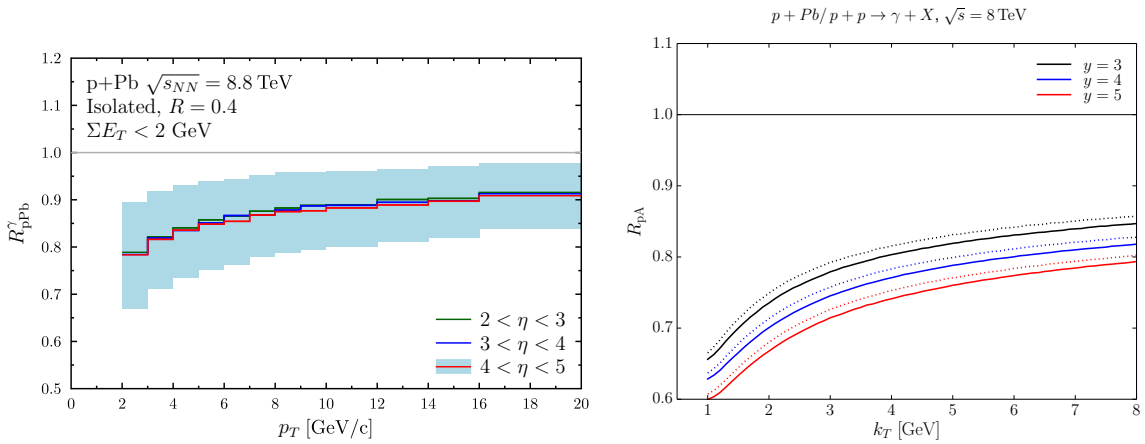

FIGURE 19 Calculations for the nuclear modification factor R_{pPb} at different rapidities. The left figure shows results from a calculation using the collinear factorization and DGLAP evolution [82] and the right figure performing the calculation in the CGC framework [83]. Figures reproduced under the license CC BY 4.0.

is observed in the case of the collinear factorization. Therefore the measurement might provide information about the presence of the saturation effect.

The isolated photon measurement is also an interesting measurement regarding nuclear PDFs which describe the PDFs of nucleons inside nucleus [84]. nPDF's are not just the sum of individual nucleon PDFs which can be seen in Figure 20. The figure shows the nuclear modification factor R_g^{Pb} in which the gluon nPDF in lead nucleus is compared to the gluon PDF in proton [85]. Especially the gluon nPDFs have had large uncertainties but recently the promt D^0 data measured by the LHCb collaboration [86] constrained the nPDF behaviour at low x. Now the inclusion of D^0 data confirms the presence of gluon shadowing [84] at low x where R_g^{Pb} goes below one. For the nuclear modification factor from nNNPDF2.0, shown in the figure, the uncertainties are reduced significantly in recent nNNPDF3.0 data with the LHCb D^0 data included [87]. Isolated photon measurement in FoCal can be used to further constrain the nuclear PDFs and test out the universality of low x region description by providing an independent measurement.

In addition to the isolated photons FoCal will also extend studies of ultra-peripheral collisions (UPCs) to lower x. UPCs are defined as collisions where the impact parameter is larger than the sum of radii of the colliding ions. In these events the interactions happen mainly between the electromagnetic fields of the ions and hadronic interactions are minimal. This allows the study of interactions of single photons with the target ion.

The photoproduction of J/ψ can be coherent or incoherent. In coherent production the emitted photon couples with the whole target nucleus and in this case the target stays intact. In incoherent production, however, the photon interacts only with a single nucleon which normally leads to breaking up the target nucleus. After being produced the J/ψ can decay into a lepton pair (e^+e^- and $\mu^+\mu^-$). From the experimental point of view the process leaves a unique signal to the detector: only the lepton pair is seen in the forward region in an otherwise empty detector. In incoherent production, the lepton pair signal can be accompanied by nuclear fragments from the breakage of the nucleon. There is also a difference in the vector meson transverse momentum from the two production channels: for the coherent production $\langle p_{\mathrm{T}} \rangle \approx 60$ MeV$/c$ and

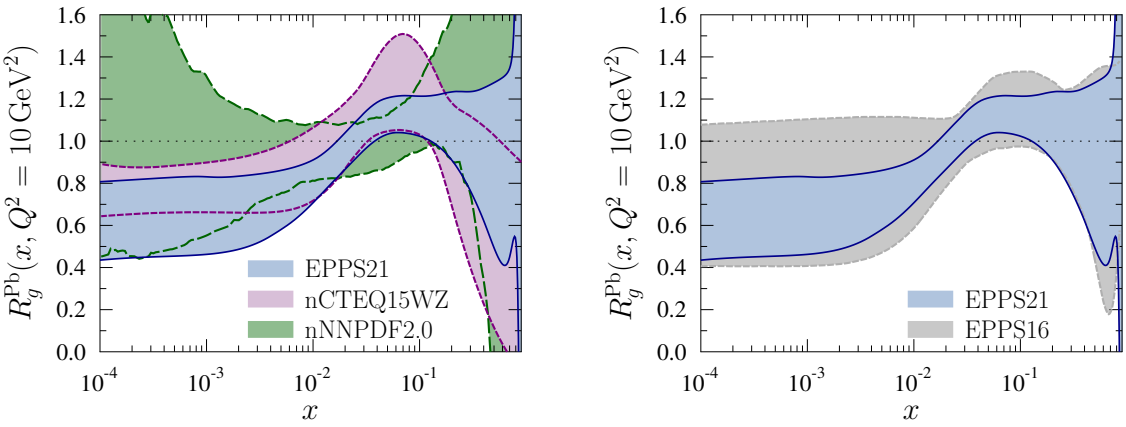

FIGURE 20 Comparison of gluon nuclear modification factor R_g^{Pb} calculated from EPPS21 [85], nCTEQ15WZ [88] and nNNPDF2.0 [89] (left). In EPPS21 the uncertainties are significantly improved in comparison to EPPS16 (right). Figures from [85], reproduced under the license CC BY 4.0.

for incoherent $\langle p_{\mathrm{T}} \rangle \approx 500$ MeV$/c$. For the low x studies especially the incoherent production channels is important to study the gluon shadowing effects. [90]

It has been suggested that J/ψ measurement is a good observable to probe the gluon PDFs since the J/ψ is proportional to the square of the gluon PDF in LO [91]. However, recent NLO calculations have shown that the J/ψ production is more complicated than what the LO picture has indicated [92]. At NLO, compared to LO, the quark contribution also becomes significant. New UPC measurement with FoCal can shed light into relative magnitudes of these quark contributions.

An important group of observables are correlations between different particle species that emerge from the collision. Particle correlations have been used widely in high-energy physics, in both jet and flow studies. Particle correlations can uncover information about the dynamics of the collision that single particle observables are not sensitive to. Therefore it is not a surprise that the sensitivity of correlations to the saturation regime also is something to consider.

The aim is to form the correlation between two particles coming out from the collision

$$A + B \rightarrow h_1 + h_2 + X, \tag{5}$$

where A and B are the projectile and target, for example, proton and lead ion. The final state after the collision includes the particles of interest h_1 and h_2, and other particles X that are not considered in the analysis. In this thesis, we consider correlation where two particles of interest are required to belong into trigger (t) and associated particle (a) bins so that $p_{\mathrm{T,t}} > p_{\mathrm{T,a}}$. For each trigger and associated pair we construct azimuthal angle and pseudorapidity differences $\Delta\phi = \phi_{\mathrm{t}} - \phi_{\mathrm{a}}$ and $\Delta\eta = \eta_{\mathrm{t}} - \eta_{\mathrm{a}}$, and form a per trigger normalized correlation function

$$\frac{1}{N_{\mathrm{trigg}}} \frac{\mathrm{d}^2 N_{\mathrm{pair}}}{\mathrm{d}\phi \mathrm{d}\eta} = \frac{1}{N_{\mathrm{trigg}}} \frac{S(\Delta\phi, \Delta\eta)}{B(\Delta\phi, \Delta\eta)}, \tag{6}$$

where the measured signal $S(\Delta\phi, \Delta\eta)$ is the number of pairs measured in the same event and $B(\Delta\phi, \Delta\eta)$ in the mixed event. The mixed event distribution is normalized such that $B(0,0) = 1$. Dividing the same-event distribution with the mixed-event distribution corrects

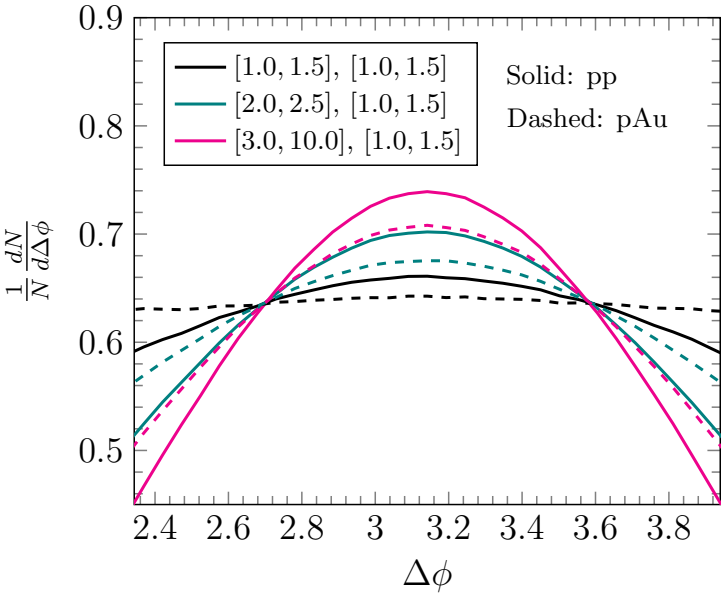

FIGURE 21 Calculation for dihadron correlations in forward rapidity with varying p_{T} bins. The calculation is done at RHIC energy of $\sqrt{s_{\mathrm{NN}}} = 200$ GeV. Figure taken from [93], reproduced under the license CC BY 4.0.

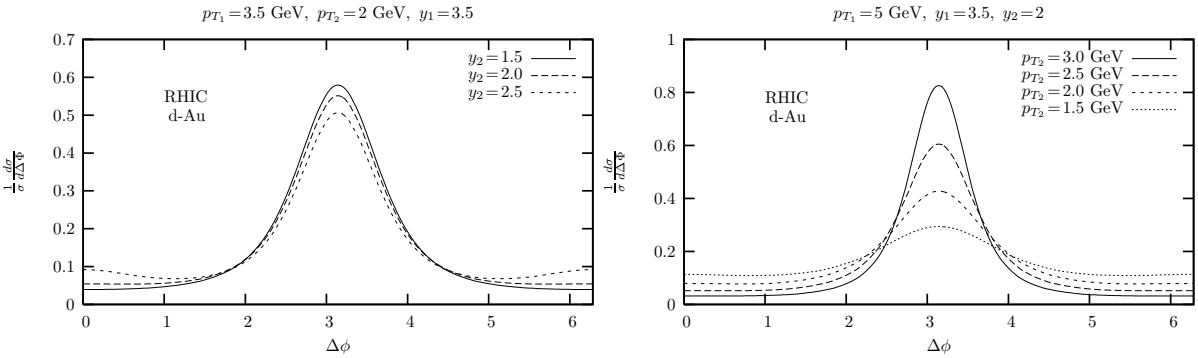

FIGURE 22 Calculation for forward rapidity dihadron correlations at RHIC kinematics. The figure on left shows the effect of varying rapidity by fixing the rapidity of the more forward particle in the correlation. Similarly the figure on right shows the effect of varying associated p_{T}. Reprinted with permission from [94], 2007, Elsevier.

for the effects from the finite η acceptance, and in the case of experiments various effects stemming from detector inefficiencies or holes in the acceptance. Experimentally these distributions are measured in all events where a trigger particle is found. A single event may contain more than one trigger unless the correlation is restricted to leading particle correlations.

When the correlation is considered in $\Delta\phi$, i.e. $\Delta\eta$ dependency is integrated out in Equation 6, two distinct regions can be recognized. Due to the jets from the initial hard scattering, it is more likely to find associated particles near the high-p_{T} trigger particles. These pairs form a peak around $\Delta\phi = 0$ and this region is usually referred to as the 'near side' of the correlation. Since the other parton coming out of the collision travels in the opposite direction, the particles from the developed jet form a low and wide peak on the 'away side', around $\Delta\phi = \pi$. The away side is lower compared to the near side because the longitudinal momentum distribution of partons causes elongation to the peak in $\Delta\eta$ direction [95]. Especially the away side is interesting since the suppression there will tell about the effects of the medium.

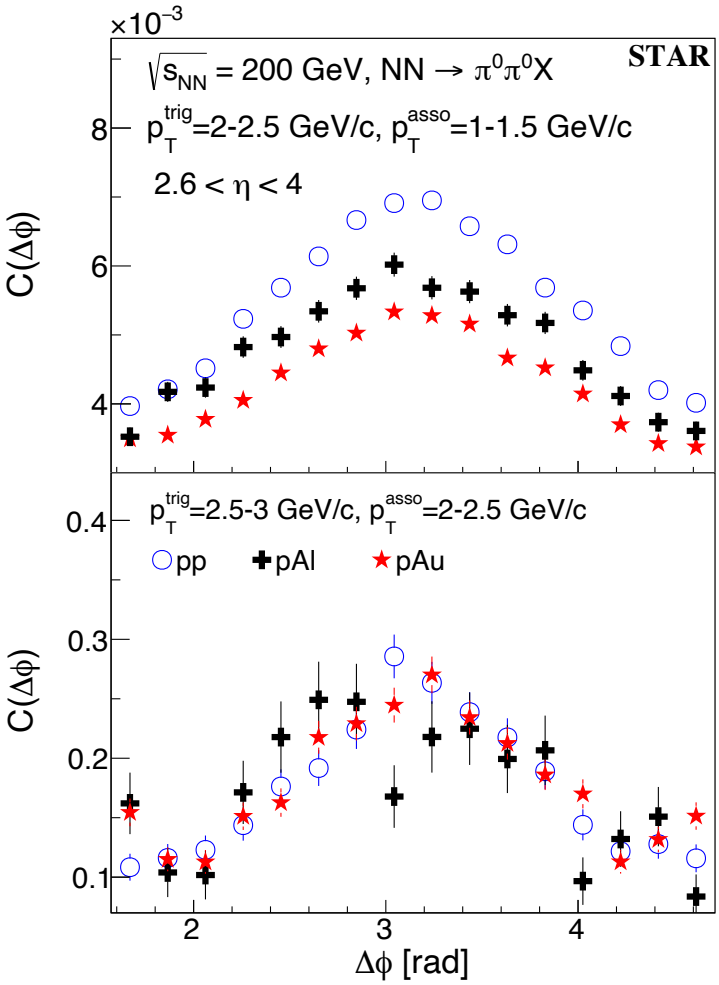

FIGURE 23 The away side of forward π^0–π^0 correlations measured by the STAR Collaboration at $\sqrt{s_{\rm NN}} = 200$ GeV. Reprinted with permission from [96], 2022, American Physical Society.

Figure 21 shows a CGC prediction [93] for $\pi^0 - \pi^0$ azimuthal correlation function for pp (solid lines) and pAu (dashed lines) at RHIC energy $\sqrt{s_{\rm NN}} = 200$ GeV. The saturation momentum $Q_{\rm s}$ grows proportionally to $A^{1/3}$, resulting in the broadening of the away side peak and more prominent suppression of the peak in pAu compared to pp. The same effect is expected to happen when Q_s is approached by measuring correlations at larger rapidity and/or lower $p_{\rm T}$. Stronger broadening and suppression can indeed be observed in the CGC calculation when comparing the lower $p_{\rm T}$ compared to larger values. The suppression on the away side for decreasing associated $p_{\rm T}$ can also be seen in the case of dihadron correlations, as the CGC calculation shown in Figure 22 suggests. The suppressive behaviour can also been seen when increasing the rapidity at fixed $p_{\rm T}$, although the effect is not as pronounced as in the case $p_{\rm T}$ comparison.

Figure 23 shows forward π^0–π^0 correlations measured by the STAR Collaboration at collision energy of $\sqrt{s_{\rm NN}} = 200$ GeV [96]. The away side correlation is compared between three collision systems in two transverse momentum bins. At lower momentum clear suppression can be seen in the case of pAl and pAu compared to pp. However, no similar broadening to the theoretical predictions is seen in the measured data. The differences between the collision systems vanish at larger $p_{\rm T}$ which is consistent with the notion that the saturation scale is probed at lower

momenta. In this thesis, the main focus is on the same neutral pion two-particle correlation in the context of FoCal. π^0–π^0 correlations are covered by Section 5.

3 FIT EVENT PLANE PERFORMANCE

One of the observables to be provided by FIT detector is the event plane. During Run 1 and 2 event plane was measured by VZERO and therefore naturally its successor FV0 would also be suitable for the task. In this Section, the simulated event plane performance of FV0 along with two other FIT detectors (FT0-A and FT0-C) is presented. Before going into details of the event plane determination and the simulation results, the physical meaning of the event plane is explained.

3.1 Collision geometry

A collision between two heavy ions in the transverse plane is depicted in Figure 24. The outcome of the collision is defined by the distance between the centers of the colliding nuclei (marked with $\times$ in the figure) as well as the placement of the nucleons inside the ions. The distance between the centers is referred to as impact parameter b and the plane defined by the impact parameter vector and beam direction is reaction plane Ψ_{RP}. The collision can be simulated via Monte Carlo Glauber approach [97] in which the nuclear density is parametrized by Woods-Saxon potential

$$\rho(r) = \rho_0 \frac{1 + w(r/R)^2}{1 + \exp((r-R)/a)}, \tag{7}$$

where ρ_0 is the nuclear density in the center of the nucleus, R the nuclear radius, a the skin depth, and w characterizes the sphericity of the nucleus. The nucleus is constructed by sampling the coordinates of the nucleons inside the nucleus via Equation (7). To simulate the collision both nuclei are constructed with impact parameter b and then the distances between nucleons from different nuclei are calculated to determine whether an interaction has taken place. The minimum distance for the interaction to happen depends on the inelastic nucleon-nucleon cross-section $\sigma_{\mathrm{inel}}^{\mathrm{NN}}$ which itself depends on the collision energy. Participants, the nucleons that partake in the collision then define the almond-shaped participant zone.

Due to the size of the system being only few femtometers both b and Ψ_{RP} are unobtainable directly from a measurement. Thus models such as Monte Carlo Glauber connect the measured quantities to the initial geometry. Values for nucleon-nucleon binary collisions N_{coll} and number

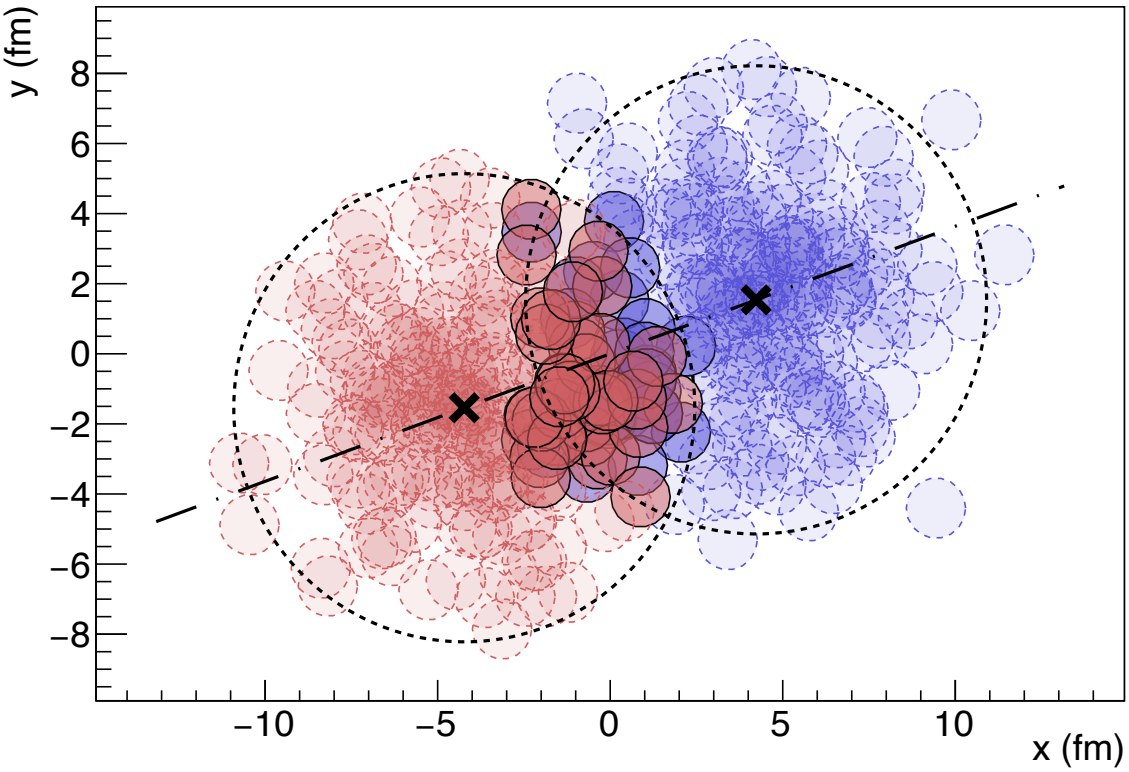

FIGURE 24 Geometry of lead-lead collision calculated using Monte Carlo Glauber model. The reaction plane is determined by the centers of the nuclei and the beam axis and is marked with the dashed line.

of participants N_{part} can be retrieved from the simulation and these values can be connected to measured event multiplicity. The sum of charge amplitudes measured by VZERO detector in the ALICE experiment, which depends linearly on the event multiplicity, is shown in Figure 25. The multiplicity distribution in pp collisions follows Negative Binomial Distribution (NBD) $P_{\mu,k}(n)$. Therefore the multiplicity in the case of heavy ions can be simulated by generating the number of particles per interaction n from NBD, by sampling it $N_{\text{ancestor}} = fN_{\text{part}} + (1-f)N_{\text{coll}}$ times. Here N_{ancestor} represents the number of independently emitting sources of particles. The free parameters μ, k and f are determined from fitting the simulated distribution $N_{\text{ancestor}} \times P_{\mu,k}(n)$ to the VZERO amplitude. The simulated distribution deviates from the measured data at low multiplicities because electromagnetic processes start to dominate there. The simulated distribution is thus normalized to the point where the hadronic cross section is 90 % of the total cross section. That defines the so-called anchor point from which onwards the VZERO amplitude distribution is divided into centrality classes from 0 to 90%, based on how the large amplitude range (in percentile) is taken from the distribution. For example, centrality class $0-5\%$ to corresponds events with the largest signal i.e. the most central collisions. [98, 99]

The centrality is an estimator for b of a heavy ion collision. The reaction plane estimator on the other hand can be determined from the collective behaviour of the particles, more specifically from the harmonic asymmetries in the azimuthal particle distribution discussed in Section 1.1. Elliptic flow, the second order harmonic v_2 in Equation (1) is the strongest component of the particle flow in the collision. Elliptic flow pushes the particles to the direction of the reaction plane and therefore the v_2 symmetry plane can be used to estimate the reaction plane. This

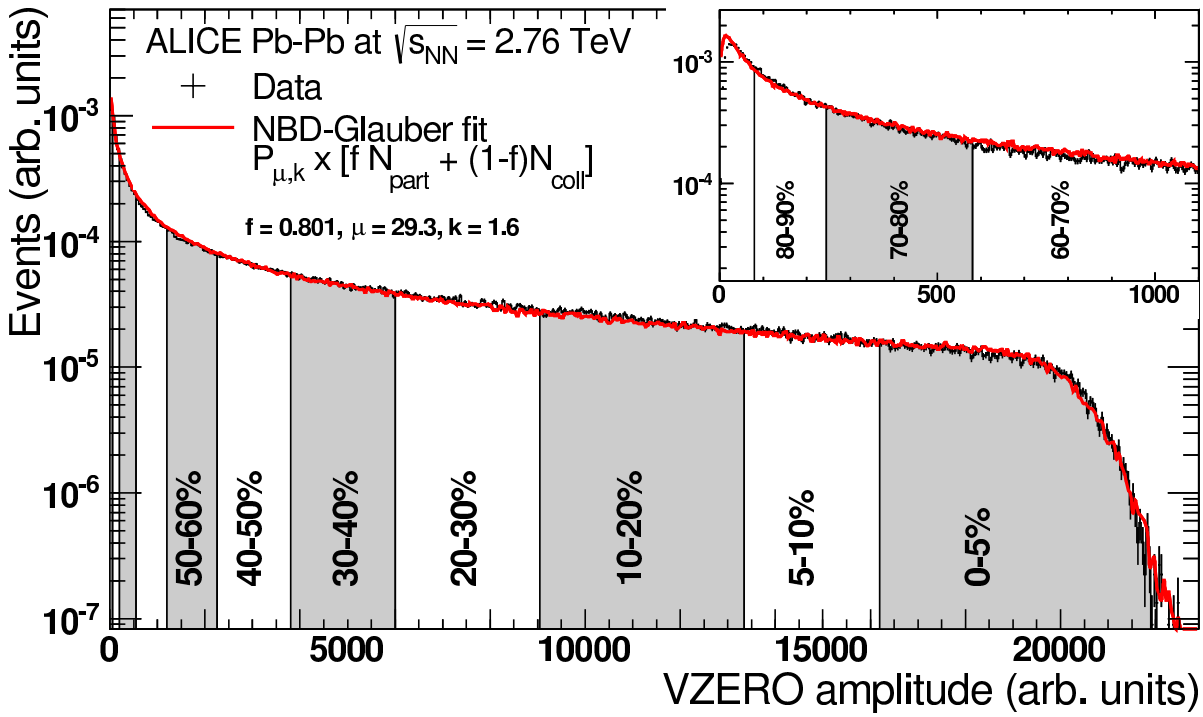

FIGURE 25 Measured VZERO amplitude in $\sqrt{s_{\mathrm{NN}}} = 2.76$ TeV Pb-Pb collisions [98]. The distribution is divided into different centrality classes depending on the amplitude strength. Figure reproduced under the license CC BY 4.0.

estimation is called the second-order harmonic event plane Ψ_2. Let it further be noted that the Ψ_2 is actually an estimation of the symmetry plane ψ_2. Second order symmetry plane ψ_2 is not the same as Ψ_{RP} since due to the fluctuations the participants are not symmetrically placed related to Ψ_{RP}. Thus the estimation can deviate from the Ψ_{RP}.

Since the event plane is related to the particle flow it has been traditionally used to estimate the flow also. However, the event plane method in flow studies has proven to be biased [100]. Nowadays more sophisticated methods such as multi-particle cumulants [101] are used instead. The cumulant method takes into account possible non-flow contributions in the measurement which cannot be excluded in the event plane method. However, the event plane information can be used, for example, to study jet modifications in QGP in relation to the symmetry plane [102, 103].

3.2 Event plane determination methods

The studies in this thesis cover only the second-order event plane Ψ_2. However, the methods used in event plane determination are described here in the more general notation, with nth harmonic. To determine the event plane for nth harmonic, Ψ_n, the first thing is to calculate the event flow vector (or Q-vector). Q-vector is defined as

$$Q_{n,x} = \sum_i w_i \cos(n\phi_i) \tag{8}$$

$$Q_{n,y} = \sum_i w_i \sin(n\phi_i) \tag{9}$$

where the sum is over all particles of the event. ϕ_i is the azimuthal angle of a particle in the sum. w_i is a weight that should approximate $v_n(p_\mathrm{T},y)$ and usually the particle p_T is chosen as the weight [17]. This is because $v_n(p_\mathrm{T},y)$ depends linearly on p_T at low momenta.

Q-vector represents the direction where the particle flow is strongest for the nth flow harmonic i.e. along the nth symmetry plane Ψ_n. Therefore Ψ_n can be calculated from the Q-vector components as

$$\Psi_n = \arctan\left(Q_{n,y}/Q_{n,x}\right). \tag{10}$$

The event plane angle can then be used to estimate the v_n. The flow components v_n are defined as

$$v_n = \langle \cos\left[n(\phi_n - \Psi_n)\right]\rangle, \tag{11}$$

where $\langle\cdots\rangle$ denotes the average over a large set of events. By replacing the unknown Ψ_n with Ψ_n we can measure the value of the flow component which is denoted as v_n^obs, to differentiate from the true v_n. The measured v_n^obs deviates from v_n because on average Ψ_n correlates with Ψ_n but can deviate quite substantially event-by-event. The deviation depends on the event multiplicity: Ψ_n is closer to the true value Ψ_n the more there are particles in the calculation. However, the particle multiplicity is finite and therefore is a limitation in the event plane calculation.

The observed v_n^obs can be corrected, on average, to correspond v_n by determining event plane resolution R_n. The event plane resolution depends on the properties of the detector that has been used in the event plane measurement. The resolution measures the difference between the estimated event plane and the true symmetry plane. It is defined as

$$R_n = \langle \cos\left(n(\Psi_n - \Psi_n)\right)\rangle. \tag{12}$$

The v_n^obs corrected with R_n then gives

$$v_n = v_n^\mathrm{obs}/R_n. \tag{13}$$

The problem in Equation (12) is again that the true value of Ψ_n is unknown. However, the resolution can be measured via the so-called subevent method [17]. The event planes calculated from different subsets of particles (subevents), for example from different detectors, are correlated because all particles of the event are correlated with the same symmetry planes. The two subevents should have an equal amount of particles because the resolution depends on particle multiplicity. If this requirement is met the resolution can be evaluated from the correlation, between Ψ_n^A and Ψ_n^B calculated from subevent A and B respectively. However, it may not be trivial to make the division into two equal subevents. In that case, the resolution can also be calculated utilizing three subevents in which the subevents can differ in multiplicity [17]. The resolution with three subevents is

$$\langle \cos\left(n(\Psi_n - \Psi_\mathrm{n})\right)\rangle = \sqrt{\frac{\langle \cos\left(n(\Psi_\mathrm{A} - \Psi_\mathrm{B})\right)\rangle \langle \cos\left(n(\Psi_\mathrm{A} - \Psi_\mathrm{C})\right)\rangle}{\langle \cos\left(n(\Psi_\mathrm{B} - \Psi_\mathrm{C})\right)\rangle}}. \tag{14}$$

The accuracy of event plane measurement is determined mainly by the multiplicity of the event and the strength of the flow component. The particle flow depends on the pseudorapidity [104, 105] and is strongest in mid-rapidity. Therefore it would make sense to determine the event plane and its resolution from mid-rapidity particles. However, the physics analyses utilizing

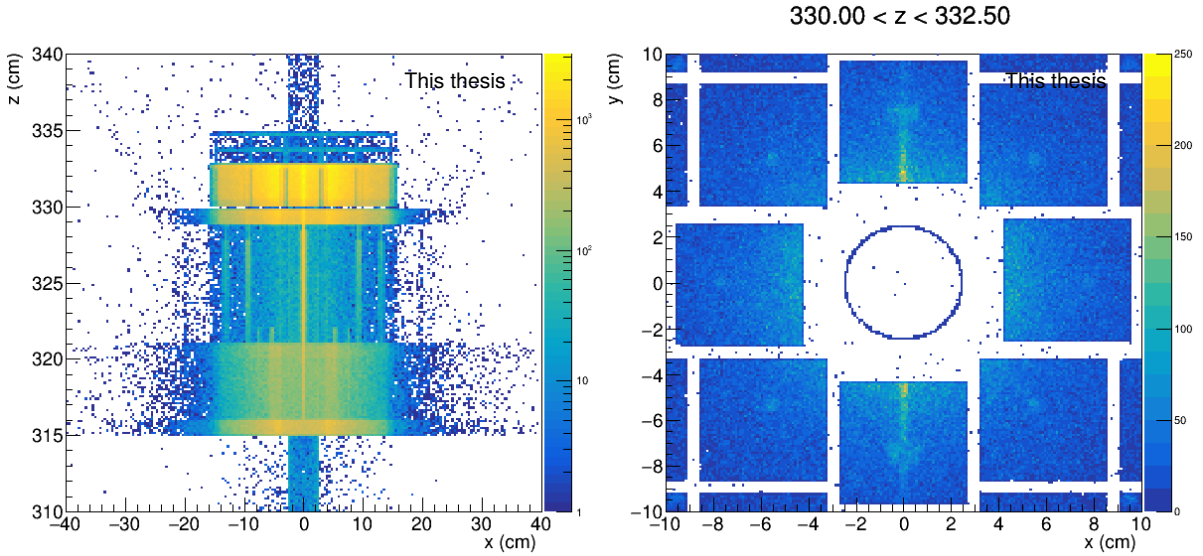

FIGURE 26 Secondary particle production vertices on the A-side (left figure) in which especially the middle part of FV0 case is visible. This can also be seen in the right figure which is a cross section of FT0-A.

the event plane information are usually done with the mid-rapidity particles. It is then better to do the event plane measurement at forward rapidities to avoid any autocorrelations. Thus the task would be best suited for the FIT subdetector system. In this study, the subevents are divided so that subevent A refers to the detector in which the event plane measurement is done, in this case, FV0, FT0-A or FT0-C. Subevent B and C are mid-rapidity particles, taken from $\eta = [-0.8, -0.1]$ and $\eta = [0.1, 0.8]$. This choice would correspond to the tracks taken from the TPC.

3.2.1 Q-vector corrections

The true reaction plane distribution should be isotropic since the beam particles hit each other randomly. Therefore the inclusive azimuthal particle distribution $\mathrm{d}N/\mathrm{d}\phi$ does not show any flow structures. However, the measured second-order event plane distribution $1/N_{\mathrm{ev}}\ \mathrm{d}N/\mathrm{d}\Psi_2$ can have a non-uniform shape. The geometry and the material of the detector may affect the distribution so that some event plane angles are favored more than others. This kind of effect may also occur if there are sources for secondary particle production. In the case of FIT, it was discovered that the middle part of the aluminium case of FV0 (see Figure 13) causes extra particle production in the vertical direction.

Figure 26 shows the secondary particle production on the A-side. The structures at $z = 315$ cm and $z = 330$ cm in the left side figure are related to FV0 aluminium case while the lines parallel to z-axis are the rods in the case. FT0-A is also a large source of secondaries and is visible at $z = [330, 335]$ cm. The middle part of the FV0 case, which can be seen clearly as the middle line at $x = 0$ on the left side figure, causes extra particles in the vertical direction. This kind of line is not visible in the $y - z$ plane. The secondary photons emerging from the structures cause a signal in FT0-A due to the electrons and positrons from pair production. This can be seen on the right side of Figure 26 where the secondary particle production is shown at $z = [330, 332.5]$ cm in xy-plane where FT0-A is located. The FV0 structures can be clearly seen from the secondary production. An additional test was conducted by leaving out FV0 from the simulation which

improved the FT0-A resolution and event plane distribution. Thus the casing does have an effect on the event plane measurement on the A-side.

These kinds of effects can be corrected by using methods to flatten the event plane distribution. In the case of flat event plane distribution, the (Q_x, Q_y) distribution would be symmetric and centered around the origin. Asymmetry in Q-vectors result in a non-flat event plane and thus the corrections need to be applied to the Q-vectors. These kinds of asymmetries include non-centered (Q_x, Q_y) and elongation of the distribution in some direction. The corrections are calculated from the non-corrected Q-vector distributions and then applied to the Q-vectors event by event. The corrections are the following [106]:

Recentering: is applied by subtracting the mean value of Q-vectors from the Q-vector in both x and y direction. Thus the recentered Q-vector components are

$$Q'_x = Q_x - x_{\text{corr}}, \quad Q'_y = Q_y - y_{\text{corr}} \tag{15}$$

where x_{corr} and y_{corr} are the mean values calculated over many events. After the correction, the Q-vector distribution in the Q_x–Q_y plane will be shifted so that the center of the distribution is at the origin.

Twist: corrects the possible rotation observed in the Q-vector distribution. This is done after the recentering using again predefined parameters (λ^-,λ^+) calculated from the uncorrected distributions:

$$Q''_x = \frac{Q'_x - \lambda^- Q'_y}{1 - \lambda^- \lambda^+}, \quad Q''_y = \frac{Q'_y - \lambda^+ Q'_x}{1 - \lambda^- \lambda^+} \tag{16}$$

Rescaling: corrects the last deformation in the distribution that might remain after the previous two corrections and that is the elongation of the distribution. Rescaling is done by dividing the Q-vector after the twist with rescaling parameter a^+ or a^-, depending on which component is in question:

$$Q'''_x = \frac{Q''_x}{a^+}, \quad Q'''_y = \frac{Q''_y}{a^-}. \tag{17}$$

The corrections are transformations in the Q-vector space and need to be applied in this order. The values for the correction parameters $a^\pm$ and $\lambda^\pm$ can be determined by solving a group of equations for uncorrected Q-vector [106].

A toy simulation was used to demonstrate how the different corrections affect the Q-vector and event plane distributions. The raw Q-vector distribution in Figure 27 was created by randomly sampling a two-dimensional Gaussian function that is elongated in y-direction and rotated in the clockwise direction. The correction parameters are then determined from this randomly generated Q-vector distribution and are then applied to the individual Q-vectors according to Equations (15)-(17). Each step corrects a different aberration in the distribution: firstly, the distribution is centered at $(x, y) = (0, 0)$ (recentering) and then it is rotated so that the distribution axes align with the coordinate axes (twist). Secondly, the elongation is corrected (rescaling) which makes the final distribution symmetric in both x and y directions. Figure 27 shows the Q-vector and event plane distributions after each step. As seen here after all the corrections the event plane is completely flat and therefore the methods work as intended. It was observed that in some extreme cases, the corrections were not able to fully flatten the event plane distribution. This happened when the distribution was very elongated and rotated. However, the

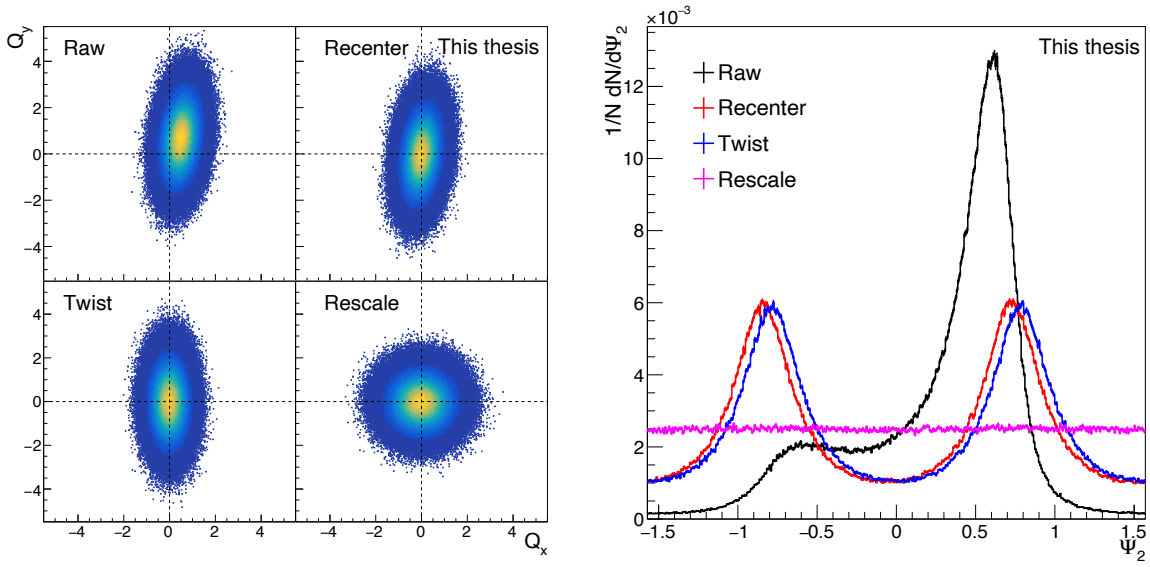

FIGURE 27 Validation of the Q-vector corrections using a toy model. The left side figure shows distributions of Q-vector x and y components after each correction, the top left panel showing the raw distribution. In the right side figure the event plane distribution calculated from the Q-vectors in the four different cases on the left is shown.

FIT simulations show very minor modifications to the Q-vector distributions and in that case Equations (15)-(17) are applicable.

3.3 Simulations

The simulations were carried out using the O^2 framework, which is the simulation and analysis framework of ALICE for Run 3. The initial collision is simulated with AMPT (A Multi-Phase Transport Model) generator [107] for Pb-Pb at 5.5 TeV. As the name suggests the routines in AMPT can be divided into four different phases. The initial conditions are first generated with HIJING (Heavy Ion Jet Interaction Generator) model [108]. Then the partonic scatterings are handled via ZPC (Zhang's Parton Cascade) model [109], and either Lund string model [110] or a quark coalescence model [111] can be used for hadronization. Lund string model is used in the default AMPT model whereas the AMPT model using the quark coalescence model is referred to as AMPT with string melting. We chose to use AMPT with string melting since it produces v_2 closer to measured values [107]. Consequent hadronic dynamics are implemented through ART hadronic cascade [112]. AMPT was chosen for these simulations due to the fact that it can produce v_2 signal that is consistent with the measurements at LHC energies [113, 114]. This is necessary so that the event plane information can be extracted from the particle flow.

Elliptic flow strength and thus the event plane resolution depend on the event centrality. Therefore it is meaningful to express the results as a function of centrality. In AMPT centrality can be adjusted by setting a minimum and maximum value to the impact parameter. The impact parameter values corresponding to the centrality classes used in this simulation are taken from Monte Carlo Glauber predictions done at 5.5 TeV [115].

Particle transport through the detector geometry is done by using GEANT4 [116] which will be discussed more in Chapter 4. After the particle transport, the output is run through a digitizer. Digitizer simulates the electronics in the detector and converts the hits in the detector's sensitive material into digital signals. The digital values from the detector channels are directly proportional to the total energy that incident particles have lost to the sensitive material in that channel. Since all we know from the detector output is the signal strength in each channel the Q-vector according to Equation (9) needs to be calculated not summing over the individual particles but over the detector channels. The Q-vector would then be

$$Q_{n,x} = \frac{1}{\sum_{ich} ADC_{ich}} \sum_{ich} ADC_{ich} \cos\left(n\phi_{ich}\right) \tag{18}$$

$$Q_{n,y} = \frac{1}{\sum_{ich} ADC_{ich}} \sum_{ich} ADC_{ich} \sin\left(n\phi_{ich}\right) \tag{19}$$

where ADC_{ich} and ϕ_{ich} are the signal value and the azimuthal angle of channel *ich* respectively. The angle of the channel is calculated from the center of the channel.

When running the digitizer for FV0 its dynamic range needs to be taken into account. In high multiplicity events such as Pb-Pb collision, the signal can be so large that the dynamic range is not enough and the signal saturates. This can be a problem, especially with the more central collisions in which the large particle multiplicities cause very large signals in the detector. Modification to the detector settings can be done so that the detector response for a single minimum ionizing particle (MIP) will be changed. In the simulation, this is done by changing how many ADC counts one MIP would correspond to. The default is in pp collisions 16 ADC counts per one MIP but for the Pb-Pb collisions, this is changed to 8 ADC counts per MIP. The effect of changing the gain can be seen in Figure 28 in which the charge distribution in all FV0 channels is shown in Pb-Pb collisions in the most central bin ($0-5\%$). If the default pp collision gain is used for Pb-Pb the signal saturates in all channels. Changing to 8 ADC counts per MIP will give a larger dynamic range in the Pb-Pb collisions but will in return worsen efficiency for single MIPs. With this setting in the simulation the signal in centrality $0-5\%$ fits the dynamic range in most channels though some channels will still be saturated (in centrality bin $5-10\%$ around 2% of the signal still saturates). With the default of 16 ADC/MIP the event plane resolution was worse up to 20 % centrality compared to the 8 ADC/MIP but no difference was observe at higher centralities between the two settings.

It should be mentioned that the simulations were performed with a slightly different geometry that is implemented in the framework at the moment. The PMTs were included in the geometry after we ran the simulations and the FV0 fibres were redistributed to better correspond to the final setup. Also, the location of FIT-A was moved approximately 4.42 cm in z direction from the previous location. This is because there was a need to access the ITS electronics in December 2021 and for that FIT-A needed to be removed and reinstalled after the access. The change in placement could in principle affect the event plane measurement and therefore the possible effect needed to be checked. We ran the simulation with the new setup in one semi-central bin and concluded that the change in event plane resolution is negligible, and hence the simulation was not repeated over the full centrality range.

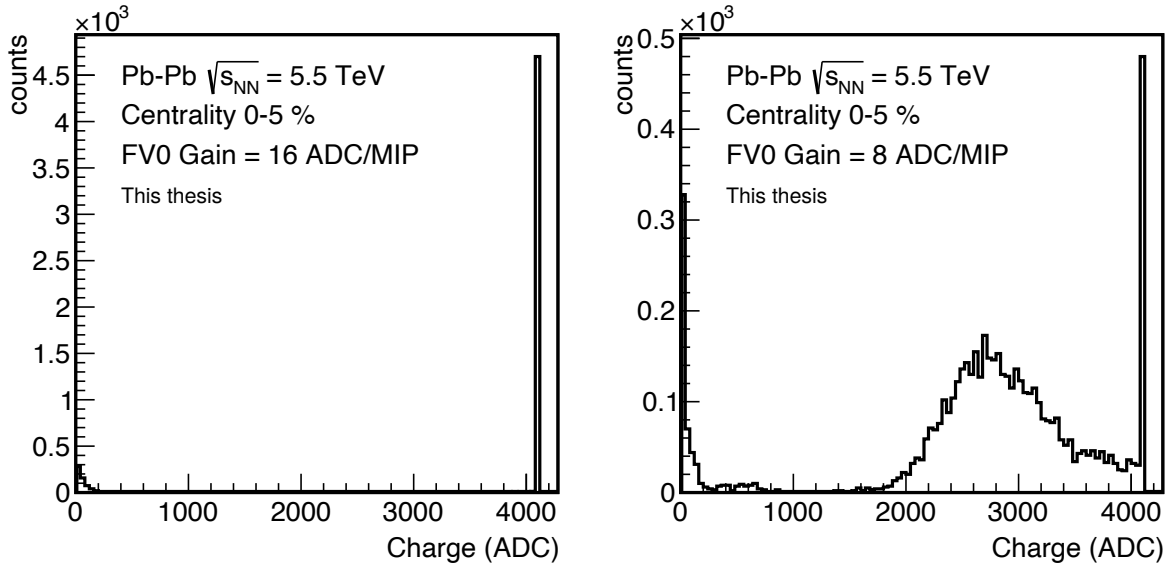

FIGURE 28 Simulated charge from all the FV0 channels with two different gain settings, one MIP corresponding to 16 ADC counts (left) and 8 ADC counts (right).

3.4 Results

The simulated event plane resolution for three FIT sub-detectors is shown in Figure 29a. FT0-C resolution is the highest whereas the A-side detectors have a bit lower values. It was expected that, since FV0 has the largest acceptance with the highest multiplicity, the resolution would be the best out of the three detectors. This is the case when the resolution is calculated from charged MC tracks in each detector's acceptance (Figure 31, left side). The results from Figure 29a have been included to see the difference between the ideal resolution from MC tracks versus the detector level resolution from digits. The largest drop in resolution can be observed in FV0. This can be caused by several reasons. Firstly, finite granularity reduces the resolution. Secondly, the channels in the outmost ring of FV0 are physically larger which leads to signal smearing. The event plane calculation is based on the measurement of signal strength in the channels and therefore the signal smearing might be the reason behind the worsening resolution.

Since FV0 is quite similar to VZERO-A from the Run 1 & 2 setup measured VZERO-A resolution gives a baseline if the simulated resolution for FV0 is reasonable. FV0 simulation gives 10% to 15% larger resolution than measured VZERO-A [72] values depending on the centrality. This is expected since FV0 has a larger acceptance than VZERO-A. There is also a difference in multiplicity between the two datasets since the simulation is performed in larger center-of-mass energy than the V0-A measurement at 2.76 TeV. In any case, the result for FV0 seems consistent with what has been measured previously.

In Figure 29 results the Q-vectors have been corrected using the corrections presented in Section 3.2.1. The simulated Q-vectors for the detectors were already quite symmetric in (Q_x, Q_y) plane except for FT0-A, as can be seen in Figure 30. The FT0-A Q-vector distribution is slightly off-centered which leads to a quite significant change in the event plane distribution. The corrections needed are not large but as shown in the bottom panels of Figure 30 the corrections are able to flatten the event plane distribution. This can also be seen in Figure 31 (right fig-

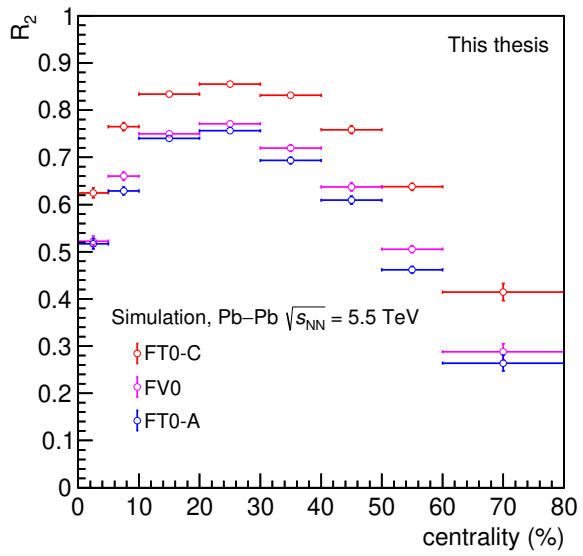

(a) Event plane resoluton calculated using the three-sub event method.

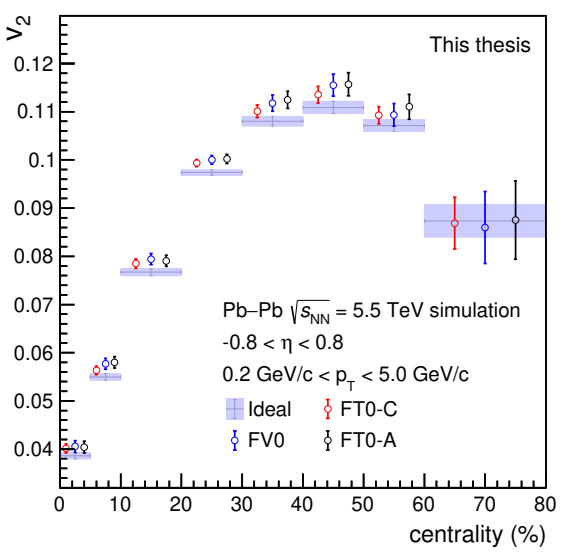

(b) Elliptic flow v_2 corrected with the resolutions in Figure 29a. For comparison ideal v_2 corrected with resolution from an imaginary, very large acceptance forward "detector" is also included.

FIGURE 29 Final simulation results for three FIT detectors FT0-A, FT0-C, and FV0.

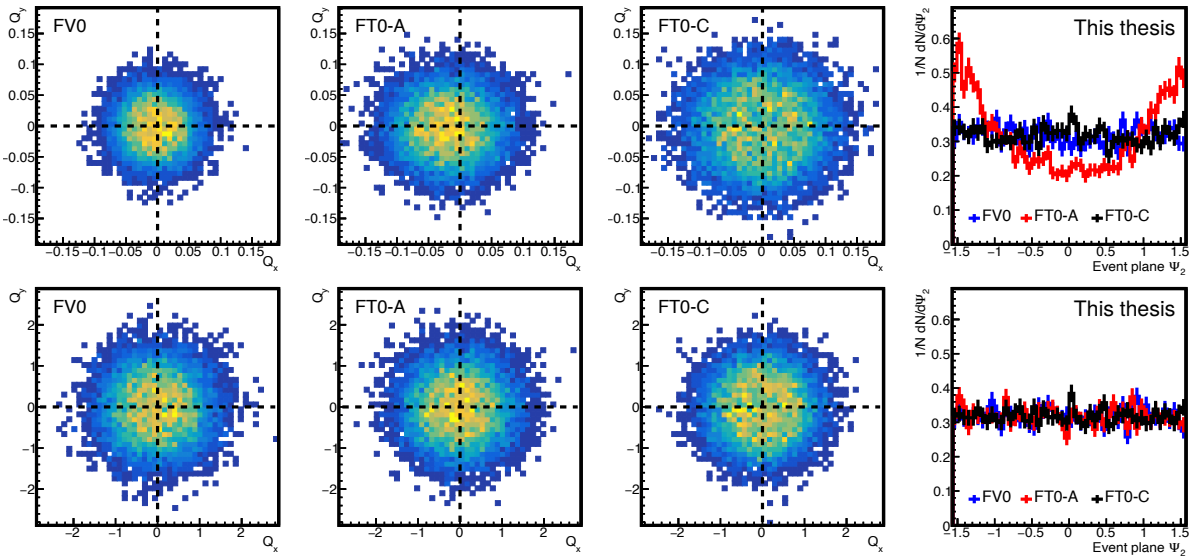

FIGURE 30 Q-vectors and Ψ_2 distributions from the O^2 simulations in centrality $20-30\%$ for the three FIT detectors. The raw distributions are shown on the top row while the distributions after the corrections are on the bottom row.

ure) where the event plane resolution with corrections is compared to the resolution without any corrections to the Q-vectors. FV0 and FT0-C resolutions with corrections align with the non-corrected counterparts but the corrected FT0-A results differ from the non-corrected results $\sim 8\%$ in the most central bin. The difference decreases when the centrality class increases and at $50-60\%$ centrality the correction has no effect on the resolution.

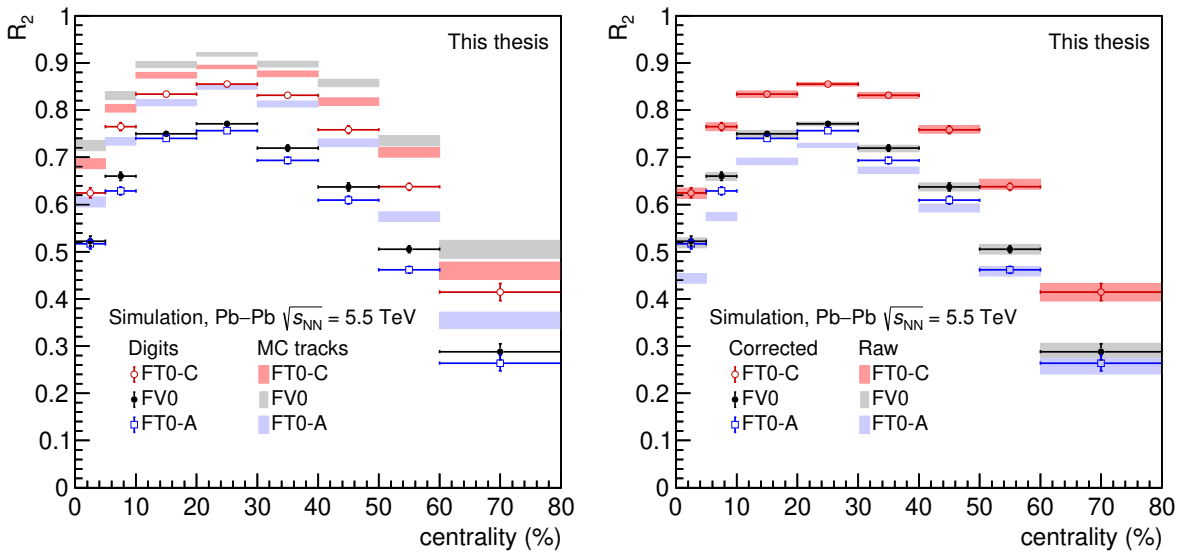

FIGURE 31 The final corrected event plane resolution compared to the resolution calculated from charged MC tracks in the acceptances of each detector (left). Similarly, the final result is compared to the resolution without any corrections to Q-vectors (right).

3.4.1 Recovery of elliptic flow v_2

The obtained resolution should be able to recover the true value of v_2 when the observed v_2^{obs} is divided by the resolution. The true value for v_2 could be retrieved using the true reaction plane Ψ_{RP} but this parameter was not saved to the simulation output. Instead, the primary particles from the AMPT generator were used to calculate an ideal value for v_2^{obs}. Instead of taking the event plane information from the detector signal the subevent A was formed from the primary particles from $-6 < \eta < -1$ and $1 < \eta < 6$. Larger acceptance ensures larger multiplicity which in turn results in higher resolution and more precise estimation for the reaction plane.

Figure 29b shows v_2 calculated using Equation (13) using event plane information from different FIT detectors. The ideal value is also presented in the figure. v_2^{obs} is calculated the same way in each case, using MC tracks in TPC acceptance ($-0.8 < \eta < 0.8$) with p_{T} ranging from 0.2 GeV/c to 5.0 GeV/c. v_2 calculated from using the detector resolution slightly overestimates the ideal value. This might indicate some detector effect that is not corrected using the corrections presented in Section 3.2.1.

Out of the three detectors FT0-C value seems to be closest to the ideal value but it is still within the uncertainties of FV0 and FT0-A. The A-side detectors have similar values in most bins. Without the corrections, the value of FT0-A would be slightly higher which means that for FT0-A corrections work as intended.

3.4.2 Effect of dead channels on FT0 event plane performance

In the simulation, all the detector channels are working and their responses are similar. In reality, channels might experience a loss in efficiency or even break. Changing or fixing parts would require lots of effort since the detectors should be moved and the cabling would need to be done again. For that reason it is not plausible to do minor modifications after the installation, the reasons for that kind of task would require problems that severely affect the performance.

At the end of 2012, VZERO was observed to have a drop of 10 to 40% in signal amplitude, depending on the channel [72]. The reason was traced back to the deterioration of the PMTs used for the light collection, only a few percent of the loss was contributed to the deterioration of the scintillation material. The loss was compensated by rising the bias voltage of the PMTs but the ageing problem needed to be taken into account in the design of FV0. The PMTs chosen for FV0 should not age that quickly, the newer Hamamatsu PMTs are expected to perform better on that front [76]. The MCP-PMTs used in FT0 have shown signs of ageing which can be corrected in the case that they do not completely fail.

The effect of ill-performing channels in FT0 was studied via simulations to see what would happen to the event plane performance in the situation of an efficiency drop. The breakage of FT0 channels was simulated by randomly selecting channels that would be left out of the analysis. Channels near the beam pipe are more likely to experience efficiency losses and breakages since the radiation load is larger for them than the further channels. The ageing of the photosensor has been studied before via measuring their integrated anode charge (IAC) [76]. To take the radiation load into account in the simulation each channel was weighted with their respective IAC value which makes the channels with higher values more likely to be selected as dead channels.

The performance was studied in four different scenarios, where 10%, 25%, 50%, or 75% of the detector channels would not work. FT0-A and FT0-C are studied in this case independently, selecting dead channels from both sides would favor the A-side array since its IAC values are higher. The results are shown in Figure 32 for both sides, along the ideal situation with no dead channels. Q-vectors have been corrected using the corrections described in Section 3.2.1. FT0-A and FT0-C perform well even if 10% or 25% of the channels are out of order, the drop is less than 5% on both sides. At 50% the resolution starts to decrease though in FT0-C the decrease is still less than 10%. In the last case, most of the detector is not functioning but still, FT0-C has a harsh resolution; for FT0-A the calculation fails in most bins.

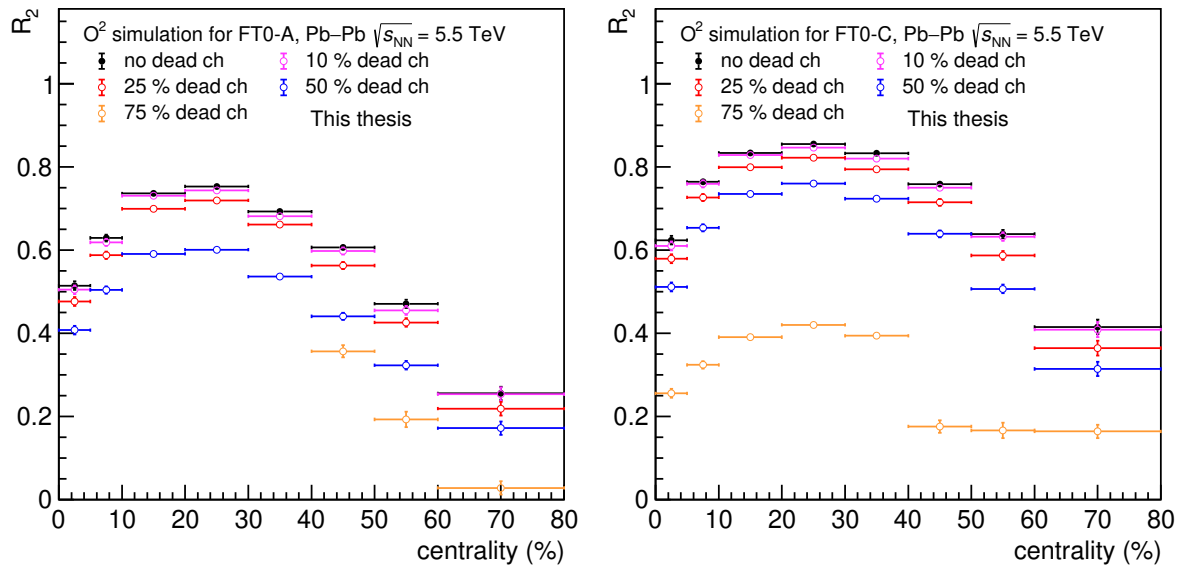

FIGURE 32 FT0 event plane in different cases in which the channels have been left out from the analysis. The left figure shows the results for the A-side and the right for the C-side.

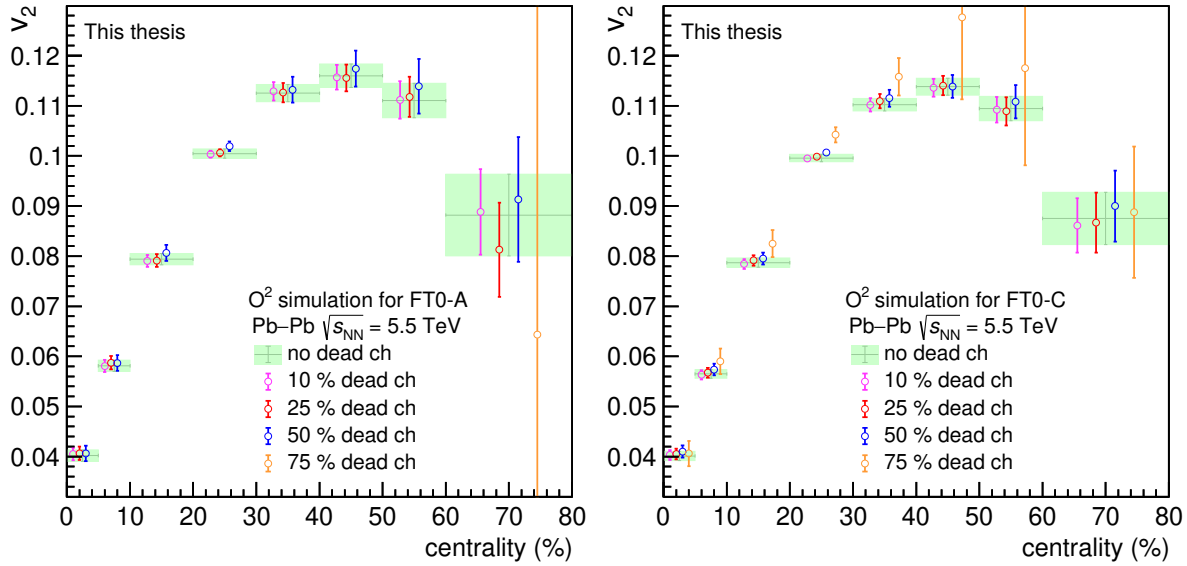

FIGURE 33 v_2 calculated using event plane calculated from FT0 in a different case in which the channels have been left out from the analysis. The left figure shows the results for the A-side and the right for the C-side.

To see how this would affect the physics v_2 was also calculated in each of these cases. The v_2 values are presented in Figure 33, again for both sides individually. As with the resolution, v_2 starts to deviate from the ideal case in the 50% case and at 75% v_2 is not recovered. However, the event plane measured with FT0-C is still able to recover v_2 to some extent after the Q-vector corrections.

In a scenario in which over half of the channels are broken, there would mean that there is something severely wrong with the detector and it would not be used for data taking in that situation. This study demonstrates that FT0 can reliably measure the second-order event plane and its resolution and it would fail only in very extreme situations.

4 FOCAL TEST BEAMS

In addition to FIT, the Forward Calorimeter FoCal introduced in Section 2.3 will be operating during Run 4 on the A-side i.e. towards the ATLAS experiment in ALICE cavern. The coordinate system in ALICE is defined such that A-side corresponds to positive rapidities. In order to meet the physics goals set to FoCal there needs to be a good understanding of its performance. Therefore to ensure that FoCal will operate as intended during the physics runs the components need to be tested extensively. Testing the detector parts gives output about the performance of the sensors and the readout. These tests are also essential to uncover possible problems that might be present in the sensor itself or in the electronics, for example how they react to the temperature during the operation.

In this chapter, the concepts in calorimetry important for the test beams are first introduced. Then the results from two test beams held in CERN during 2021 and 2022 for FoCal prototypes are presented. The test setups include sensors from both the FoCal-E and FoCal-H. My analysis only covers the pad sensors of the electromagnetic part. Before going through the analysis procedure and the results the quantities that are interesting from the test beam point of view are reviewed.

4.1 Calorimeter characterization

Particle detection with a calorimeter is based on measuring the energy deposited by a traversing particle in the calorimeter material. A calorimeter can be built entirely from the active material from which the energy deposition is measured (homogenous calorimeter), or it can be complemented with another, passive absorber material to produce particle showers from the particle (sampling calorimeter). There are numerous ways to construct both types of calorimeters: the active material can be made of liquid (organic scintillators, water), solid (inorganic crystals, semi-conductors), or gases. In the case of sampling calorimeters, there are several materials used as absorbers (e.g. Cu, Fe, Pb, W) and with the choice of the absorber material the shower development can be adjusted. Due to their versatility in customization, and providing energy and space measurements, calorimeters have been widely used in particle and nuclear physics. [117]

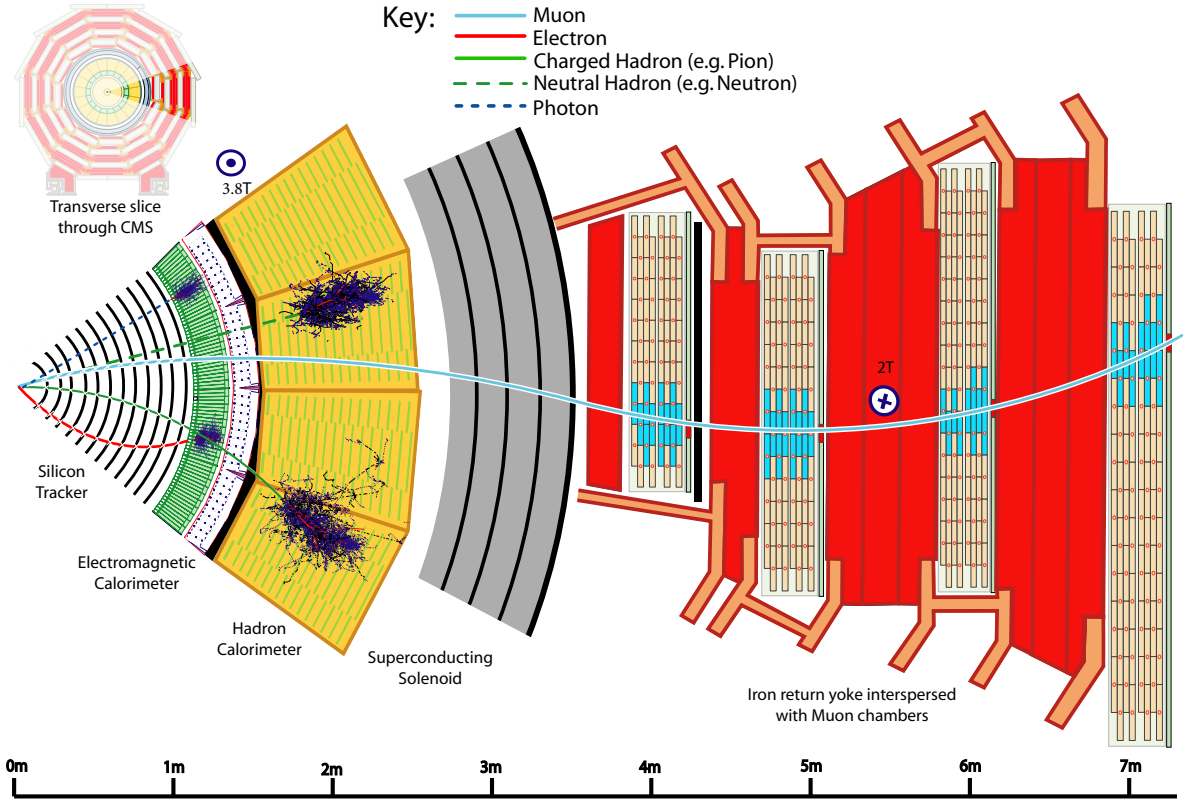

FIGURE 34 Illustration of CMS central calorimeters, showing one slice of the detector in the transverse plane. Particle identification is based on how the particle track bends in the magnetic field and in which layer the signal is measured. Image taken from [120], reproduced under the license CC BY 3.0.

In the end what dictates the calorimeter design is what is the purpose of the experiment. Homogenous calorimeters are widely used in low-energy nuclear physics due to their excellent energy resolution. Good examples in the field of particle physics are large neutrino detectors such as water Cherenkov detector Super-Kamiokande [118] which demands a large amount of active material for detecting rare neutrino processes. In accelerator-based particle physics inorganic crystals such as $PbWO_4$ are being used in for example CMS electromagnetic calorimeters [119]. Examples of sampling calorimeters can be found in the HEP experiments. They are well suited for detecting high energy particles due to their short radiation length X_0 which represents how long the particle can travel in the material [117]. For this reason, sampling calorimeters are more cost and space effective for HEP. FoCal-E for example, as described in Section 2.3 has alternating layers of silicon and tungsten to produce and detect particle showers from electromagnetic particles.

Instead of categorizing calorimeters in the way they are built, they can also be divided into two groups depending on what kind of interaction produces the signal. Electromagnetic calorimeters can be used to detect particles via electromagnetic interaction and hadronic calorimeters are for detecting strongly interacting particles. Thus usually in larger HEP experiments several different detectors are needed in the setup to measure several processes in the particle collisions. This approach can be seen in Figure 34 which shows a slice of the CMS central detectors in the transverse plane. To detect the electromagnetic particles (photons and electrons) an electromagnetic calorimeter is needed. To detect the hadrons the electromagnetic part is usually

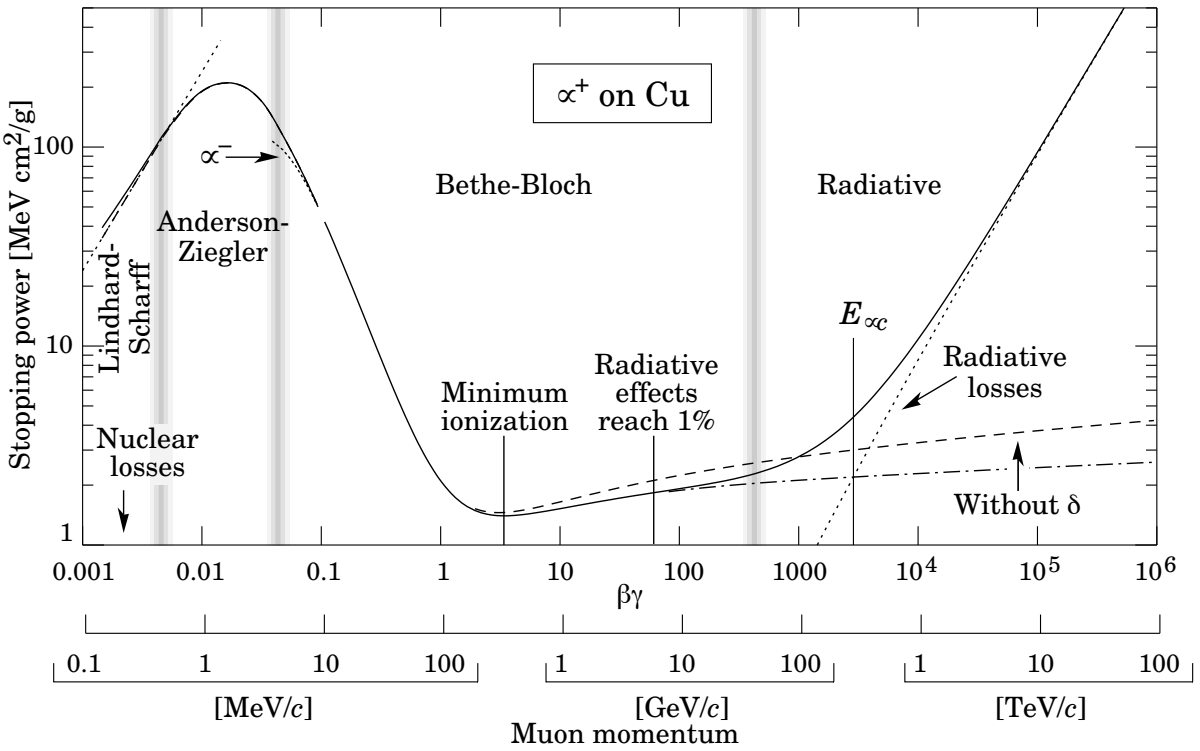

FIGURE 35 Stopping power $-dE/dx$ as a function of positive muon momentum in copper [121]. Figure reproduced under the license CC BY 4.0.

accompanied by a hadronic calorimeter. Hadrons have a larger mass than electrons and photons and thus to contain the particle shower produced by them the material budget in the hadronic part needs to be larger than in the electromagnetic one. Most of the particles are at the latest stopped by the hadronic calorimeter but muons can travel much farther. If it is in the interest of the experiment to measure muons (which is the case with CMS) the outmost layer will be a muon detector.

The particle showers produced in the calorimeter via different particles can hardly be distinguished from each other. For example, a shower in an electromagnetic calorimeter can be either from an electron or a photon. It should be also noted that hadrons as well can create a shower in the electromagnetic part but will usually travel through leaving a small signal (more about the minimum ionizing in the next section) and shower later in the hadronic part. For particle identification, a tracker with a magnetic field is needed in front of the calorimeters so that the tracks can be matched to the calorimeter showers. In ALICE trackers are placed only in the central barrel at rapidity $-0.8 < \eta < 0.8$. FoCal will then not be able to distinguish different showers. However, the separation between electrons and photons could be made by placing one pixel layer in front of FoCal-E, before any tungsten plates. Electrons would leave a signal to the pixel layer but photons would only go through. Matching the signal with the showers could then provide the capabilities to identify the shower origin but it has not yet been fully explored if this is necessary for reaching the physics goals presented in Section 2.3.1.

During the test beams, FoCal response was tested for both electromagnetic and hadronic interactions. In the case of FoCal-E, it is important to test with an electron beam to get an estimation of its energy resolution. However, measuring hadrons with the electromagnetic part also provides useful information since they act as minimum ionizing particles. This is an important measure

to see that the actual physical signal is observed during the measurement. Both the minimum ionizing and energy resolution were investigated for FoCal-E, therefore these parameters are reviewed here in more detail.

4.1.1 Minimum Ionizing Particle

The mean energy loss through inelastic and elastic atomic collisions per unit length is known as stopping power $-dE/dx$ and can be described by the Bethe-Bloch formula [122]. Figure 35 shows the Bethe-Bloch formula plotted against the momentum of the particle traversing the material, in this case, muon with a positive charge in copper. The muon reaches its minimum stopping power around $\beta\gamma \sim 4-5$ and this holds for all particles with the same charge [122]. Stopping power does not increase considerably until the momentum reaches hundreds of GeV$/c$, when the radiative effects start to come into play. In this momentum range muon will pass through matter with a minimal deposit of energy and is referred to as a minimum ionizing particle (MIP). Even though the mean energy loss depends on the particle species most ultra-relativistic particles have energy losses close to the minimum ionization. Therefore in practice, ultra-relativistic particles at accelerators can be treated as MIPs.

The importance of MIPs comes from the fact that this is the smallest physical signal that the detector is able to pick up. Signals with lower values than MIP are regarded as background noise. The signal from detectors varies from a detector to detector and even from channel to channel and to get meaningful energy measurements the signal needs to be calibrated correctly. Since the energy losses are well known and can be simulated for different geometries the measurement of MIP provides means for energy calibration of the detector channels. Results from simulations are used to relate the detector response to energy. Figure 36 shows the simulated response of a 20 layer FoCal tower. The figures of the geometry on the left side demonstrate the difference between electrons and hadrons, in this case, protons. At this energy electron (and

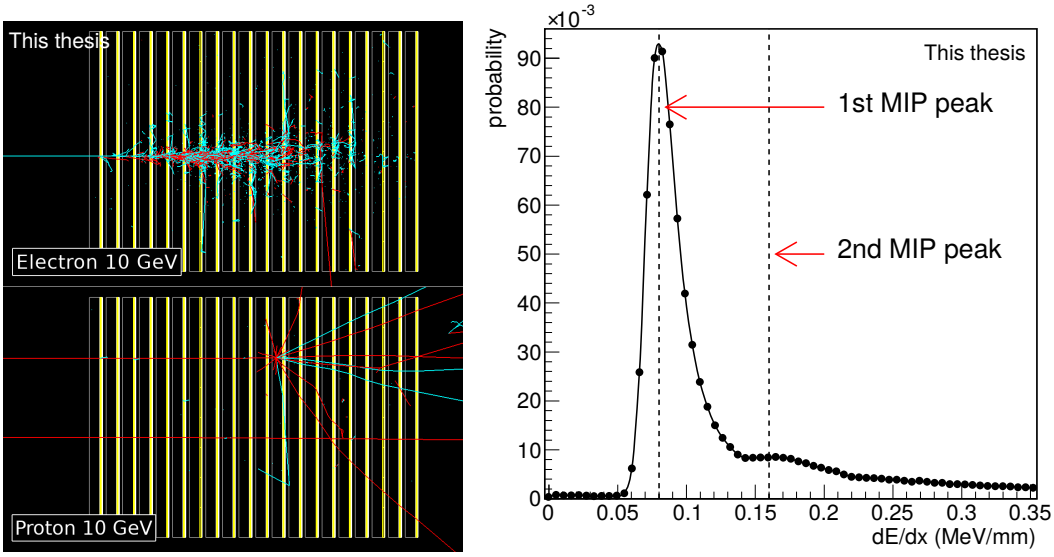

FIGURE 36 Simulated MIP response of one FoCal pad channel. The figure on the left side shows 10 GeV electron and proton from a Geant4 simulation. In the proton case, two different events are shown. On the right figure is the distribution of energy deposited by protons in the last layer of the setup.

also photon) tends to form a particle shower in the material. Proton on the other hand typically passes through the material without showering and leaving only minimal energy to the layers.

The figure on the right side shows the energy loss by the simulated protons to the last layer of the geometry shown on the left side figure. Since the hadrons from time to time can create showers and then deposit more energy to the layers the energy distribution has a long tail continuing to the larger energies. The distribution can be described by Landau distribution [123] which takes into account also the tail. In addition to the clear MIP peak, there appears another peak that arises when two MIPs pass through the material in the same event. The most probable value of the second peak is around two times the value of the first peak and is more visible in the last layers since the protons have a higher chance to shower there and produce additional particles. Thus in reality the energy distribution is described by a sum of several Landau distributions, with the peak positions at $1 \times E_{\mathrm{MIP}}$, $2 \times E_{\mathrm{MIP}}$, and so on.

In addition to the physical signal from the particles, the sensors will pick up noise from the environment and electronics. Thus to utilize the MIPs in the calibration the electronics must be adjusted so that the MIP signal will be larger than the noise level. This will then determine the sensitivity of the detector.

4.1.2 Energy resolution

One of the most important aspects of a good calorimeter is the resolution in which it can measure the energy of the traversing particle. The energy resolution is the standard deviation of the energy response divided by the mean energy response and is parametrized as [117]

$$\frac{\sigma(E)}{E} = \frac{a}{\sqrt{E}} \oplus \frac{b}{E} \oplus c. \tag{20}$$

a, b, and c are parameters that need to be determined experimentally for the detector. The energy resolution is then defined by these three different terms that are summed together in quadrature (marked with $\oplus$). An excellent explanation of the terms is given in [117], here they are covered shortly based on the reference.

The three terms in Equation (20) have different interpretations. The so-called stochastic term $a/\sqrt{E}$ represents the intrinsic energy resolution of the calorimeter and it depends on the signal fluctuations. In homogenous calorimeters, this term is the only order of a few percent because the whole particle energy is deposited to the medium. For sampling calorimeters, this term usually dominates the energy resolution at low energies. This is because the absorbing layers cause more variation in the energy response. The stochastic term can be reduced by having more layers with thinner absorbers in each.

The second term, b/E, is the noise term and, as the name suggests arises from the electrical noise the sensors pick up. The noise term is affected by the signal collection method. Low noise detectors such as photomultiplier tubes (PMTs) provide low noise terms but sensors which collect the charge directly and use a preamplifier to enhance the signal can have large noise terms. The noise term can be in that case reduced by some amount by having a larger signal from the deposited charge. In sampling calorimeters, this can be achieved by increasing the amount of active material.

TABLE 1 Energy resolutions for various calorimeters in different high-energy experiments. The information is grouped so that the first group is upcoming detectors, the second group includes existing calorimeters from LHC experiments and the last group from RHIC PHENIX experiment.

Calorimeter	Stochastic term	Noise term	Constant term	Details	η
ALICE FoCal [46]	27.0%	–	1.0%	Si-W, 20 layers, Si thickness: $290-300$ µm, 20 X_0	$3.5 \leq \eta \leq 5.8$
CMS HGCAL [124]	19.9–24.3%	–	0.6–0.8%	Si-W-Cu, 28 layers, Si thickness: $100-300$ µm, 26 X_0	$1.5 \leq \eta \leq 3.0$
ALICE EMCAL [125]	11.3%	4.8 %	1.7%	Scintillator–Pb, 77 layers, 20 X_0	$\lvert\eta\rvert \leq 0.7$
ALICE PHOS [125]	1.8%	3.3 %	1.1 %	$PbWO_4$, 20 X_0	$\lvert\eta\rvert \leq 0.12$
CMS ECAL (barrel) [119]	2.7%	–	0.55 %	$PbWO_4$, 26 X_0	$\lvert\eta\rvert \leq 1.48$
CMS ECAL (endcap) [119]	5.7%	–	0.55 %	$PbWO_4$, 25 X_0	$1.7 \leq \eta \leq 3.0$
ATLAS LAr EMCAL [126]	10.0%	–	0.7 %	LAr–Pb, 22 X_0	$\lvert\eta\rvert \leq 3.2$
PHENIX EMCAL(PbSc) [127]	8.1%	–	2.1%	Scintillator-Pb, 66 layers, $18X_0$	$\lvert\eta\rvert \leq 0.35$
PHENIX EMCAL(PbGl) [127]	5.9%	–	0.8%	Pb-Glass Cherenkov	$\lvert\eta\rvert \leq 0.35$

The last one is the constant term. This term represents variations that do not depend on the energy of the incident particle. The variation can be caused for example by irregularities in detector geometry, temperature changes, radiation damage, sensor ageing etc. This term becomes important when measuring particles with very high energy and thus in high-energy applications, it should be small, around 1%.

Table 1 lists the individual energy resolution components for selected calorimeters across different experiments. We can see that the stochastic term for FoCal is the largest out of these detectors while the magnitude of the constant term is close to the average within the given examples. The high granularity calorimeter upgrade HGCAL is similar to FoCal in terms of resolution. These both are sandwich calorimeters which tend to have worse energy resolution at low energies compared to homogenous detectors as explained. For example, ALICE PHOS and CMS ECAL are assembled from long lead-tungstate crystals ($PbWO_4$) in which the fluctuations are not as large as in a sandwich calorimeter. However, in the case of CMS HGCAL, there are more layers with a smaller thickness which results in a larger sampling frequency and thus better intrinsic resolution.

CMS electromagnetic calorimeters possess similar attributes to ALICE PHOS, being made of $PbWO_4$ and therefore having similar resolutions. ATLAS electromagnetic calorimeter however

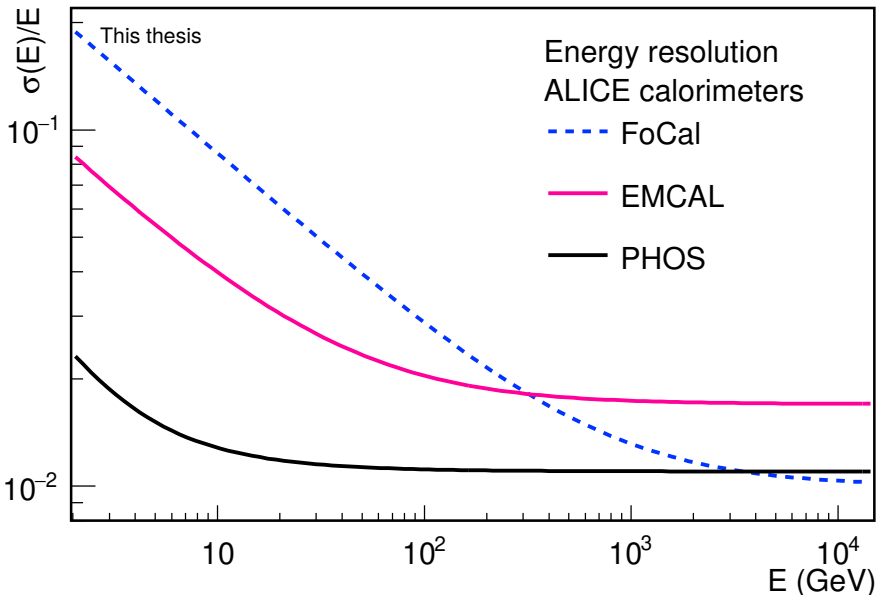

FIGURE 37 The energy resolutions of ALICE calorimeters.

is a sandwich calorimeter with an accordion structure, using liquid argon as the active material. The stochastic term is then characteristic to a sandwich calorimeter and is similar to ALICE EMCAL.

Similarly to the ALICE experiment the PHENIX experiment takes advantage of both sampling and homogenous calorimeter technologies in the design of their electromagnetic calorimeter. This enables the cross-check of results within the experiment [127]. Four out of the six sectors in the calorimeter are lead-scintillator sampling calorimeters with 66 layers while two sectors use homogenous Cherenkov detectors made of lead glass. In principle, ALICE EMCAL should provide better resolution based on the number of layers compared to PHENIX EMCAL. However, the calorimeter performance does not only depend on the physical properties but also on the hardware. In this case, the basic difference between the two calorimeters comes from the electronic noise.

For comparison between the ALICE calorimeters Equation 20 is plotted using values of FoCal, EMCAL, and PHOS presented in the table. At lower energies, the resolution is dominated by the stochastic and noise term. FoCal has the largest stochastic term and thus the largest resolution at lower energies out of the three detectors. However, at large energies, the resolution depends more on the constant term and the energy resolution of FoCal exceeds EMCALs resolution at ~ 250 GeV and PHOS resolution at ~ 3 TeV. Since FoCal is located at higher rapidity, where the particles will be more energetic for FoCal, the constant term is important to be kept small.

4.2 FoCal readout

FoCal uses programmable ASIC (Application-Specific Integrated Circuit) chips for the readout from the sensors. The chips are designed for the purpose of calorimetry in high-energy physics by CMS collaboration and are called HGCROCs [128]. One HGCROC is capable of reading 72 different channels and has in addition 4 channels for common mode noise subtraction and 2

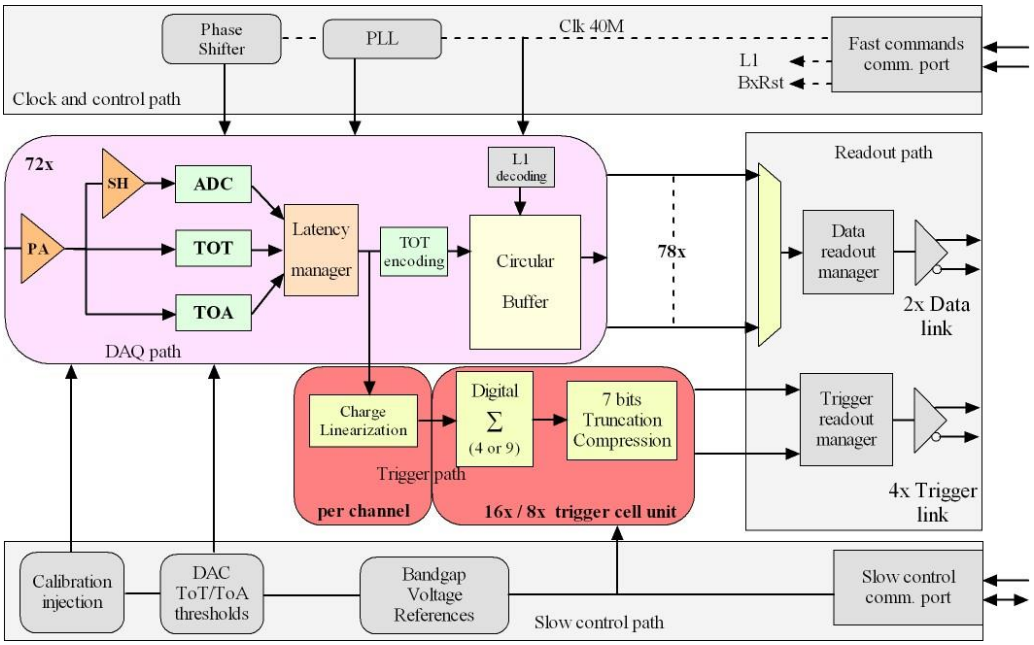

FIGURE 38 The architecture of the HGCROC chip. Figure taken from [128], ©2020 IEEE.

calibration channels. During the test beams the common mode channels were switched off and the common mode noise was calculated using the regular channels, as will be explained in the next section.

An overview of the HGCROC architecture can be seen in Figure 38. The charge input from the silicon sensor is first converted into an output voltage via the preamplifier (PA), following the shaper (SH) which then gives out the digitized ADC count. HGCROC provides a 10-bit ADC in the linear range of the preamplifier and when the ADC saturates, the signal can be measured with the Time-over-Threshold (ToT) method [129]. Timing information is provided by ToA (Time-of-Arrival) pulse.

Through the slow control, the chip can use internal injection which means that the channels are directly fed with a charge signal instead of measuring the charge from the chips. This can be used for calibration purposes and investigating the linearity between ADC and ToT. The adjusting of ToT and ToA thresholds is also done through the slow control port and determine how large a charge is needed so that the ToT measurement starts.

It is important to adjust the readout so that the gain received from the sensor is large enough that the MIP signal can be separated. A larger gain however narrows the dynamic range of the sensor which means that the gain needs to be adjusted so that the dynamic range covers even the largest possible signals from the energetic particles. The gain can be adjusted by changing the preamplifier parameters Cf and Cf_comp which are values given for parallel capacitors in the unit of fF. The capacitors provide the gain of the preamplifier, Cf_comp improving the stability. Another parameter to be adjusted is the value of the feedback resistors Rf. The time constant, product of $Cf \cdot Rf$ should be adjusted to get a clear MIP peak. These parameters can be adjusted only globally, the same values being applied to all channels of the HGCROG. [130]

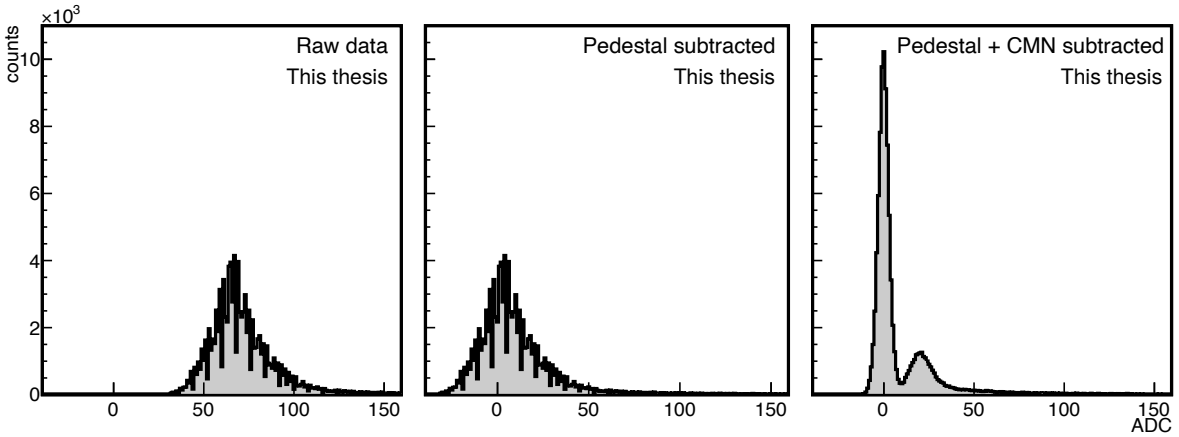

FIGURE 39 Analysis procedure for the test beam data. Pedestal subtraction shifts the ADC distribution around zero while only after subtracting the CMN from the data a clear MIP peak is revealed.

4.3 Analysis procedure

This section explains how the MIP signal was obtained from the digitized signals of the pad sensors. Then the discussion is extended to the full electromagnetic shower in the FoCal-E. The analysis steps include the noise removal and energy calibration, and then for the electrons the clusterization. The results are also compared to simulations and for that reason, the simulation software built for the test beams is presented in the end.

4.3.1 Pedestal and noise removal

Without a proper understanding of the background in the measurement, the physics signal cannot be distinguished from the noise coming from the electronics and environment. Even if the sensor is measuring seemingly nothing it will collect charge and this signal is called the pedestal signal. The pedestal level depends on the electronics and the sensor itself, which means that it needs to be determined for each channel individually. The pedestal is always presented and is gaussian distributed if no other sources than background sources are presented. The width of the distribution then is the level of noise the channel experiences.

The noise can be intrinsic i.e. coming from the electronics and its level stays similar while no changes happen to the setup. However, one needs to take into account also changes in the environment. For example, a change in the measurement cavern temperature can very well affect the noise level. These kinds of changes can affect all the channels (or sub-group of them) similarly and is thus called the common mode noise (CMN).

To obtain the signal from the traversing particles there are then two steps that need to be made: remove the pedestal to get the correct ADC value for the signal and remove the CMN event-by-event. The signal S_i (i referring to ith channel) after noise subtraction, can be then obtained via

$$S_i = ADC_i - P_i - CMN = ADC_i - P_i - \frac{\sum_k (ADC_i - P_i)}{N_k}, \tag{21}$$

where P_i is the pedestal value for channel i. The sum goes over k channels taken into the CMN calculation and N_k is the number of those channels. An example of the ADC distribution is shown in Figure 39 after each step. The data is from the 2022 June measurement with a hadron beam of 15 GeV.

Pedestal values P_i can be determined most easily from pedestal measurement with no beam on but since the pedestal is the most prominent feature in the data even when the sensors are collecting particle data it can be extracted from physics runs also. In this analysis, the pedestals are determined from Gaussian fit to the pedestal and then corrected with a second iteration to ensure that the pedestal peak is at zero after the pedestal subtraction.

To determine the CMN in an event the pedestal subtracted signal in each channel used for the calculation is sorted from smallest to largest. Then CMN is calculated from the mean value of the channel with signal strength at the middle of the list. This ensures that the mean will not be skewed because of non-functioning channels (no signal or oversaturation) or the physics signal.

4.3.2 Clusterization

To measure the energy of electron showers in the pad layers the channels containing a signal from the electron shower must be summed together i.e. clusterized. The simplest way to estimate the shower energy would be to sum over the channels close to where the particle beam goes through. To take into account the event-by-event differences between the showers an algorithm is needed to construct the shower. The following clusterization algorithm was used for the test beam data:

1. find out the seed i.e. the channel of largest signal strength
2. check the adjacent channels to the seed: if the channel signal exceeds a set threshold (to exclude noise) the channel is added to the cluster and tagged as checked
3. go through the adjacent, non-tagged channels of channels included in the cluster until there are no adjacent channels which are above the threshold any more

Each triggered event should contain one electron shower and therefore it is sufficient to assume that the shower core is the channel with the largest signal.

The clusterization is done after both the pedestal and CMN subtractions. To have the results in units of energy the MIP results are used in the energy calibration. The ADC signal S_i in channel i is calibrated to a value of energy E_i via

$$E_i = C_i S_i = \frac{E_{\mathrm{MIP}}}{M_i} S_i, \tag{22}$$

where the calibration coefficient C_i is calculated using the simulated values of MIP peak position $E_{\mathrm{MIP}} = 80$ keV and the MIP peak position M_i from Landau fit of the measured distribution. In the analysis, the calibration is done after the subtractions.

4.3.3 Simulation

Simulation software was prepared for the setups used in the measurements. The simulation was built using Geant4 [116], a C++ -based simulation toolkit widely used not only in high-energy physics but also for example in medical physics. Geant4 has extensive geometry classes to

create the desired geometry for the detector, implementation of different physics depending on the studied subject and saving the output to the desired format such as ROOT files.

The simulation includes FoCal-E and the spaghetti version for FoCal-H. The code is written in such a way that many parameters, for example, the number of FoCal-E layers and FoCal-H modules can be adjusted easily. The test setups were not the same in all the test beams but were slightly modified, in the 2021 SPS test beam only one pad layer was included and FoCal-H has had one module, testing with nine in the 2022 September test beam. The simulation results presented in this thesis are produced with configurations including only FoCal-E.

To have meaningful results from the build detector geometry the user has to specify particles, physics processes and production cuts using the classes found in the framework. However, Geant4 provides validated physics lists that include the relevant physics for different purposes. For high-energy physics, the lists FTFP_BERT and QGSP_BERT are recommended to be used since they have been tuned using LHC data for shower longitudinal and lateral shapes [131]. The difference between them comes mainly in the handling of inelastic collisions of hadrons at higher energies: FTFP_BERT uses the Fritiof parton model whereas QGSP_BERT switches to quark-gluon model (QGS) for most hadron species above 12 GeV. For our simulations, FTFP_BERT was chosen since it is the default reference physics list.

The Geant4 simulation does not take into account the individual differences between the channels nor the pedestal and noise. These are added to the simulated data in the analysis phase by randomly generating a pedestal value from a gaussian distribution and adding it to the simulated ADC value. The gaussian function parameters are determined from the data for each channel. After the addition of the noise the ADC value is converted back to energy using the MIP calibration and the clusterization is performed similarly to the measured data.

4.4 Results

FoCal had an extensive testing period during 2021 and 2022, including four test beams over 1.5 years. These test beams were held at CERN facilities and utilized particle beams provided by the Proton Synchrotron (PS) and the Super Proton Synchrotron (SPS). The testing sites are marked in Figure 40 which shows the locations of the CERN experiments and facilities in relation to the accelerators. The SPS testing line is located in the North Area whereas the PS beam lines go in the East Area. PS can provide electron, positron and hadron beams up to 26 GeV [132] while at SPS the energies can reach as high as 450 GeV [133]. The first one was held at SPS in September 2021 in which all the FoCal sub-systems were present but measuring independently. In June 2022 the test beam, held at PS, mainly focused on testing the parameters of the pad sensors while the FoCal-H prototype was also present. In the next test beam in September 2022, held first in SPS and then continued at PS, all the sub-systems utilized the same triggering system which then enabled the tests for combined events in FoCal. The last test beam in November 2022 at SPS to extend the program to higher energies, up to 300 GeV.

As mentioned before, this analysis focuses on data collected in the first two test beams and addresses only the measurements done with the pad sensors.

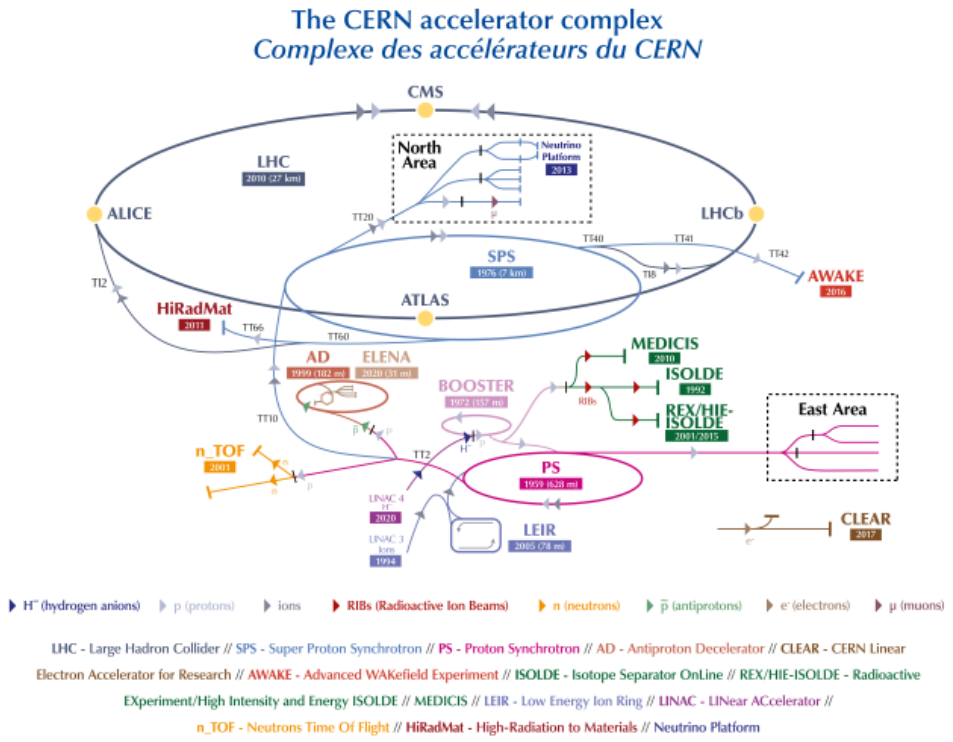

FIGURE 40 Map of CERN facilities and experiments alongside the accelerators as in 2022. Points of interest from the standpoint of this thesis are the ALICE detector site at LHC, and beam testing sites in North and East Areas. Image by CERN.

4.4.1 2021 SPS test beam

During the fall of 2021, the test beam for FoCal was held at SPS. Both the FoCal-E and FoCal-H were present in the test, with the FoCal-E setup including one pad sensor and two pixel sensors. FoCal-H prototype was a 10 cm $\times$ 10 cm $\times$ 100 cm copper box filled with copper tubes that contained the scintillator fibres. Also, alongside FoCal testing EPICAL-2 [134], a calorimeter prototype composed of 24 layers of 3×3 cm^2 similar pixel sensors as used in the design of FoCal, accompanied by tungsten absorbers.

The plan for the pads was first to measure MIPs for calibration purposes and then particle showers induced by tungsten layers. It was however discovered that the pad could not be placed between the tungsten plates due to electrical interference from the common SPS ground. This affected the readout so that no meaningful data would have been collected with the intended setup. The grounding issue was avoided by placing the pad behind the tungsten layers (with a 11.3 cm gap between the last tungsten layer and the pad), far enough from the ground. The two pixel layers were placed behind the pad sensor. The setup can be seen in Figure 41.

The MIP data for all 72 pad channels tested in the fall can be seen in Figure 42. All except channel 65 (marked with a red cross) were working during the running and were able to collect data. In this case, the common noise was calculated separately for two sides of the sensor (channels 0-35 and 36-71) since the two sides operate independently from the readout standpoint. In the calculation, only three channels with signal strength from the middle of all signals between minimum and maximum signals are used. This ensures that the average represents the common

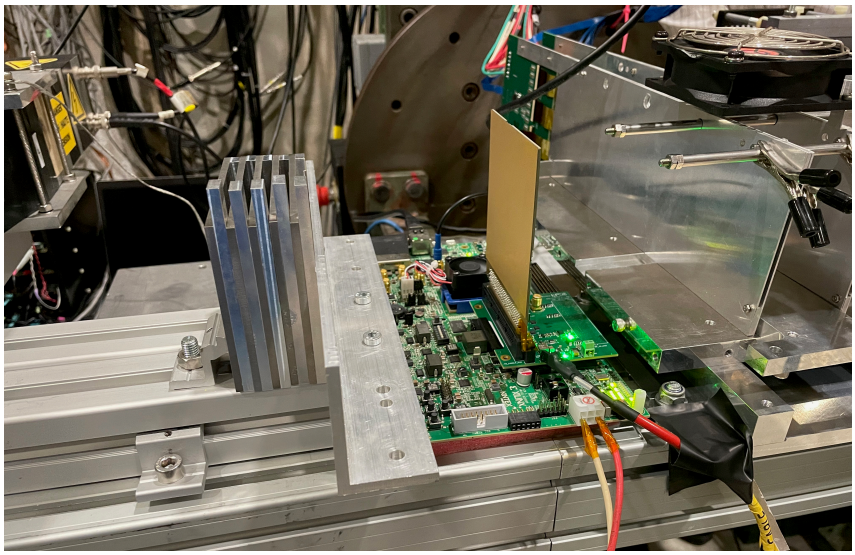

FIGURE 41 The setup during the SPS test beam in 2021. The pad layer can be seen in the middle after the tungsten plates, two pixel layers then behind the pad.

noise best way possible, leaving out possible saturated and zero signal channels as well as the channel with real particle signal.

Considering all of the channels, the MIP signal can be seen in most of the channels clearly next to the noise pedestal (around 0 ADC), at 12 ADC counts. However, the separation between the pedestal and the MIP peak is not as clear as expected. This might have been due to incorrect tuning of the readout board parameters which could have resulted in a non-ideal gain. Since the MIP peak was not clear after the noise subtractions an isolation cut was applied to the data to distinguish the MIPs better. The isolation criterion excluded events that did not have a clear MIP signal: only events in which one of the channels has a signal of ADC > 5 and others ADC < 5 were used. Using 5 ADC counts as the isolation cut value is not large enough to leave out too much of the true MIPs around 12 ADC but cuts efficiently false events with only noise. The result after the noise subtraction and isolation cut can be seen in Figure 43 for one of the two calibration channels (CALIB1) found from the sensor.

During the test, the channels were not scanned one by one but the beam spot stayed mainly around the lower right corner of the sensor. Therefore for example the channels on the left side did not pick up many MIPs and thus the MIP signal is weaker in them. Although the difficulties the MIP signal was present and it could be fitted with landau distribution to determine the position of the peak and its width. The parameters from the fits for all the channels are collected in Figure 43. Here it can be seen that the MIP peak can be found at a slightly larger ADC value on the upper half of the sensor compared to the other half. This can be explained by the different settings in the readout board which lead to different gains for the halves.

In the 2021 test beam, the showers were measured with two different setups, with 5 and 10 tungsten layers in front of the sensor. This produces different showers and models the sensor response at two different depths in the final 20 layer design. The aim was to see the distribution of clusters at different energies which is crucial to determine the energy resolution for FoCal.

The results from the tungsten runs are shown for 5 and 10 tungsten layer setups in Figure 44 and Figure 45 respectively. The figures present the cluster energy distribution at different beam energies. The energy left by the shower to the sensor is clusterized by starting from the channels

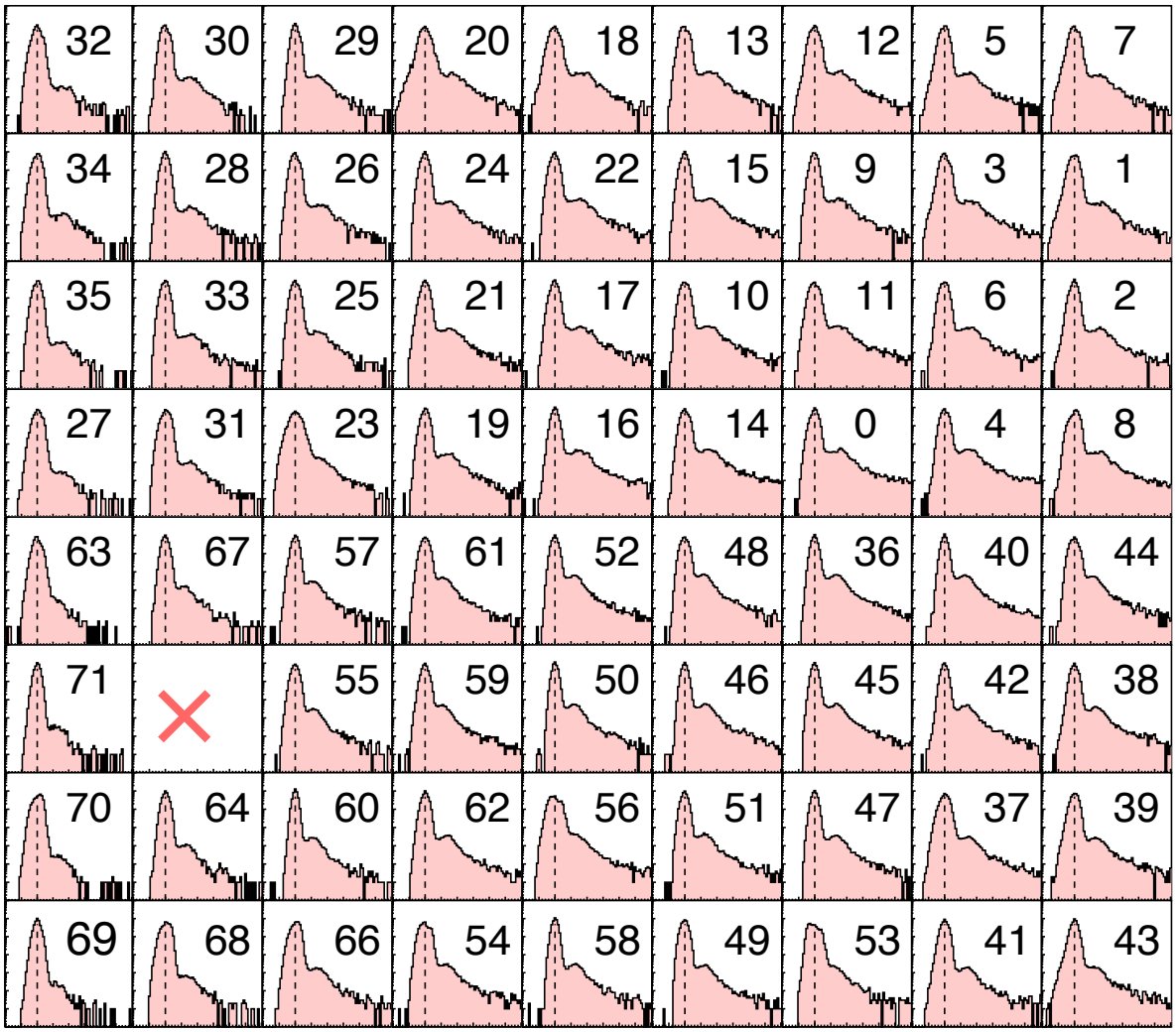

FIGURE 42 ADC distributions after pedestal and common noise subtractions, with isolation cut applied. For each channel, the channel number is presented in the corresponding panel. Channel 65 was not working and is thus marked with a red cross.

with the largest signal (seed) and then adding the adjoining channels if they exceed a certain threshold. The ADC counts in the channels are converted to energy values utilizing the MIP data and simulations. Data was collected with beam energies of 20 GeV, 40 GeV, 60 GeV, and 80 GeV. In addition to these energies, 120 GeV beam was used for the 10 tungsten setup to test the ToT of the HGCROC.

The data is consistent in the sense that the clusters have larger energies when the beam energy increases. The beam used in the measurements was a mixture of electrons and hadrons. Hadrons dominate the spectrum at the lower cluster energies since most of them won't leave a shower but go straight through the electromagnetic calorimeter. If the beam purity for electrons is high enough a clear electron peak is seen in the cluster energy distribution. However, the purity decreases greatly when the beam energy increases and that can be seen in the data since it is difficult to distinguish the electrons from the hadrons.

The data is also compared to the Geant4 simulation. The simulations take into account the noise pedestals for each channel. This is done by using the Gaussian distributions extracted from the measured MIP distributions and randomly sampling them to induce extra noise for

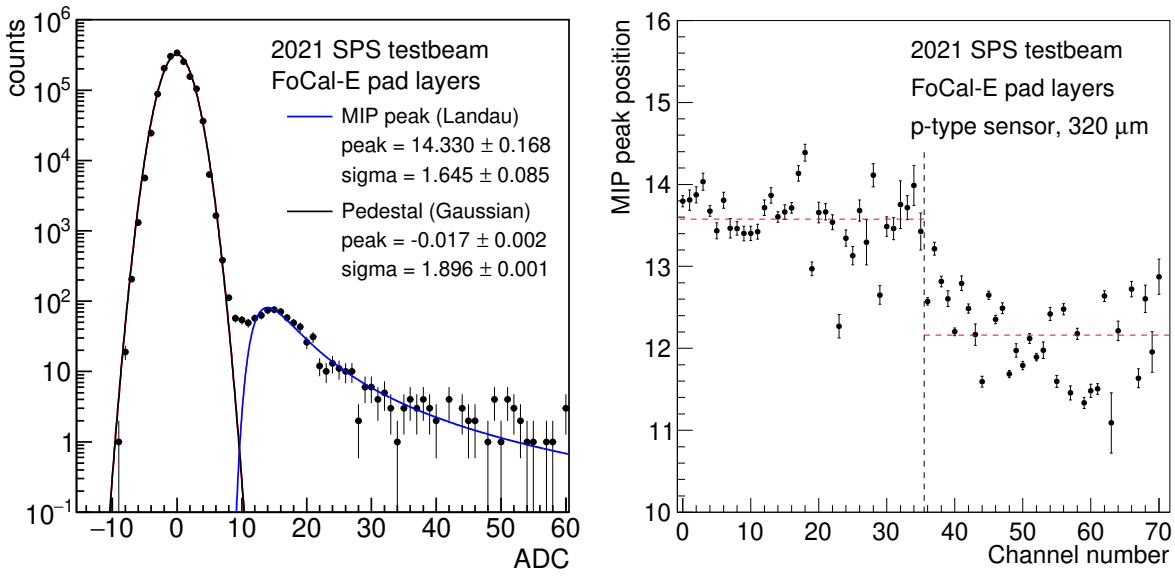

FIGURE 43 Results from the MIP analysis, ADC distribution from CALIB1 (left) and the MIP peak position values from the Landau fit in each channel (right).

the channels. The beam purity is also taken into account; both hadrons and electrons were simulated and their ratios were fixed according to the measurements of EPICAL in the test beam. The ratios estimated from the EPICAL data are presented in Table 2. The simulations yield similar distributions at lower energies but at larger energies, they start to deviate from the measurements. This could be due to the switch from ADC to ToT not working properly which then affects the clusters with higher energies.

TABLE 2 Electron beam purities at different energies in SPS FoCal test beam, estimated by EPICAL.

Beam energy	20 GeV	40 GeV	60 GeV	80 GeV
Electron purity	35.5%	22.0%	15.6%	1.9%

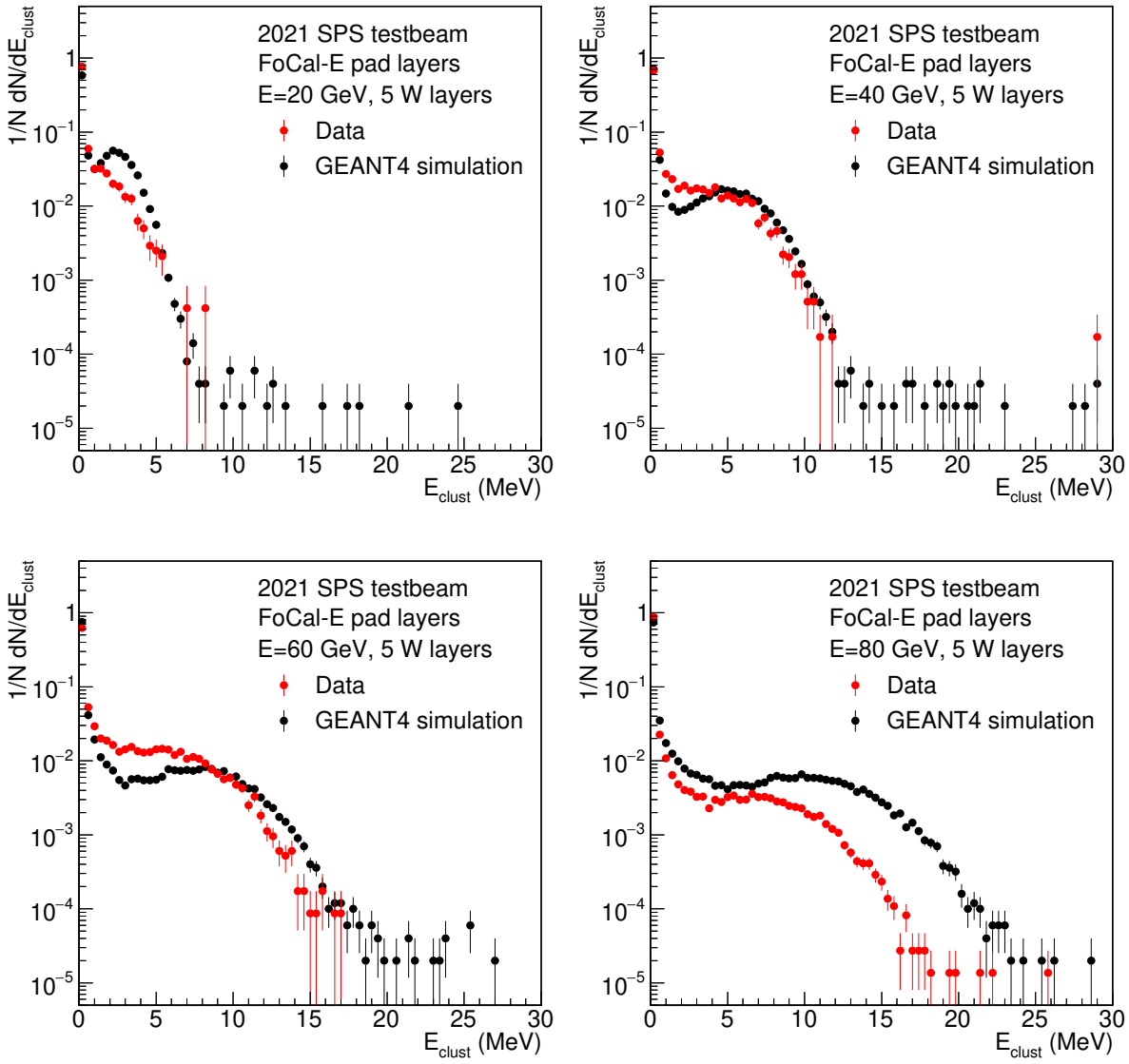

FIGURE 44 Electron shower results for the pad layer from 2021 test. The showers were created by placing five tungsten layers in front of the sensor.

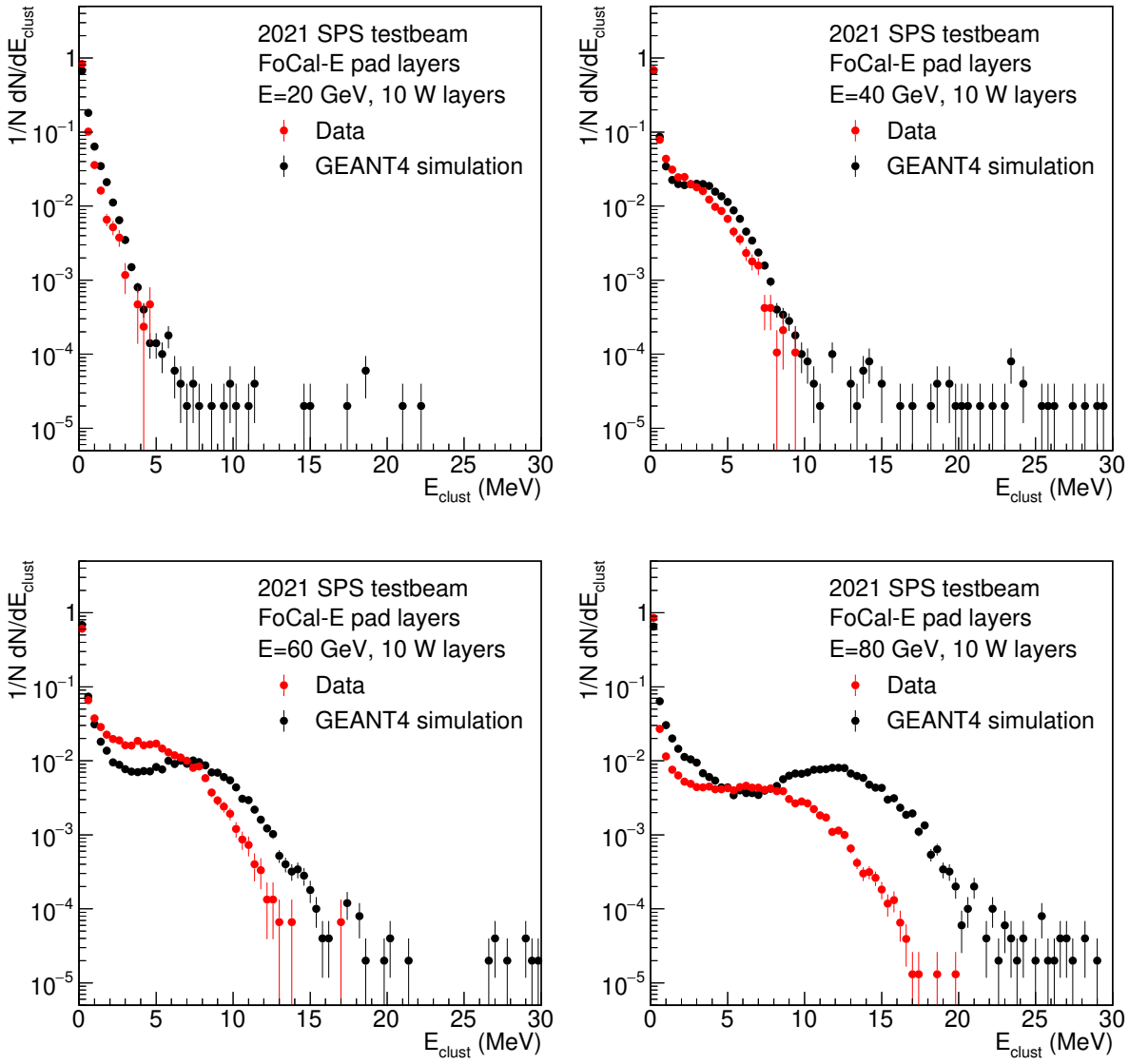

FIGURE 45 Electron shower results for the pad layer from 2021 test. The showers were created by placing ten tungsten layers in front of the sensor.

4.4.2 2022 PS test beam

The test beam held in June 2022 was mainly focusing on investigating the different settings on the HGCROC chip. FoCal-E test setup held 20 tungsten layers complemented with the 18 pad layers, leaving empty places for pixels at their respective layers. In addition, two prototypes of FoCal-H with different lengths were present at the test beam, measuring behind FoCal-E. FoCal-E prototype and the shorter FoCal-H prototype can be seen in Figure 46, mounted to the table with scintillators in front for triggering.

Both hadrons and electrons were measured during the test beam. Figure 47 shows examples of both hadron- and electron-like events in all layers after the analysis steps introduced in Section 4.3. The path left by hadron traversing the layers (Figure 47a) can be clearly seen. Similarly, the showering behaviour of electron is visible in Figures 47b and 47c. Misbehavior can be seen in some of the layers, for example during this hadron run the 15th layer did not work as intended and the same applies for the 16th layer in the case of 5 GeV electron run. Incorrectly working layers were present during most of the runs and the misbehavior was related to complications when the data acquisition was initialized. The number of misbehaving layers and which layers were affected was mostly random, though some layers were more likely to not collect good data after the initialization. Since from time to time the DAQ program needed to be restarted the data quality was checked for each run layer by layer and if any misbehavior was observed the layer was left out from the analysis. The misbehavior appeared as, for example, a chunk of data missing or shifted in the ADC distribution. Also, in some cases, the problem affected only the other half of the sensor.

At the beginning of the test beam, a large amount of time was dedicated to testing the different HGCROC readout circuit settings. Tested HGCROC settings include voltage scan, finding the correct delay time for the signal, and pre-amplifier settings for the optimal gain. These settings affect the MIP and noise response of the sensors and optimal values would reflect a situation where the separation between the pedestal and the MIP peak would be the largest.

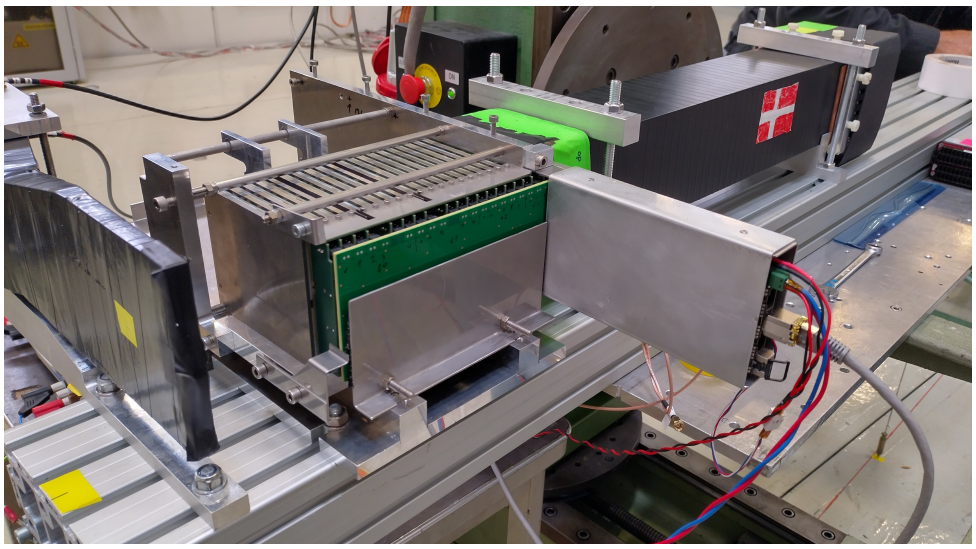

FIGURE 46 The setup of 18 pad layers in the 2022 PS test beam, accompanied by FoCal-H prototype behind it.

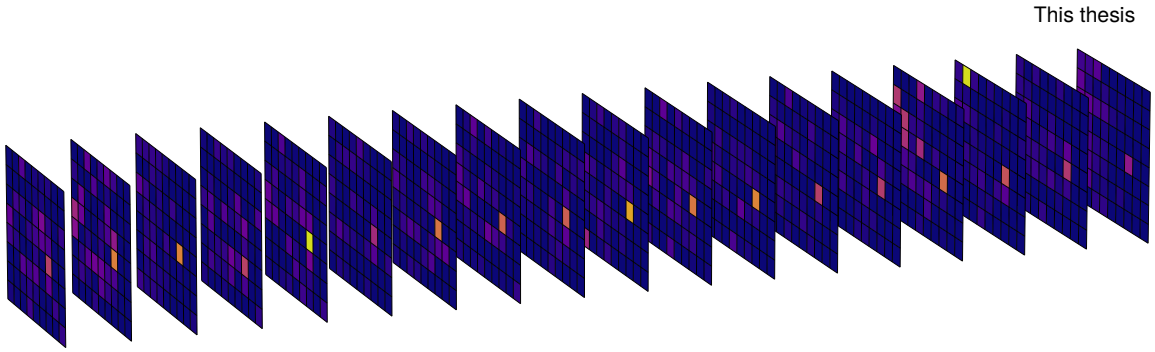

(a) Hadron beam

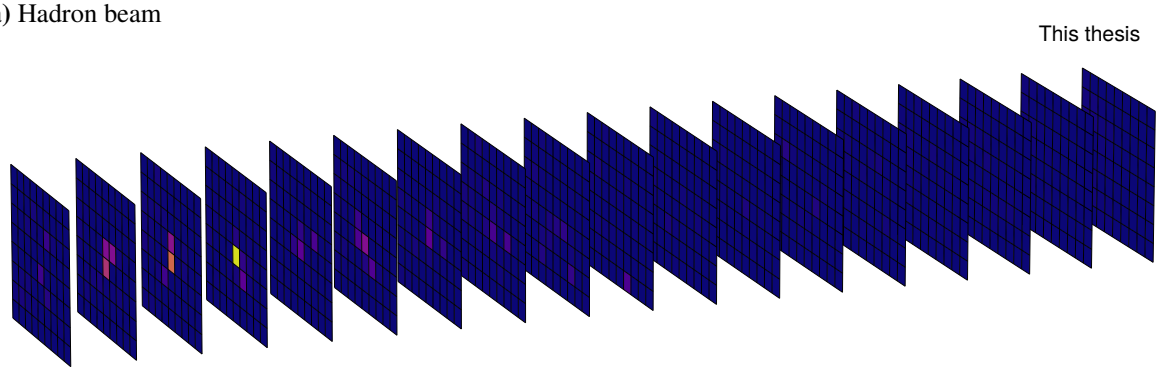

(b) Electron beam of 2 GeV

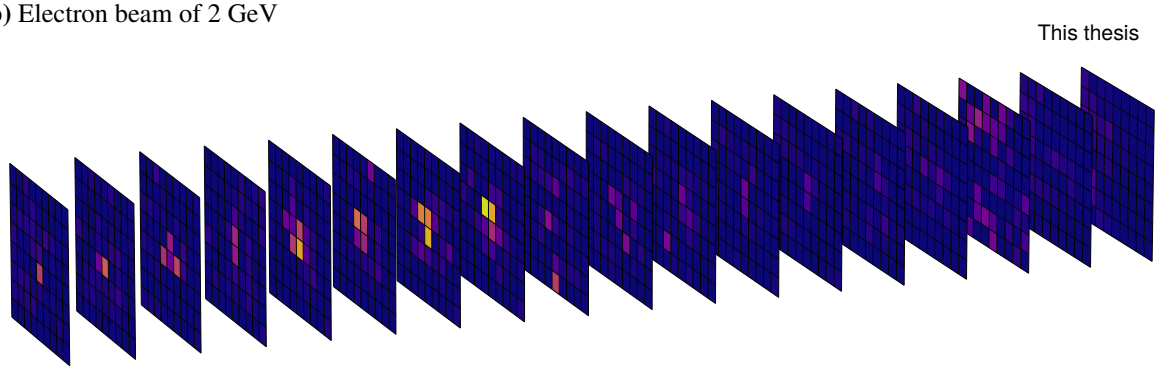

(c) Electron beam of 5 GeV

FIGURE 47 Example of one particle event in three different beam configurations.

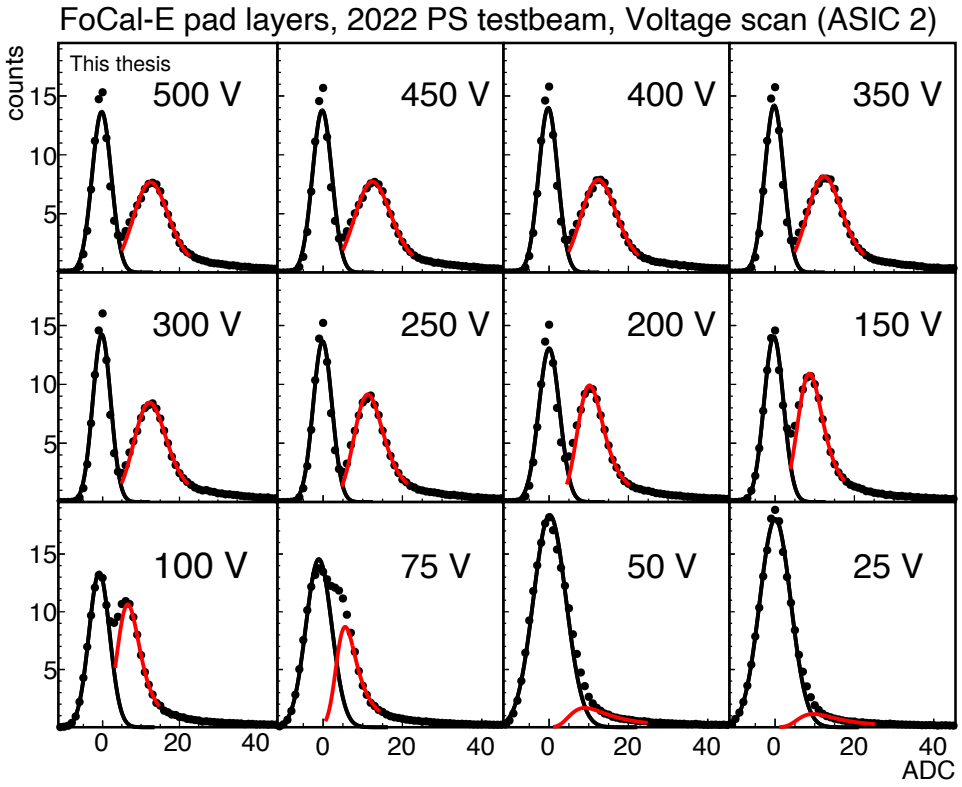

FIGURE 48 ADC distribution with varying voltage in the second layer.

After the signal timing was determined so that a clear MIP signal was observed the bias voltage of the detector was then investigated. The voltage was varied and the MIP response was checked with each voltage value used. The correct operating voltage increases the Signal-to-Noise ratio and it is thus important to investigate at what point the signal suffera from overly small bias voltage. The fitted ADC distributions after pedestal and common noise subtractions can be seen in Figure 48. The figure shows the distributions with varying bias voltage values for the third layer (labelled 'ASIC 2'). The results for other layers can be found in Appendix A. Differently from the 2021 analysis, the MIP peak was fitted with a convolution of Landau and Gaussian function (Langaus) [135] instead of the Landau function. It was noticed that the convoluted function represents the data better than regular Landau.

MIP peak positions and pedestal widths from the fits are compiled for all available layers in the left plot of Figure 49. Excluding a couple of outliers, the MIP peak position is quite similar for several layers ($10-12$ ADC counts). The peak position stays relatively constant until $V =$ 300 V and starts to move to smaller ADC values at lower voltage values. At $V = 75$ V the MIP peak starts to merge with the pedestal which can be seen as an increase in the pedestal width. For this reason, the fit function cannot be fitted to the data and the MIP peak position is left out for the low voltage values. On the right side of the figure, the width of the gaussian part of the Langaus fit function is shown. There is approximately one ADC count worth of variation across the different layers (again excluding a couple of odd ones) but the width stays quite constant value of 3-4 ADC counts after $V = 300$ V.

As described in Section 4.2 the gain of the sensors can be adjusted by changing the pre-amplifier parameters Cf and Cf_comp, and the value of the resistors Rf. To find the best combination several measurements were performed with varying these values. The results are combined to Figure 50 for three different layers (ASIC 2, ASIC 5 and ASIC 16). Only these layers are

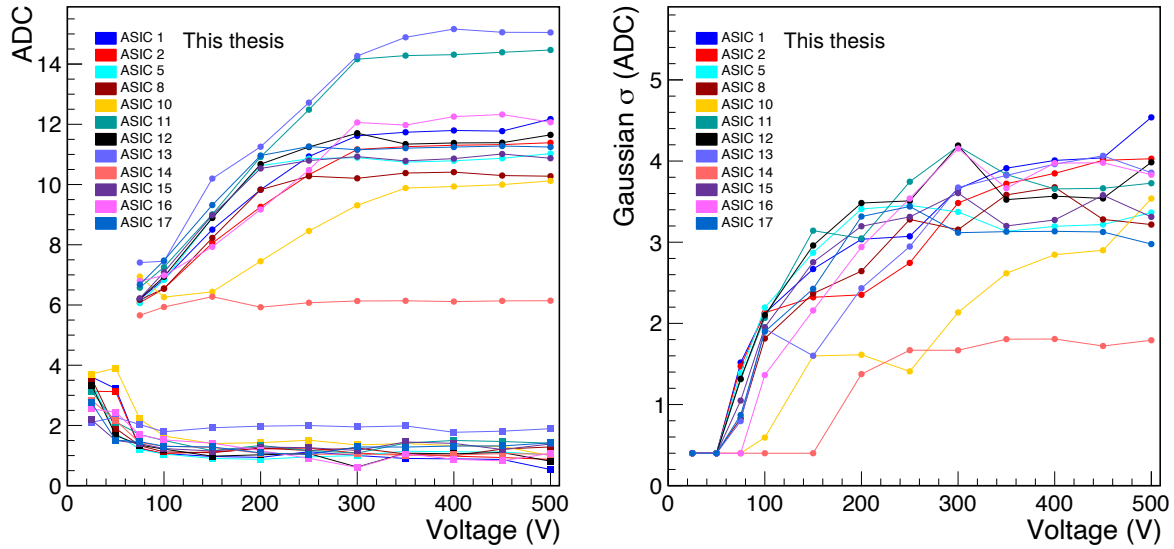

FIGURE 49 The MIP peak positions and the pedestal widths (curves around 1-2 ADC counts) from the voltage scan for the layers with good data (left figure). The width of the gaussian component from the Langaus fit is shown on the right side.

shown since they were functional during each scan with different parameters and thus in their case, the comparison between all setting combinations can be made. As can be seen, many of the combinations are not good enough to separate the signal from the noise. Also, the pedestal width varies between the settings. It was found that with values $Cf = 200$ fF, $Cf\_comp = 100$ fF and $Rf = 50$ kΩ best separation was achieved. The MIP peak position was approximately doubled compared to the previous settings which placed the MIP peak position at ~ 12 ADC counts.

After tuning the pre-amplifier settings the MIP response of each individual channel was studied by moving the detector table so that the 15 GeV proton beam would hit different cell centers. This position scan was repeated for each cell, therefore resulting in 72 runs in total. The ADC distributions for each channel in every pad layer after the pedestal and CMN subtractions can be seen in Appendix B. As mentioned before the problems in the DAQ program initialization caused poor-quality data in some layers. The channels for which the MIP peak fit could not be performed due to the misbehaviour are marked with red color. Most of the channels show excellent separation between the pedestal and the MIP peak, around 15% of the channels are affected by the DAQ misbehaviour. The most problematic layers are ASIC 3 and ASIC 9, as well as the other half of ASIC 14.

The results of the position scan MIP peak fits are collected in Figure 51. The upper panel shows the MIP peak position for each channel in each of the layers while the MIP peak width is shown in the lower panel. Channels with poor quality data, in other words, channels from which the MIP position cannot be extracted have been left out of the figure. Figure 51 shows that the variation in peak position between the channels is quite large, the peak position can vary from 10 to 30 ADC counts. A clear difference in the mean values of MIP peaks calculated in the two halves of the ASIC tested in the 2021 test beam was observed but here the behaviour does not have a correlation on which side is in question. The mean values calculated over all of the channels in one ASIC have similar values to each other, around 20 ADC counts. However, a small difference between the layers can be seen in the MIP peak width. The average width in the first 3 to 4 layers is smaller compared to the later layers for which the width is more consistent.

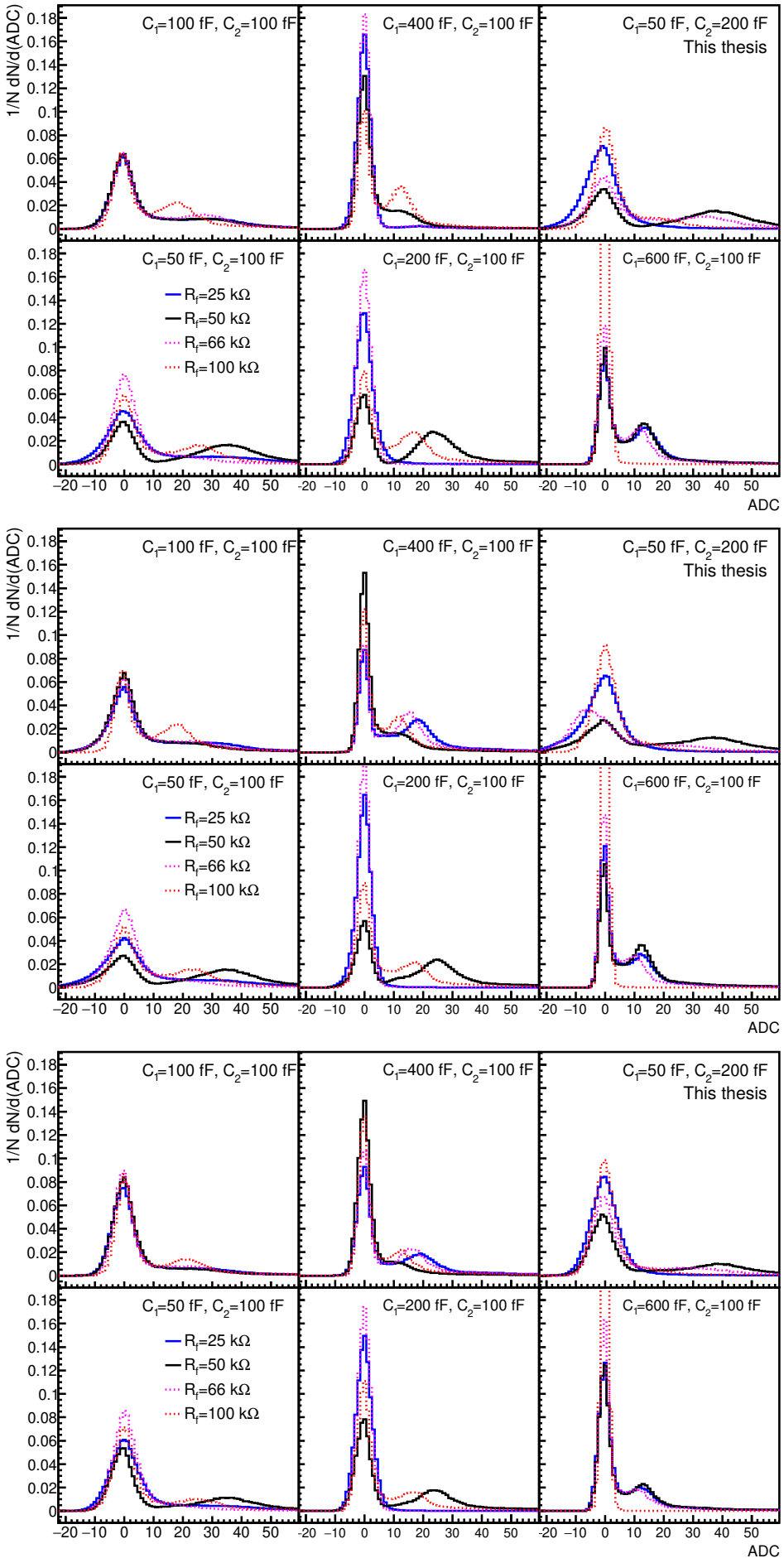

FIGURE 50 The ADC distributions with several HGCROC gain settings for, from up to down ASIC 2, ASIC 5, and ASIC 16. The distribution with the settings chosen for the rest of the testing is shown in the middle lower panel (black curve).

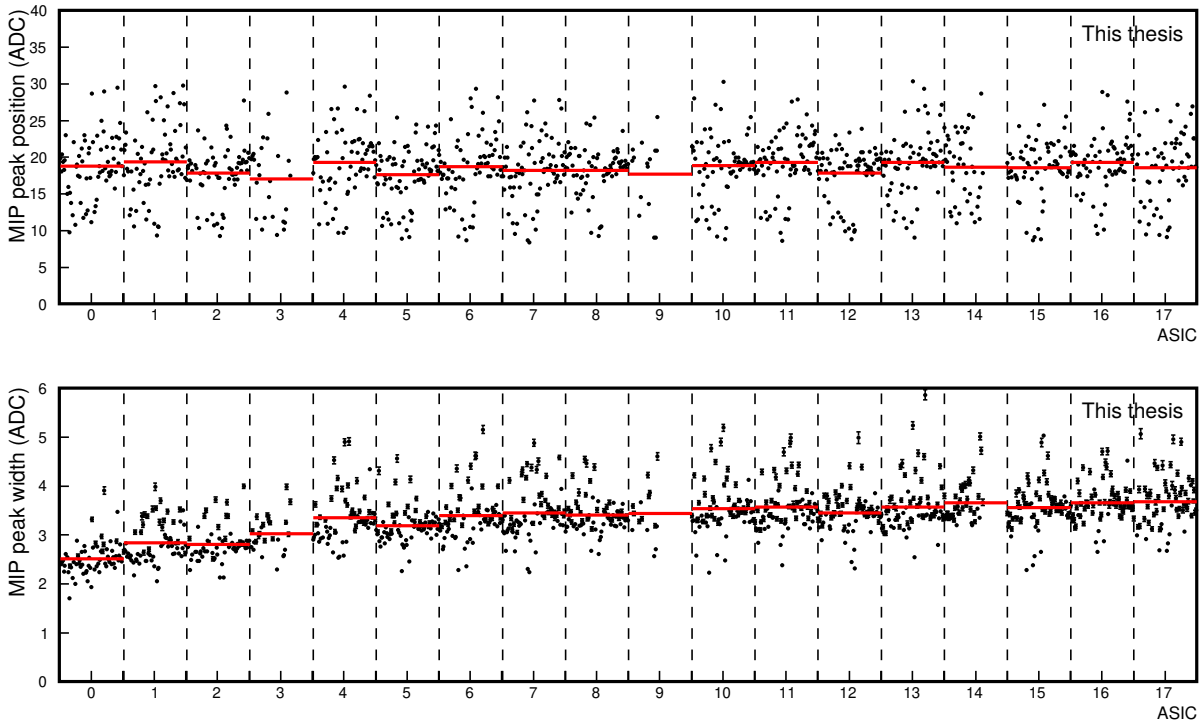

FIGURE 51 Overview of the MIP peak positions (upper panel) and widths (lower panel) in all 18 pad layers. The mean value in each layer is marked with the a red line.

Here only the width of the Landau component of the convoluted fit function is plotted but the gaussian component contributes to the width of the peak also. As explained in Section 4.1.1 there are underlying events that come from the multiple MIP hits that contribute to the tail in the distribution. In a way, the Gaussian component may compensate for the sum of the multiple MIP distributions and therefore result in a better fit.

After the position scan the beam was switched from pions to electrons. This allowed us to investigate the shower profile at different energies. The energies used in the 2022 test beam were lower and more pure than in the SPS test beam, data was collected using energies from 1 GeV to 5 GeV. The MIP peak positions from the position scan are used in the calibration of the cluster energies in the electron runs, according to Equation (22). Due to the fact that the peak position could not be extracted for all of the channels, a value of 20 ADC counts is used in the calibration for the channels with missing peaks. Then from the calibrated signals clusters were constructed in each layer separately. The pedestal width in each channel was used as the threshold to determine if the channel should be included in the cluster.

Figure 52 shows the cluster energies for 5 GeV electrons in each layer for two different data sets. To block any light from the environment the pad setup was closed inside a box for several runs. This was done to see if the light would affect the border channels in the sensors. Again data is not available for all layers and that is why data is missing for some layers. Both data sets (with and without the box) differ from the simulated distribution, especially in the middle layers the peak value is smaller compared to the simulation. In addition, a long tail can be seen in the middle layers for both cases. This may be due to calibration issue. After the position scan finetuning was done which changed the response of the channels. Also, some saturation was observed at higher energies ($4-5$ GeV) which may have pushed the distribution to lower values.

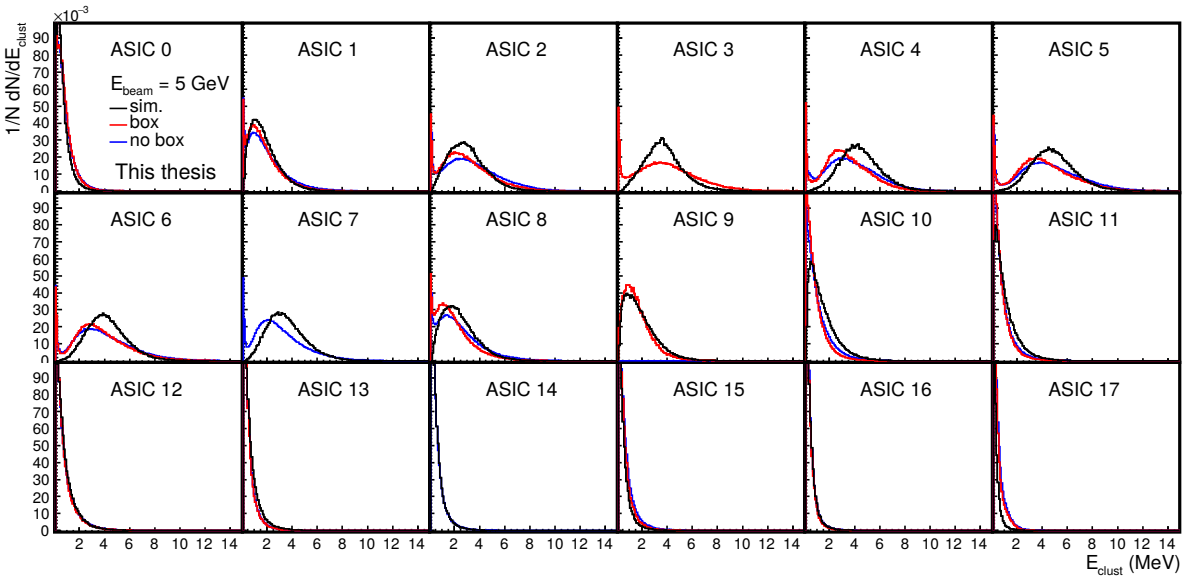

FIGURE 52 Cluster energy distribution for electron energy of $E = 5$ GeV in all layers.

The distributions with lower electron energies can be found in Appendix C. At lower energies, the differences in measurements with and without the box are more apparent. However, it could not be concluded with certainty that the differences were caused by the light. The increase in temperature inside the box also affects the measurements and it was hard to distinguish the effects of light and temperature. The temperature dependency of the sensors should be investigated in a more controlled environment than this test beam offered.

To determine the energy resolution for the pad layers the cluster energies from each layer need to be summed together. The Gaussian distribution width divided by its mean value would then give us the resolution. The summed cluster energy distributions are shown in Figure 53 for each energy. Due to the problems with the layers, the sums were calculated also from the middle layers only (ASIC 2, 4, 5, 6, and 8). These layers were selected because they were reliable during the measurement. Again the data with and without the box is plotted against the simulated distribution. From this figure, it can be seen that the electron peak is cleaner when the box is used, although the same characteristics which were present in the layer-by-layer distributions (long tail, smaller peak value compared to simulation) can also be seen here. These can also be seen in the middle layers which contribute to the energy distributions most since the shower maximum is located there.

Due to the shape of the distribution of the energy resolution, it is difficult to determine the resolution from a Gaussian fit. Therefore the standard deviation is calculated straight from the histogram, as well as the mean value. The peak at the low energy is left out of the calculation. Since the peaks are cleaner with the box the resolution is estimated only in that case. The result with fits can be seen in Figure 54. As mentioned before larger sampling rate i.e. more layers should in principle yield a better resolution. This can be seen here though it should be kept in mind that the resolution is degraded by the missing layers. Also, only low energies are included here and to get the full picture of the resolution data points at larger energies are needed to better estimate the constant term. In conclusion, these results give the first impression of the energy resolution at lower energies. However, it was the first time testing with the 18 layer setup and the energy resolution is expected to improve in the following test beams, where the problems with the readout have been fixed.

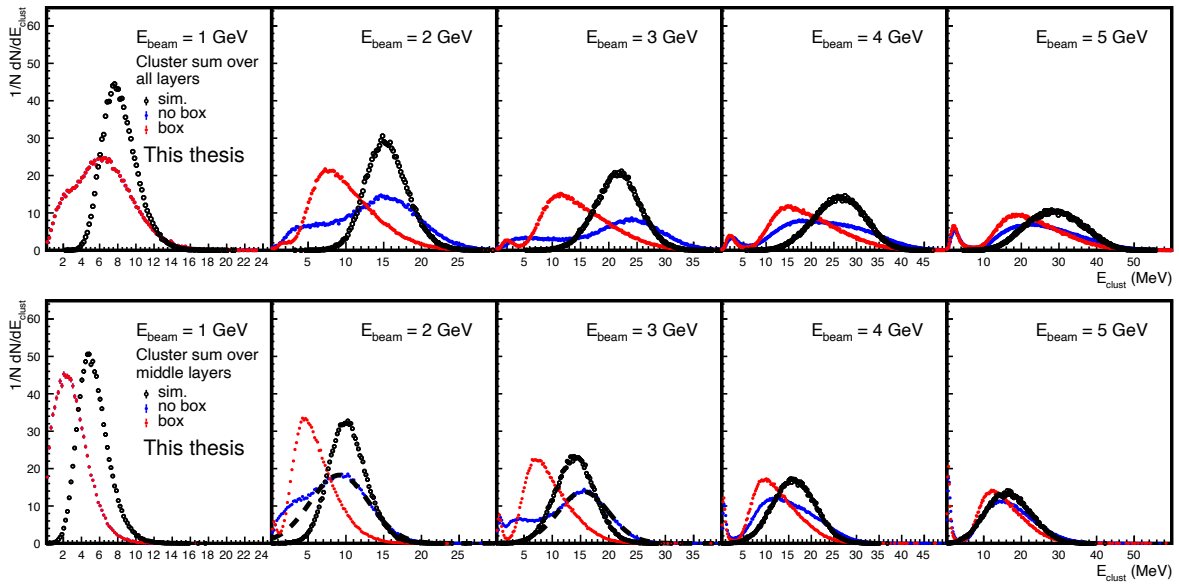

FIGURE 53 Summed cluster energies for all measured electron energies ($1-5$ GeV). The top row shows the sum over all working layers whereas only the middle layers are included in the bottom row.

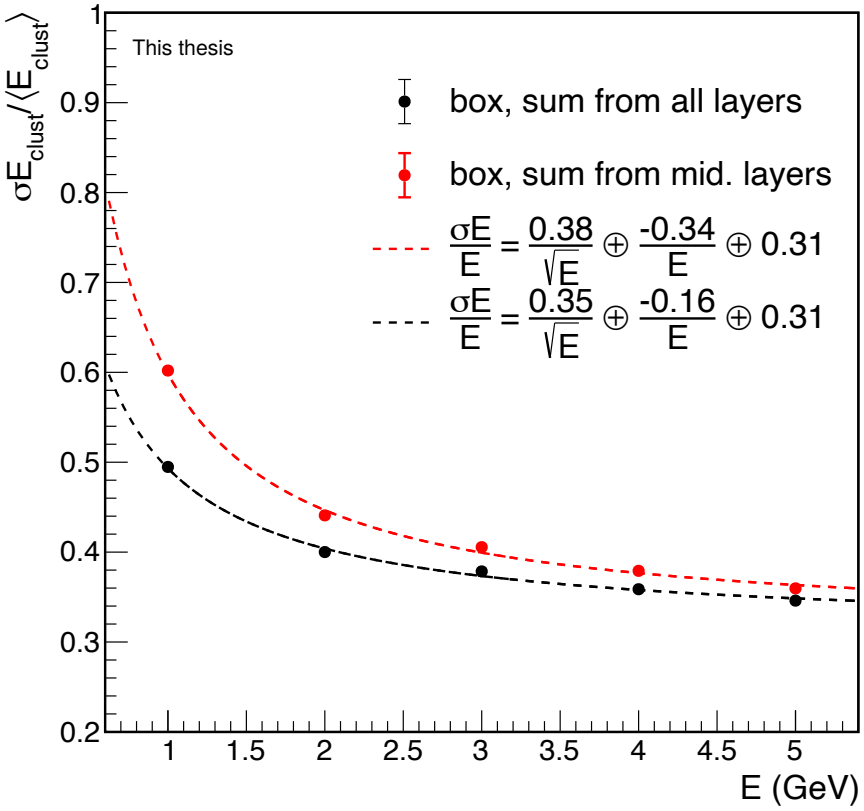

FIGURE 54 Energy resolution estimated from the summed cluster energies over all layers and over the middle layers.

5 FOCAL PERFORMANCE IN π^0–π^0 CORRELATIONS

In this section, the performance of FoCal is studied for π^0–π^0 correlations in which both the trigger and associated particle are measured in FoCal. As described in Section 2.3.1 two-particle correlations are attractive observables to probe the saturation region. Angular correlations measured in forward rapidity between trigger particle with $p_{\mathrm{T,t}}$ and associated particle $p_{\mathrm{T,a}} < p_{\mathrm{T,t}}$ are sensitive to low x region. According to CGC predictions, the gluon saturation is seen as suppression on the away side at lower p_{T} and in larger collision systems than proton-proton.

The sensitivity of π^0–π^0 correlations to x is demonstrated in Figures 55 and 56 with PYTHIA8 event generator [136]. PYTHIA is a widely used general-purpose Monte Carlo generator in physics analyses for high-energy collisions between elementary particles such as protons and electrons. The program is based on theory and models of HEP research and describes well proton-proton data which provides a well established basis for the studies presented here. The PYTHIA event record gives access to the momentum fractions x_1 and x_2 of the incoming partons in the initial hard process which then allows us to link the final state observable to the initial state. This is done in Figure 55 in which x_1 and x_2 of the event are saved when a trigger and associated π^0 in given transverse momentum bins are found in FoCal acceptance. The x_1 values of q_1, the parton moving towards FoCal, are mostly large since q_1 has to have a large momentum compared to the parton going in the other direction (q_2), to give a large enough kick to push q_2 towards FoCal. The moemntum fractions x_2 can reach values as low as 10^{-6} but peak around $10^{-5} - 10^{-4}$ at the lower trigger and associated particle p_{T}. The difference in p_{T} selection can be seen clearly in the projections in Figure 56: larger the trigger particle p_{T} is the more separated the x_1 and x_2 distributions are.

The goal is to measure the correlation between the true π^0 by removing the correlations of decay photons from different π^0 and other sources which contribute as correlated background in the measurement. In this work, I have developed a background subtraction method utilizing the reconstructed π^0 from so-called sidebands, outside the mass peak to estimate the background in the measurement. The sideband method has been used in previous correlation studies with reconstructed candidates such as in D meson-hadron correlations [137] but not in cases where both correlated particles are reconstructed in the same acceptance. Here the method is explained in detail and validated in pp collisions using a Monte Carlo generator. After that the method is applied to detector level simulation including FoCal, to obtain more realistic knowledge of how

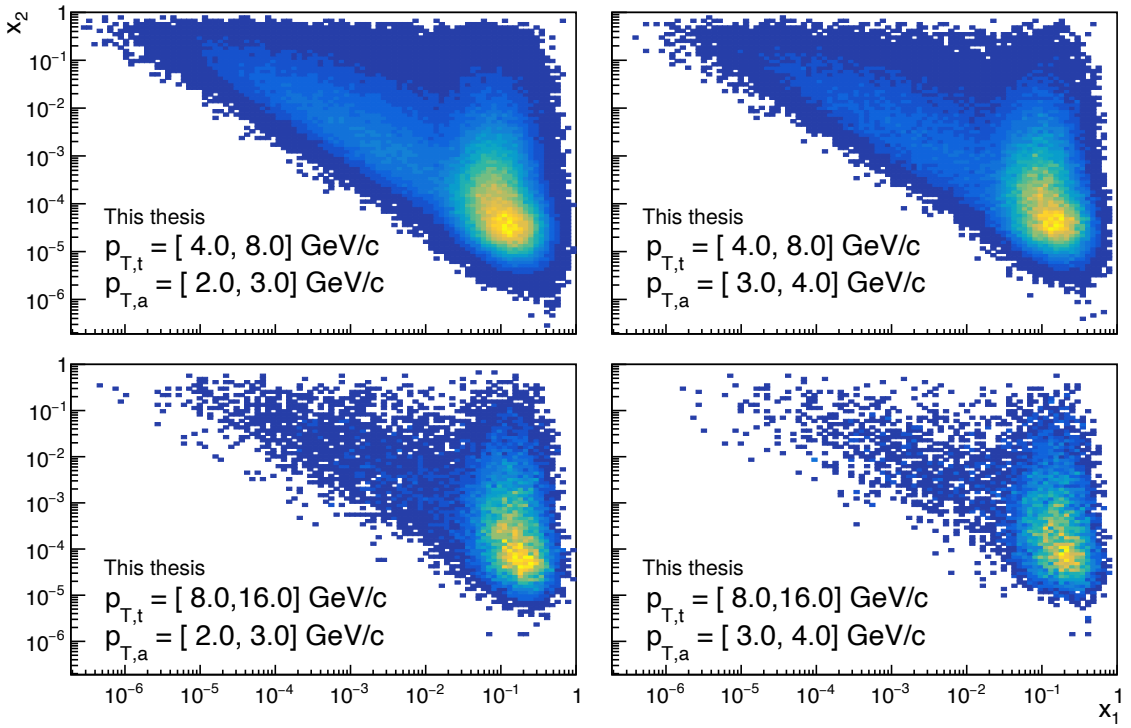

FIGURE 55 x_1 and x_2 values π^0–π^0 correlations probe in certain trigger and associated particle p_{T} bins.

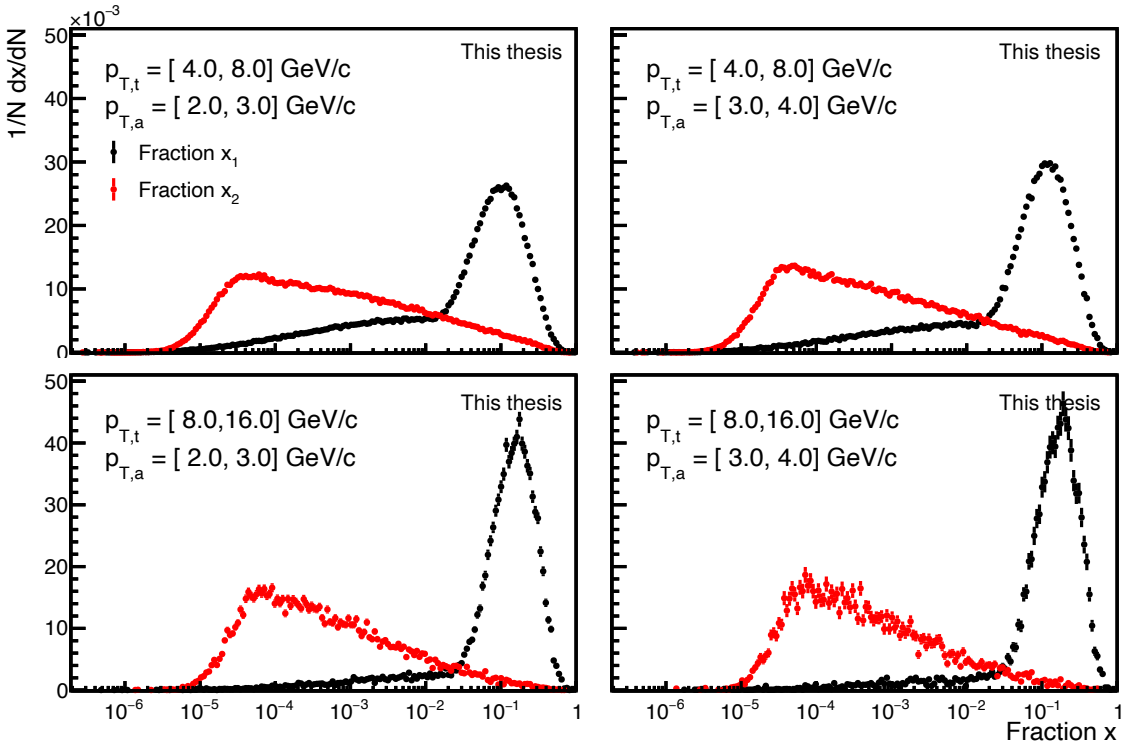

FIGURE 56 The projections of Figure 55 to both x_1 and x_2.

well this measurement can be carried out in the real situation. The success of the measurement highly depends on the reconstruction efficiency of the candidates and thus the efficiency of a single reconstructed π^0 is studied before looking into the more complicated case of correlations.

5.1 Neutral pion reconstruction & reconstruction efficiency

Neutral pions (π^0) are mesons which can not be measured directly because of their short lifetime. However, the detection of π^0's is possible through their decay products. π^0 main decay channel is $\pi^0 \rightarrow \gamma + \gamma$ with the branching ratio of $98.823 \pm 0.034\%$ [138] which means that almost all π^0's from the collision can be measured through this channel. There is a possibility that one or both of the decay photons will form an electron-positron pair, having three or four particles in the final state. The branching ratio of Dalitz decay (the case where one of the virtual photons decays) is $1.174 \pm 0.035\%$ [138], making other decay channels very rare.

Due to the conservation of momentum summing the momenta of the decay products can be used to access the invariant mass of the initial particle. The invariant mass for two-photon pair can be calculated with

$$m_{\gamma\gamma} = \sqrt{2E_{\gamma 1}E_{\gamma 2}(1-\cos\theta_{\gamma\gamma})} \tag{23}$$

where the photon energies are noted as $E_{\gamma 1}$ and $E_{\gamma 2}$, and $\theta_{\gamma\gamma}$ is the opening angle between the two photons. Calculating $m_{\gamma\gamma}$ between all the photons in the event produces invariant mass distribution in which the pairs corresponding to the π^0's can be distinguished from the mass peak at 135 MeV$/c^2$.

The width of the peak depends on the properties of the detector: the better the energy resolution of the detector is the narrower the peak gets. Figure 57 shows an example of invariant mass distribution formed pairing all the photons from PYTHIA8 simulation. On the left side, the photons are taken from the simulation as is. The π^0's form a sharp peak at 135 MeV$/c^2$ and the other photon combinations form the combinatorial background. The photons from the π^0 decay cannot be distinguished from the other photons or and thus the invariant mass is calculated over all possible photon pairs in the event. Those pairs that are treated as possible π^0 candidates are selected by using an invariant mass range depending on the mass peak width. In this case, it is enough to take the counts in one bin[1] but on the right side of Figure 57 a more realistic distribution is presented. The photon energies have been modified by taking the corresponding value for energy resolution $\sigma(E_{\text{true}})$ from the FoCal energy resolution function presented in Table 1 of Chapter 4. Then the true energy E_{true} is smeared by randomizing a new value from a Gaussian distribution of width $\sigma(E_{\text{true}})$. This creates a more realistic mass peak in which to count all the π^0 a larger mass window needs to be selected which also increases the amount of background in the measurement.

The measured π^0 peak position might also be shifted from the nominal value due to detector effects. This can happen especially when there is radiation loss in the detector, for example, a

[1] The physical width of π^0 peak is $\Gamma = \frac{}{\tau} = \frac{6.58 \times 10^{-16}\ \text{eV s}}{8.52 \times 10^{-17}\ \text{s}} \approx 8$ eV, that is 500 times smaller than the bin width in Figure 57. Therefore it is safe to assume that all π^0 are indeed in that one bin.

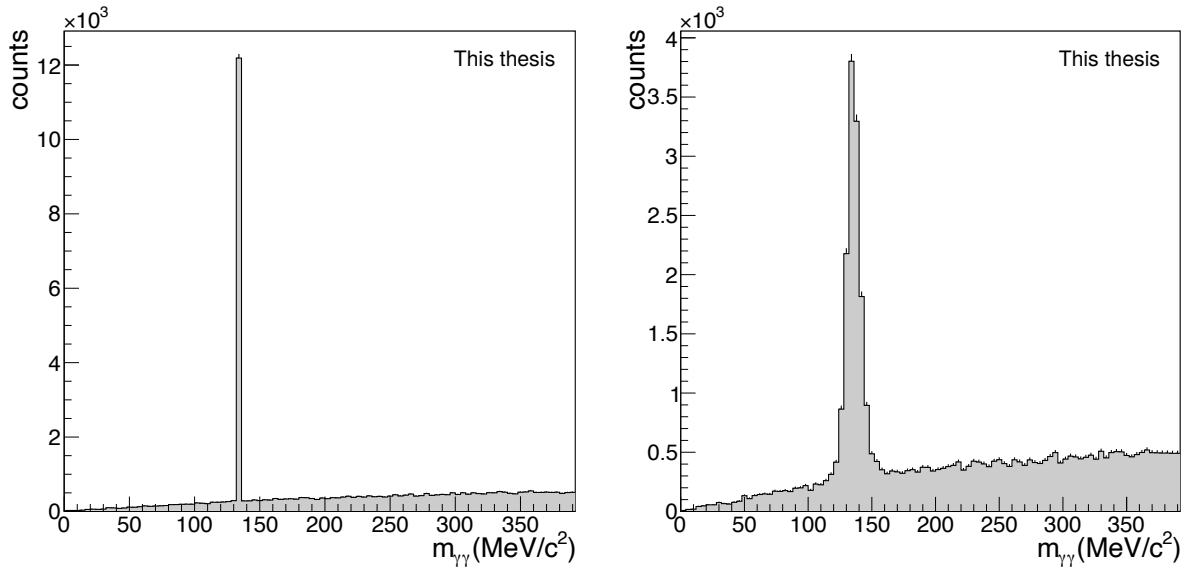

FIGURE 57 Inclusive invariant mass distributions from photons in PYTHIA 8 simulation, without (left) and with (right) energy resolution of FoCal taken into account. In both cases, the combinatorial background is the same, only the peak changes.

large enough particle shower that is not contained in the calorimeter. In this regard, the π^0 peak position is a useful tool for detector energy calibration [139].

The success of reconstructing the π^0 depends on the opening angle between the decay products. The reconstruction will become harder at higher rapidities since the photon energy increase due to

$$E = p_{\mathrm{T}} \cosh \eta. \tag{24}$$

From Equation (23) one can see that if $E_{\gamma 1} E_{\gamma 2}$ term gets on average larger at higher rapidities the cosine term $1 - \cos \theta_{\gamma\gamma}$ needs to suppress the growth so that the equation is equal to π^0 mass, therefore $\theta_{\gamma\gamma}$ needs to have small values. If the spatial resolution of the detector is not good enough to distinguish the decay photons the two showers will be seen as a merged cluster in the detector. The merged clusters can to an extent be analysed via shower shape analysis [81] but in the forward rapidity, the separation between the clusters is extremely small in which case the detector needs very good separation power. To some extent, the separation can be made better by placing the detector far away from the interaction point to assure that the decay products have a large enough displacement when they hit the active material of the detector. For FoCal the placement of 7 meters away from the interaction point, in addition to the high granularity pixel layers of FoCal-E, the separation power for π^0 reconstruction is excellent, as explained in Chapter 2.

The efficiency of π^0 detection is a combination of these points presented here. I will present π^0 efficiency studies regarding FoCal that are important to take into account in the correlations. Loss of associated particles affects the yield and the loss needs to be corrected. This is done by weighting the correlated pair with the efficiency. The loss of triggers however does not need to be corrected since the correlation function is normalized to the trigger count, as is written in Equation 6. If the trigger efficiency were to be taken into account both N_{trigg} and the correlation function would need to be corrected to get the true number of triggers. In that case, the weights would cancel out. The geometrical efficiency depending only on the acceptance of the detector has been studied using PYTHIA8 event generator, and the whole detector efficiency of FoCal

has been estimated via PYTHIA6+GEANT3 simulation package including realistic FoCal geometry and detector response.

5.1.1 Geometrical efficiency

Due to the finite acceptance, the detector may not pick up both photons from the decay. In this case, the π^0 in question cannot be reconstructed. This geometrical efficiency (probability to find both photons in the acceptance) depends on the opening angle of the photons. The efficiency drops at the detector edges, especially at lower p_{T} where the opening angle is larger. To have an idea of how the finite acceptance affects the π^0 reconstruction the π^0 production in FoCal acceptance was studied first with PYTHIA8 in an ideal case. Particles are considered in rapidity $3.2 < \eta < 5.8$ and because of that the acceptance is circularly symmetric. In reality, acceptance is smaller because FoCal geometry is rectangular but the idea here is to get a rough estimate of how the efficiency behaves.

The geometric efficiency is defined here as the ratio of the number of "detected" π^0 (pions of which both decay photons can be found from the detector acceptance) to all π^0 in FoCal acceptance. This is shown in Figure 58a as the function of both p_{T} and pseudorapidity η. The figure shows that the efficiency due to the missing photons on the edges is reduced mainly at p_{T} values below 1 GeV/c. At the small η boundary the opening angles of low p_{T} π^0's get so large that a clear boundary where the reconstruction can not be done is seen. However, at the large η boundary the effect is the opposite: if the opening angle is large enough the other decay photon can be seen on the other side of the beam pipe. The difference is demonstrated in Figure 59.

Figure 58b shows the same data divided into several η bins. From this figure it is clear to see that, excluding the lowest and highest η bins ($[3.2, 3.5]$ and $[5.5, 5.8]$) the efficiency starts to converge to a constant value of 0.98 after 1 GeV/c. In the simulations π^0's are allowed to decay via all decay channels and therefore the efficiency converges to the value corresponding

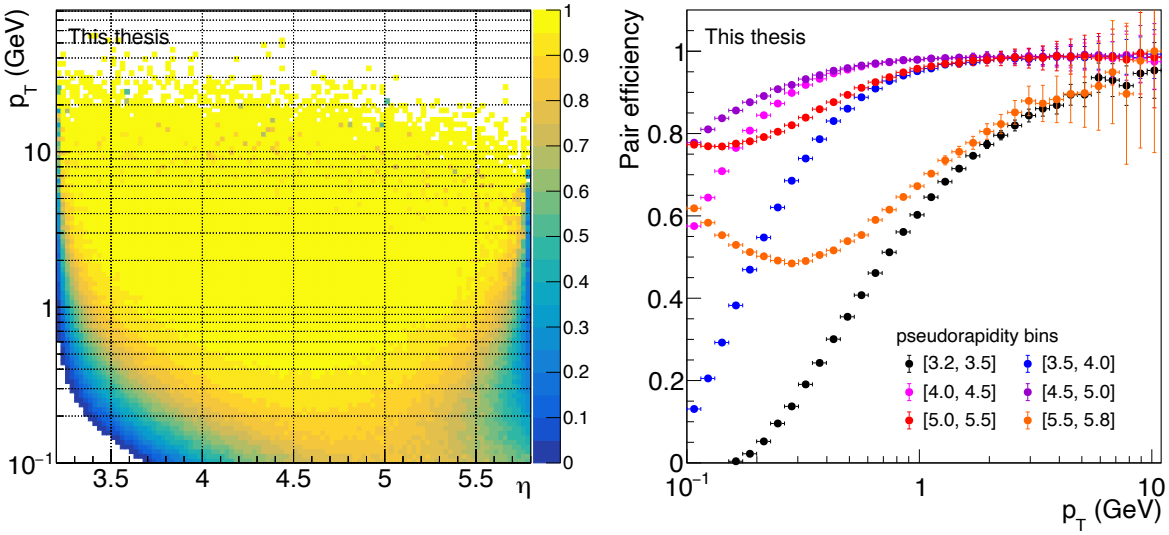

(a) The probability as a function of π^0 pseudorapidity and transverse momentum.

(b) The same probability as a function of transverse momentum, divided into several pseudorapidity bins.

FIGURE 58 Probability to see π^0 in FoCal acceptance ($\pi^0_{\mathrm{detected}}/\pi^0_{\mathrm{MC}}$). The particles are generated using PYTHIA8.

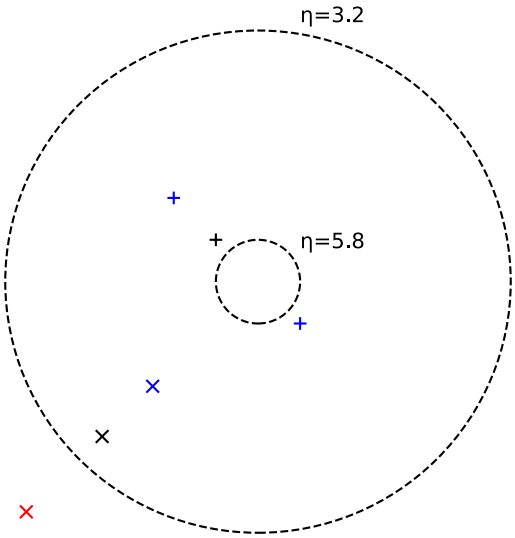

FIGURE 59 Pseudorapidity range visualized in $x-y$ plane. Black markers represent two π^0 with same p_{T} hitting the opposite edges of the acceptance and the colored markers in their vicinity are their decay photons. In both cases, the opening angle is the same but only the inner particle marked with + can be reconstructed since both photons are inside the acceptance.

to the branching ratio of $\pi^0 \to \gamma\gamma$ channel. It turns out that realistically 1 GeV$/c$ starts to be quite difficult for FoCal to measure and thus the analyses have been restricted for p_{T} values higher than 2 GeV$/c$. For π^0 with $p_{\mathrm{T}} > 2$ GeV to suppress the efficiency drop due to the loss at the edges it is sufficient to cut 0.2 from the rapidity on the edges. In practice, this means that the photons are taken in the full acceptance but the analysis of the reconstructed π^0's is restricted to the smaller acceptance.

5.1.2 Detector efficiency

In reality, the detector is not circularly symmetric but is built from rectangular towers with gaps between them. Therefore the detector has dead areas that affect the reconstruction efficiency. Since the particles are reconstructed from the energy deposit of the particle shower the energy losses from leakage affect the efficiency, as well as the energy losses to the material in front of the detector. Also, the performance of the clusterization algorithm on the edges, splitting of the clusters and energy sharing between near clusters can affect the reconstruction efficiency in analysis.

The clusterization in the electromagnetic calorimeter is done in segments. FoCal-E has been divided into six longitudinal segments as shown in Figure 60. Segments 1 and 3 consist of high granular pixel layers (HG layer) and other segments have four low-granularity silicon PAD layers (LG layers) each. In the FoCal clusterization algorithm, the clusterization is first done in each segment to get the seeds for the sub-clusters. The seeds are the starting points for the clusterization algorithm since they define the centers of the sub-clusters. For some layers pre-seeds, seed positions determined by another layer, are used. After sub-clusters are found the full-detector clusters are then created by combining the sub-clusters for each layer. This includes geometrical matching between the segments, and cluster splittings if two pixel clusters are matched with one pad segment cluster. A more detailed description of the algorithm can be

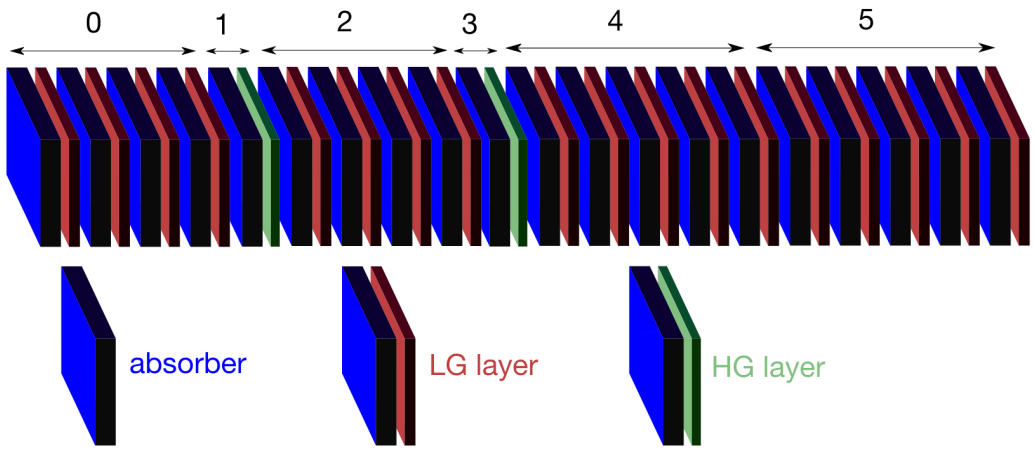

FIGURE 60 FoCal-E longitudinal segmentation used for the clusterization of electromagnetic showers. Schematic taken from [46], reproduced under the license CC BY 4.0.

found from FoCal Letter of Intent [46]. In future, a clusterization algorithm in which all layers are read individually instead of segments is planned to be implemented.

The detector level π^0 efficiency for FoCal was studied using the ALICE simulation framework. The Run 3 versions of FIT and beam pipe were implemented into the simulation framework but other detectors used their Run 2 geometries. This is because while writing this the FoCal geometry had not been yet implemented in the new O^2 analysis framework. However, FIT and the beam pipe make the largest contribution to the material in front of FoCal, thus the simulations correspond to the Run 4 circumstances well geometry-wise from the FoCal point of view. The simulations are done with a simple particle gun to generate neutral pions with uniform distribution of p_T from 2 GeV/c to 20 GeV/c to the FoCal acceptance. The particle gun creates one π^0 per event which makes it convenient to compare detector output to the single Monte Carlo particle. The particle transport is handled by GEANT3 [140].

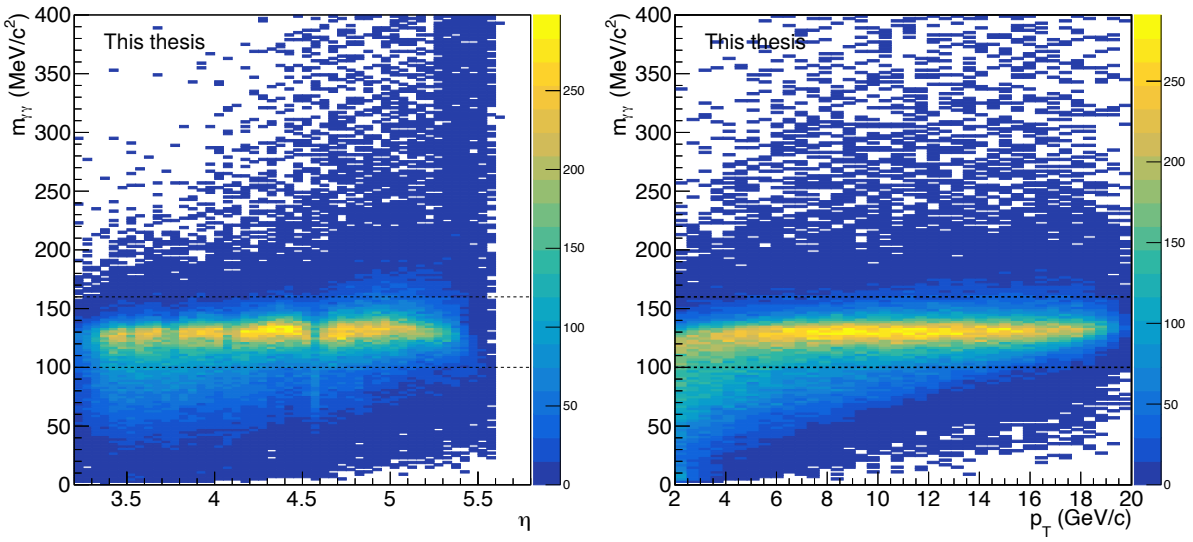

FIGURE 61 Cluster invariant mass distribution as function of rapidity η (left) and p_T (right). The mass window used to study reconstructed π^0 efficiency is indicated with dashed lines.

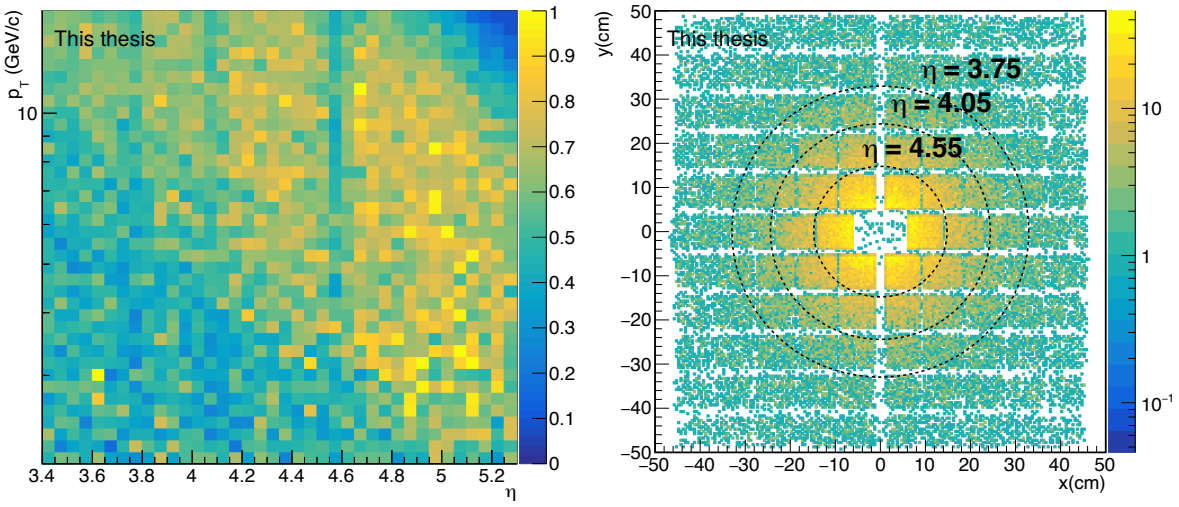

FIGURE 62 π^0 reconstruction efficiency as funcion of both rapidity η and transverse momentum p_{T} (left). The efficiency drops at certain rapidity values and these can be traced back to the gaps between FoCal-E towers which can be seen on the right side plot.

To ensure that the mass peak is visible in the whole acceptance, or if not, what acceptance range should be used in the analysis the invariant mass distribution was plotted against pseudorapidity. Similarly, the invariant mass was also checked in relation to the transverse momentum of the reconstructed π^0. Figure 61 shows both distributions. Here only the π^0 candidate with mass closest to true π^0 mass (135 MeV$/c^2$) is selected in each event, which leaves out some background resulting from low energy conversion photons and incorrectly split clusters. From the η dependent mass distribution, it can be seen that the π^0 peak is visible at the lower boundary of FoCal acceptance ($\eta = 3.2$) but at higher rapidities, the reconstruction efficiency drops around $\eta = 5.4$. Therefore the detector level analyses presented here are restricted to $\eta = [3.4, 5.3]$. As the function of p_{T}, the mass peak position and width start to deviate at values $p_{\mathrm{T}} < 5$ GeV$/c$ but otherwise, the peak position stays constant over the whole range.

The reconstruction efficiency for π^0 candidates is shown in Figure 62 (left side). Again, the reconstructed π^0 histogram is filled with the candidate with mass closest to 135 MeV$/c^2$. This is then divided with the Monte Carlo truth, meaning the p_{T} and η distribution of the generated π^0's. There are clear drops in efficiency around certain values of η, for example at $\eta \sim 4.6$. This can be traced to be caused by the air gaps between the modules. The geometry can be seen more clearly on the right side in Figure 62, plotting of x and y coordinates of the reconstructed π^0 candidates. The coordinates are calculated at $z = 700$ cm which corresponds to the front side of the detector. The dotted lines correspond to different pseudorapidies and, as can be seen, the efficiency drops at pseudorapidities that overlap with the gaps. However, the efficiency behaves similarly as in the studies presented previously in the Letter of Intent [46], in which the efficiency is presented as a function of p_{T} in three η bins between $4.0 < \eta < 5.5$. The efficiency determined in this thesis is a bit worse in certain areas compared to the LOI results because the air gaps were implemented to the geometry after the studies presented in LOI.

The projections of reconstructed and Monte Carlo π^0 distribution to p_{T} and η are shown in Figure 63. The projection to η is taken over the whole p_{T} range of simulated particles, in the case of projection to p_{T} rapidity is restricted to the range where the mass peak is visible,

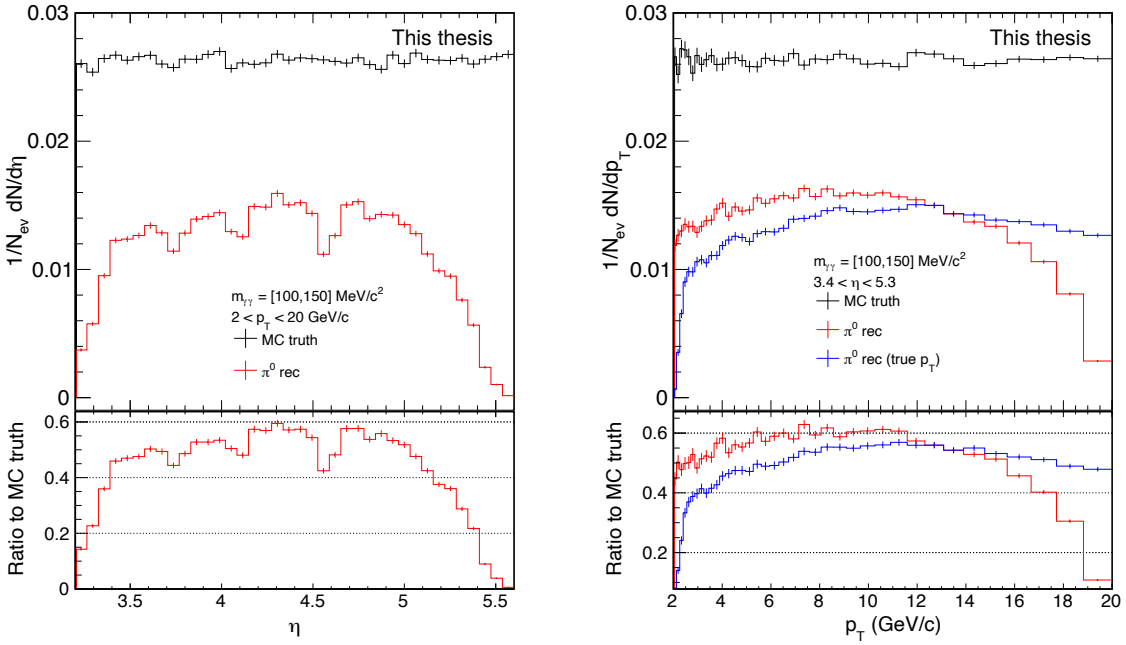

FIGURE 63 Reconstructed π^0 distribution as a function of rapidity and transverse momentum.

that is $\eta = [3.4, 5.3]$. In the p_{T} projection the reconstructed π^0 spectrum using the true p_{T} of the simulated particle is also shown. Here it can be seen that the transverse momentum reconstruction does not fully recover the true value but π^0 are flowing from higher bins to lower ones. In the largest p_{T} bin there is over 30% difference between the data with reconstructed p_{T} and the true p_{T}.

In conclusion, the reconstructed π^0 efficiency can not be represented via a single constant like in the case of PYTHIA. In the realistic detector simulation, the efficiency highly depends on both the rapidity and p_{T} of the particle. Another way to estimate the efficiency would be to compare the reconstructed energy to the true particle energy. In this thesis work, it has not been considered if it is better to define the efficiency as a function of transverse momentum or energy to correct the yields, only the p_{T} dependent efficiency has been used. π^0 efficiencies shown in Figure 32 are used in analyses onwards.

5.1.3 Event mixing

Event mixing is a technique that removes any correlations that are not related to physics. As mentioned when introducing the correlation function in Section 2.3.1, the mixed event correlation $B(\Delta\phi, \Delta\eta)$ is calculated between two particles from different events. This destroys any correlation that arises from the actual physics and leaves the possible correlation from other sources. This means for example detector inefficiencies or particle production related to the geometry that might otherwise affect the measurement. For example, in the case of π^0–π^0 correlations in FoCal the conversion photons from FIT mechanical structures can affect the correlation, in a similar manner as in the FIT event plane measurement in Section 3.2.1. The mixed event also corrects for the finite η acceptance of the detector.

In an ideal situation, the mixed event correlation function would be flat in azimuthal angle and have triangular shaped pseudorapidity distribution. The triangular shape is caused by the

limited detector acceptance. At the particle level, the mixed event distribution would still correct the efficiency in $\Delta\eta$ direction but it was not considered since in that case, $\Delta\phi$ is flat. The acceptance correction is not an issue since the comparison with Monte Carlo truth and the reconstructed π^0 correlations at the particle level are done in the same acceptance. In the full detector simulations $\Delta\phi$ there can be deviations and thus the mixed event is discussed more in the context of FoCal π^0–π^0 performance in Section 5.3.

5.2 Background subtraction

In forward π^0 –π^0 correlations both trigger and associated particle are reconstructed using only information about the invariant mass which has a combinatorial background. To some extent, the background can be reduced by imposing specific cuts for example to energy. In this work, the energy cut is applied in the form of an asymmetry cut that takes into account the energies of both combined photons. As mentioned before, the correlated background is featured in the correlation function and can be taken into account via the sideband method. In the next section, the effects of asymmetry cut to the π^0 reconstruction are shown, and after that, the sideband method is reviewed in detail and the level of background correlations from different sources is estimated.

5.2.1 Asymmetry cut

A way to exclude fake pairs from the analysis is to use an asymmetry cut. It is applied when calculating the invariant mass between the cluster pairs. This is done by calculating the asymmetry parameter

$$\alpha = \frac{|E_1 - E_2|}{E_1 + E_2}, \tag{25}$$

between the two clusters of energies E_1 and E_2 and excluding pairs with asymmetry larger than a pre-defined value of α_{thres}. If the π^0 decay is symmetric i.e. $E_1 \approx E_2$ the asymmetry is in the vicinity of 0. When looking at the asymmetry parameter distribution purely for photons from π^0 decays it is quite flat, only dropping when going near 1. However, the background contributions which occupy the lower energies skew the distribution so that more pairs are found with α near 1. Then a large number of fake pairs can be excluded from π^0 selection by leaving out pairs at large α.

Asymmetry distributions for PYTHIA smeared photons and clusters from the full detector simulation are presented in Figure 64. Monte Carlo truth here is calculated only between the two decay photons from π^0. To better compare the shapes of the distributions MC truth and PYTHIA results are scaled by values 65 and 20 respectively. It can be seen that the number of π^0 drops when nearing $\alpha = 1$. When the asymmetry between other photons or clusters is added to the distribution the distribution increases at higher values due to the background pairs. In the case of clusters, the number of pairs per event is much higher due to the larger combinatorial background and the larger mass window ($m_{\gamma\gamma} = [50,200]$ GeV/c^2). Imposing an asymmetry cut of $\alpha_{\text{thres}} = 0.8$ reduces the background already significant amount as can be seen in Figure 65. Even larger cut ($\alpha_{\text{thres}} = 0.5$) still reduces background but this starts to affect the π^0 efficiency significantly. The significance of the asymmetry cut is especially notable in

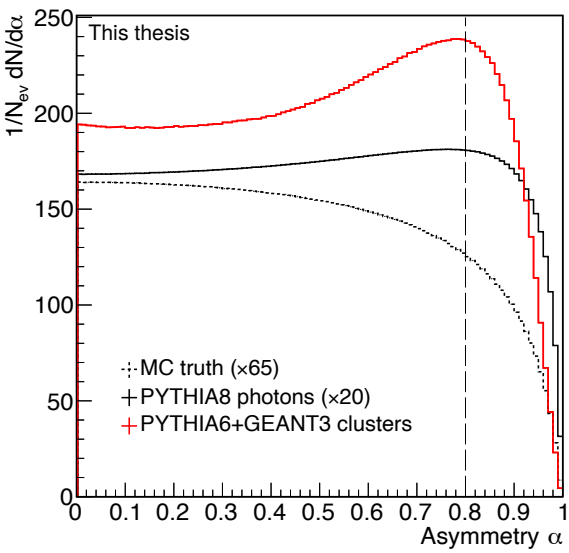

FIGURE 64 Asymmetry α calculated from energy smeared PYTHIA MC photons and full simulation clusters, compared to MC truth.

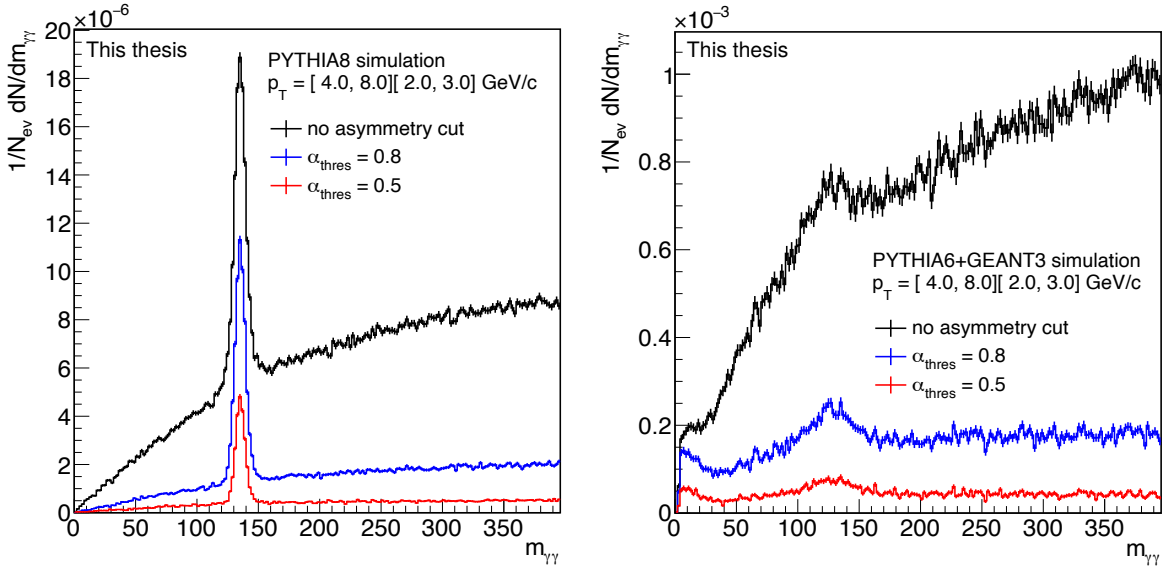

FIGURE 65 The effect of asymmetry cut α_{thres} on the invariant mass distribution from PYTHIA8 simulation (left) and full GEANT3 simulation (right). The mass peak distributions are from the correlation analysis in which the associated particle masses are saved according to both trigger and associated particle p_{T}, hence the binning $p_{\text{T}} = [4.0, 8.0]\,[2.0, 3.0]$ GeV/c.

the reconstruction of the associated pions since with it the peak is more prominent. It needs to be noted that the signal-to-background ratio here is small because the associated π^0 candidate is saved only if there is a trigger particle found in the same event. This is related to the sideband method and explained in Section 5.2.2.

To determine the optimal value of α_{thres} to be used in the full detector simulation the signal-to-background (S/B) ratio was determined with different asymmetry cuts. This is presented in Figure 66. The S/B ratio is determined by fitting the mass distribution in each p_{T} bin with a Gaussian (the mass peak) combined with a second-order polynomial (the background). The amount of background is then calculated from the integral of the polynomial in the mass window

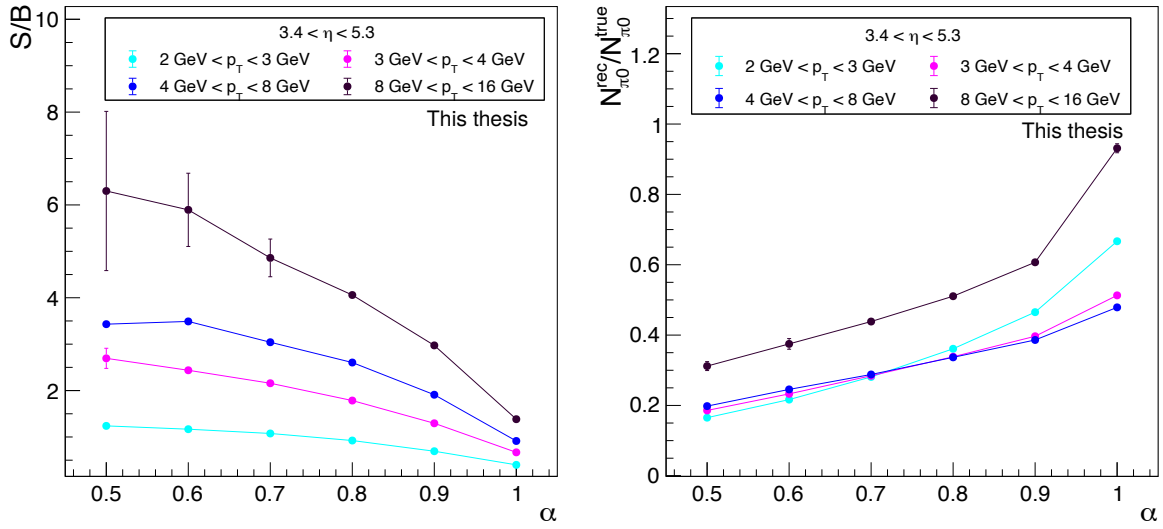

FIGURE 66 The signal-to-background ratio as a function of asymmetry cut α_{thres}, calculated from the full detector simulation is shown on the left figure. The detector level efficiency over different p_{T} ranges as a function of α_{thres} can be seen in the right figure.

whereas the amount of signal is the integral of the mass histogram minus the background from the fit. Based on this the S/B ratio is already improved at $\alpha = 0.9$. The S/B ratio does not get significantly better with values lower than 0.8/0.9 at lower p_{T} but can improve the ratio greatly at large p_{T}. As seen in the case of the mass distribution the cut does worsen the efficiency if a larger cut is used. To keep a good balance with the S/B ratio and the efficiency $\alpha_{\text{thres}} = 0.8$ was selected for the analyses presented onwards.

5.2.2 Sideband method

In the measurement, the π^0–π^0 correlation function can be divided into different components depending on what the correlated candidates actually are. The true correlation wanted in this measurement is the one between π^0's but there can be pairs in which neither the trigger nor associated particle is a true π^0. It can also happen that either the trigger or the associated particle is a fake π^0. Taking into account all these situations gives us a way to write out the measured correlation function by the means of four different components:

$$f_{\text{mass,mass}} = f_{\text{true,true}} + f_{\text{true,fake}} + f_{\text{fake,true}} + f_{\text{fake,fake}} \tag{26}$$

where the first subscript refers to the nature of the trigger particle and the second one to the associated particle, 'mass' meaning that the pair is taken from the mass peak region, 'true' meaning real π^0, and 'fake' meaning reconstructed candidate that falls into the mass window but is not a π^0.

The four components can not be measured separately, only $f_{\text{mass,mass}}$ is measurable. The real signal, $f_{\text{true,true}}$, can however be extracted if the other components are estimated and subtracted from $f_{\text{mass,mass}}$. This is where the sidebands around the mass peak in the π^0 mass distribution can be used to estimate the shapes and magnitudes of $f_{\text{true,fake}}$, $f_{\text{fake,true}}$, and $f_{\text{fake,fake}}$. The sidebands include only pairs that are not from the same π^0 mother. The pairs from sidebands can then be used as triggers and associated particles to construct correlations between the pairs from the mass region to get different combinations. The correlation functions constructed this way are

$$f_{\text{mass,side}} = f_{\text{true,fake}} + f_{\text{fake,fake}} \tag{27}$$

$$f_{\text{side,mass}} = f_{\text{fake,true}} + f_{\text{fake,fake}} \tag{28}$$

$$f_{\text{side,side}} = f_{\text{fake,fake}} \tag{29}$$

Then using Equations (26)–(29) $f_{\text{true,true}}$ can be expressed in terms of the measurable correlation functions $f_{\text{mass/side,mass/side}}$. The functions need to be scaled correctly when substituting the components with other equations. For example, $f_{\text{fake,fake}}$ in Equation (28) does not include the same amount of pairs as in Equation (29) and therefore the number of pairs needs to be taken into account. The scaling can be sorted out by dissecting the correlation functions into the number of pairs. Then Equations (26)–(29) in terms of number of pairs are

$$N_{\text{mass,mass}} = N_{\text{S}}^{\text{t}} N_{\text{S}}^{\text{a}} + N_{\text{S}}^{\text{t}} N_{\text{B}}^{\text{a}} + N_{\text{B}}^{\text{t}} N_{\text{S}}^{\text{a}} + N_{\text{B}}^{\text{t}} N_{\text{B}}^{\text{a}} \tag{30}$$

$$N_{\text{mass,side}} = N_{\text{S}}^{\text{t}} N_{\text{B}}^{\text{a}^*} + N_{\text{B}}^{\text{t}} N_{\text{B}}^{\text{a}^*} \tag{31}$$

$$N_{\text{side,mass}} = N_{\text{B}}^{\text{t}^*} N_{\text{S}}^{\text{a}} + N_{\text{B}}^{\text{t}^*} N_{\text{B}}^{\text{a}} \tag{32}$$

$$N_{\text{side,side}} = N_{\text{B}}^{\text{t}^*} N_{\text{B}}^{\text{a}^*} \tag{33}$$

where t and a refer to the trigger and associated particle, and * to particles taken from the sideband. Now to substitute, for example $N_{\text{B}}^{\text{t}^*} N_{\text{B}}^{\text{a}}$ in Equation (32) with Equation (33) the number of pairs need to be scaled correctly. In this case, the number of triggers are the same, since in

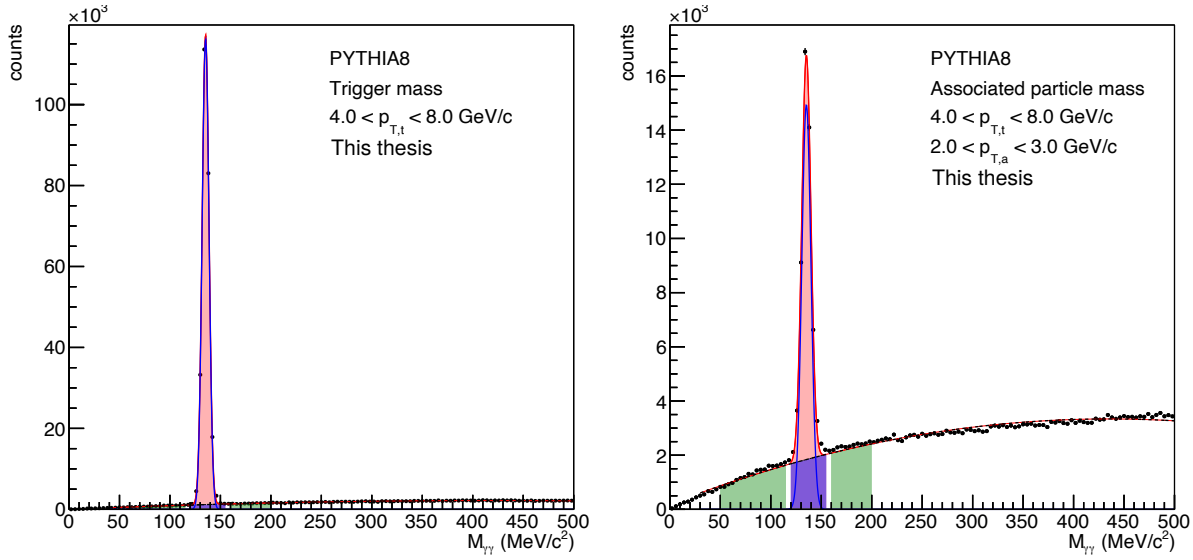

FIGURE 67 The particle level π^0 mass distributions for the lowest p_{T} bin used in this study. The sidebands used to estimate the background candidates in the mass window (marked with blue) are marked with green color.

both cases they are taken from the sideband, but the number of associated particles differs. Thus to fix the number of associated particles $N_{\mathrm{side,side}}$ needs to be scaled with factor $\alpha = N_{\mathrm{B}}^{\mathrm{a}}/N_{\mathrm{B}}^{\mathrm{a}*}$ which then gives

$$\alpha N_{\mathrm{side,side}} = \alpha N_{\mathrm{B}}^{\mathrm{t}*} N_{\mathrm{B}}^{\mathrm{a}*} = \frac{N_{\mathrm{B}}^{\mathrm{a}}}{N_{\mathrm{B}}^{\mathrm{a}*}} N_{\mathrm{B}}^{\mathrm{t}*} N_{\mathrm{B}}^{\mathrm{a}*} = N_{\mathrm{B}}^{\mathrm{t}*} N_{\mathrm{B}}^{\mathrm{a}}.$$

Working out the substitution in Equation (31) in the same manner by using scaling factor $\beta = N_{\mathrm{B}}^{\mathrm{t}}/N_{\mathrm{B}}^{\mathrm{t}*}$ leads into

$$\beta N_{\mathrm{side,side}} = \beta N_{\mathrm{B}}^{\mathrm{t}*} N_{\mathrm{B}}^{\mathrm{a}*} = \frac{N_{\mathrm{B}}^{\mathrm{t}}}{N_{\mathrm{B}}^{\mathrm{t}*}} N_{\mathrm{B}}^{\mathrm{t}*} N_{\mathrm{B}}^{\mathrm{a}*} = N_{\mathrm{B}}^{\mathrm{t}} N_{\mathrm{B}}^{\mathrm{a}*},$$

and in Equation (30)

$$\alpha\beta N_{\mathrm{side,side}} = \alpha\beta N_{\mathrm{B}}^{\mathrm{t}*} N_{\mathrm{B}}^{\mathrm{a}*} = \frac{N_{\mathrm{B}}^{\mathrm{a}}}{N_{\mathrm{B}}^{\mathrm{a}*}} \frac{N_{\mathrm{B}}^{\mathrm{t}}}{N_{\mathrm{B}}^{\mathrm{t}*}} N_{\mathrm{B}}^{\mathrm{t}*} N_{\mathrm{B}}^{\mathrm{a}*} = N_{\mathrm{B}}^{\mathrm{t}} N_{\mathrm{B}}^{\mathrm{a}}.$$

The mixed components in $N_{\mathrm{mass,side}}$ and $N_{\mathrm{side,mass}}$, $N_{\mathrm{S}}^{\mathrm{t}} N_{\mathrm{B}}^{\mathrm{a}*}$ and $N_{\mathrm{B}}^{\mathrm{t}*} N_{\mathrm{S}}^{\mathrm{a}}$, are scaled with α and β respectively so that the number of pairs corresponds the numbers in Equation (30).

After determining the scaling factors and making the needed substitutions the real correlation function can be written as

$$f_{\mathrm{true,true}} = f_{\mathrm{mass,mass}} - \alpha f_{\mathrm{mass,side}} - \beta f_{\mathrm{side,mass}} + \alpha\beta f_{\mathrm{side,side}}. \tag{34}$$

To estimate the number of triggers and associated particles for the scaling factors the mass distributions are saved separately in the trigger and associated particle p_{T} bins. The scaling factors are then calculated by estimating the combinatorial background in the mass peak by fitting and subtracting the results of the fit from the counts in the mass window. These numbers are also needed in the sideband and in this case the counts are taken straight from the sideband

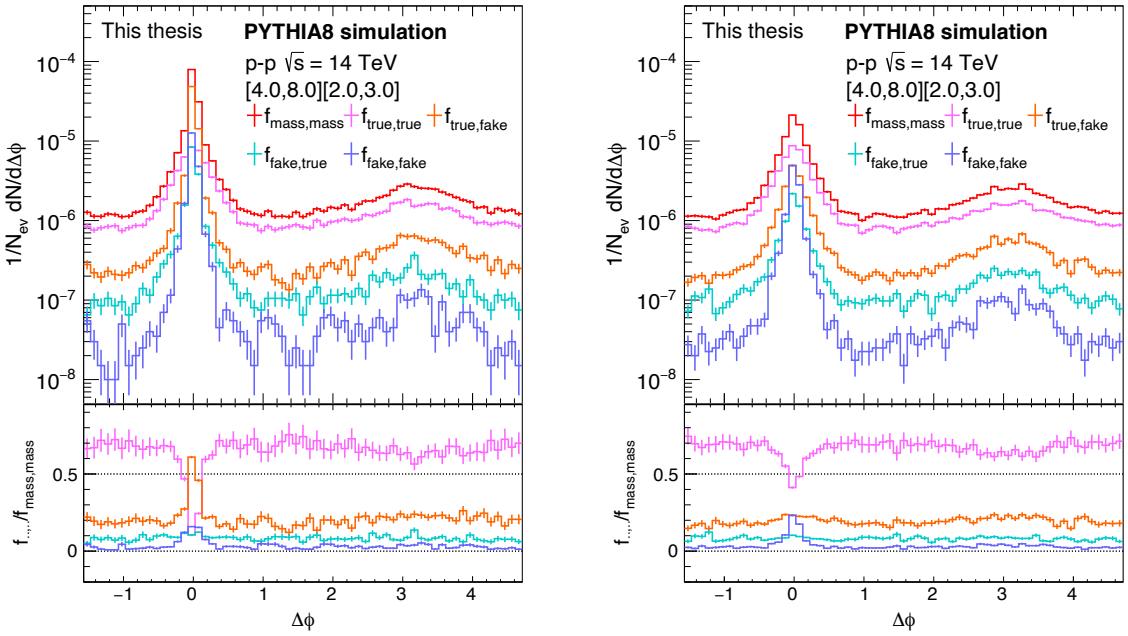

(a) Shared photons between the trigger and associated candidate are not taken into account

(b) The associated pairs that share a photon with the trigger are excluded.

FIGURE 68 $f_{\text{mass,mass}}$ divided into its four components shown in Equation (26).

regions in the mass histogram. The mass histograms for both trigger and associated particle in particle level are presented in Figure 67 for bin $[4.0,8.0][2.0,3.0]$ GeV$/c$. To get the correct numbers it is important that the associated particles are saved only then when there is a trigger particle found in the same event. Thus the associated particle mass distribution has also a dependence on the trigger particle p_{T}. At particle level π^0 peak is narrow and the combinatorial background is not large, especially in the case of the trigger.

PYTHIA simulations to estimate the correlated background and validate the sideband method were run with `pThard=2` setting, meaning that only events in which the outgoing partons have transverse momenta larger than 2 GeV$/c$ are considered. This is to reduce the computing time since low-momentum particles dominate in the collisions. Transverse momentum of 2 GeV$/c$ is any way at the lower limit of FoCal capabilities and from this point of view it is not necessary to consider the correlations at lower momentum.

In the simulation PYTHIA saves the particle history and therefore the initial source of the photon can be checked. This makes it possible to see whether the π^0 candidate is actually constructed from decay products of the same mother and thus the contributions of different components in Equation (26) can be constructed. Figure 68a shows the correlation between reconstructed π^0 candidates divided into its components ($f_{\text{true,true}}$, $f_{\text{true,fake}}$, $f_{\text{fake,true}}$, and $f_{\text{fake,fake}}$) with trigger bin $[4.0,8.0]$ and associated particle bin $[2.0,3.0]$. The correlation function has been normalized to the number of events but not to the number of triggers; the purpose of the figure is to compare the amount of background in the correlation and therefore it is not necessary to look at per trigger distribution yet.

As can be seen, the correlation function is mainly composed of $f_{\text{true,true}}$ component, making up $\sim 70\%$ of the overall "measured" function. On the away side the ratio of the true component

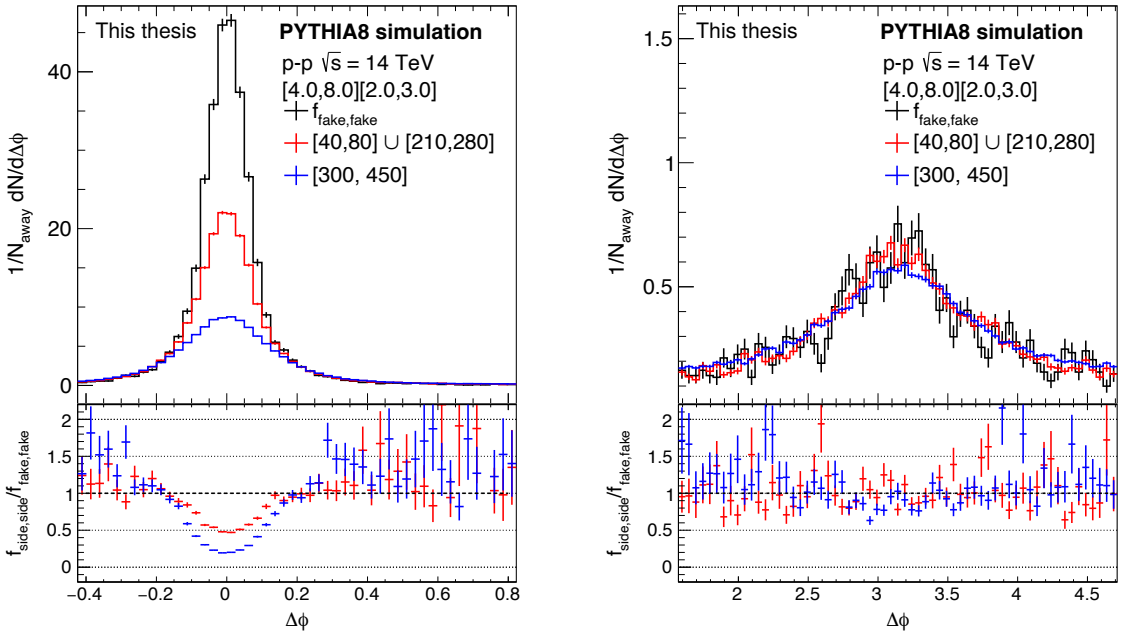

FIGURE 69 Comparison between the sideband correlation $f_{\text{side,side}}$ and the true background correlation from the measured function ($f_{\text{fake,fake}}$). The near side (left) and away side (right) are calculated are shown in the case of two different sidebands. The ratios on the lower panel correspond to the colors on the upper panel.

to $f_{\text{mass,mass}}$ is quite constant although a slight deviation can be observed. A more striking difference is on the near side: there the near side peak consists of $f_{\text{true,fake}}$ pairs even as much as 60%. $f_{\text{fake,true}}$ component is quite small and constant throughout the range. Even smaller contribution is also by $f_{\text{fake,fake}}$ pairs but this component does peak at the near side $10-15\%$.

The large background contribution on the near side can be to an extent explained by the selection of trigger and associated particles. At first, when the π^0's were reconstructed it was not considered that the trigger and associated particle could share the same photon. This leads to a situation where $\Delta\phi$ between two particles that share the same photon is very small, especially if the photons paired with the shared photon belong to the same jet. Having the same photon in two different decays is unphysical and should be resolved by a choice: either the photon belongs to the trigger or the associated particle. We chose to pair the shared photons with the trigger and exclude any associated particles sharing the trigger photons from the analysis. The effect of this choice can be seen in Figure 68b. The away side stays similar as before but $f_{\text{true,fake}}$ contribution on the near side is almost completely flattened. The largest non-constant background contribution to the near side comes now from $f_{\text{fake,fake}}$ to which the shared photon exclusion did not influence on.

As discussed previously the correlated background π^0–π^0 correlations could be on the paper be removed by utilizing background pairs from mass distribution sidebands. The method is based on the notation that the background correlations would be similar in the mass window and the sideband which is postulated in Equation (29). $f_{\text{side,side}}$ is also an integral part of the other correlations and therefore it is good to examine how well the component describes the background. The easiest first check to see if $f_{\text{side,side}} = f_{\text{fake,fake}}$.

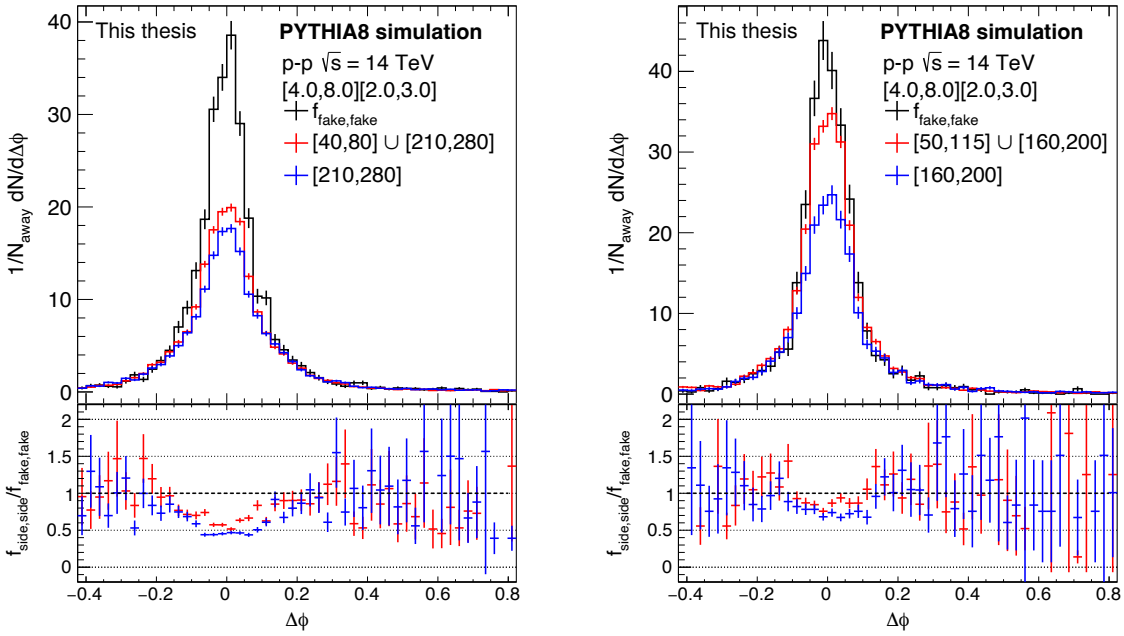

FIGURE 70 Comparison between the sideband correlation $f_{\text{side,side}}$ and the true background correlation from the measured function ($f_{\text{fake,fake}}$). The ratios on the lower panel correspond to the colors on the upper panel.

Figure 69 shows $f_{\text{side,side}}$ calculated in different sidebands, plotted alonside $f_{\text{fake,fake}}$. The distributions are normalized to the away side counts. The sideband correlation was checked in two sidebands: at $[40,80] \cup [210,280]$ from both sides of the peak and at a larger mass of $[300,450]$. As can be seen on the left side figure $f_{\text{side,side}}$ on the near side differs significantly from the shape of $f_{\text{fake,fake}}$. Especially in the case where the sideband is taken only from the right side of the peak the sharp shape of the correlation is almost completely gone. On the away side $f_{\text{side,side}}$ follows the overall shape of the true background correlation with both sideband selections even though a small difference can be observed. Therefore we only focus on the near side while studying the shape of $f_{\text{side,side}}$.

Since it seems that the shape of $f_{\text{side,side}}$ corresponds $f_{\text{fake,fake}}$ best when the sideband is taken closer to the mass peak and from both sides, the comparison was done with another sideband selection. Also, a smaller mass window of the π^0 candidates was selected ($[120,155]$ in contrast to the default of $[110,160]$). The differences between these selections in the smallest p_{T} bin can be seen in Figure 70. Even though the correlation near $\Delta\phi = 0$ still cannot be constructed with the sidebands fully it is evident that the sideband closer to the peak yields better results. Because in the real situation, which is discussed in Section 5.3, the sidebands can likely be selected only from the other side of the peak the correlations without the smaller mass range are also shown. This confirms that selecting background pairs from both sides would benefit the method.

5.2.3 Sideband method validation in pp and pPb

To verify that the sideband method truly recovers the true π^0–π^0 correlation the method was applied to PYTHIA8 simulated data samples. Comparison to Monte Carlo truth and the correlation without sideband correction i.e. $f_{\text{mass,mass}}$ component is shown in Figure 71. The

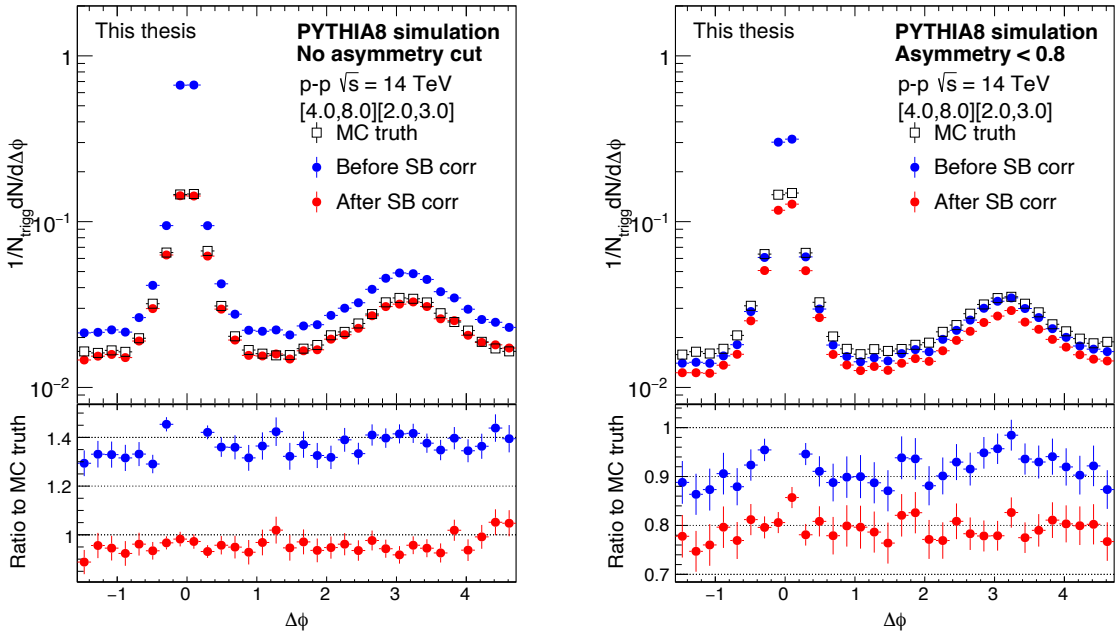

FIGURE 71 The effect on correlation function when the asymmetry cut is implemented. The left-hand side figure shows the correlation when no asymmetry cut is used, on the right side π^0 candidates with asymmetry larger than 0.8 have been left out from the analysis.

distributions have been normalized to the trigger count: in 'Before SB' case the trigger count is the integral over the mass window and in 'After SB' the same integral minus fitted combinatorial background (SB referring to the sideband subtraction). Without the subtraction, the yields would be larger than what the true correlation gives. Also, the sharp peak on the near side vanishes when the sideband method is used. The ratio to Monte Carlo truth is slightly below 1 in the case of the sideband corrected correlation function. This is expected since even though the reconstruction efficiency is nearly 100% with the η cut of 0.2 the branching ratio has not been taken into account.

Any kind of loss of pions affects the sideband corrected correlation and therefore the effect of asymmetry cut was also studied on the particle level. This is because the number of pairs in the correlation function does not come out right if pions are lost. Figure 71 shows how the cut affects the correlation function in bin $[4.0,8.0][2.0,3.0]$, the lowest bin combination used in the analyses in this thesis. The mass window and sidebands are chosen to be the optimal ones used in the near side background correlation study[2]. The left figure shows the correlation function without any limitations to the photon energy, on the right figure the photon pairs with $\alpha > 0.8$ have been excluded. When no cut is imposed to the data the SB correction works as it should and recovers the true correlation, excluding the near side due to the problems explained in Section 5.2.2. Removing candidates via asymmetry cut reduces pairs in the correlation function but SB correction cannot produce the true correlation any more. Therefore the loss of pairs needs to be taken into account when filling the correlation histograms.

When asymmetry cut is used both trigger and associated particle efficiencies are altered. The loss of triggers is not problematic since the distributions are normalized to the trigger count.

[2] Mass window of $[120,155]$ MeV$/c^2$ and sidebands $[50,115]$ MeV$/c^2$ and $[160,200]$ MeV$/c^2$

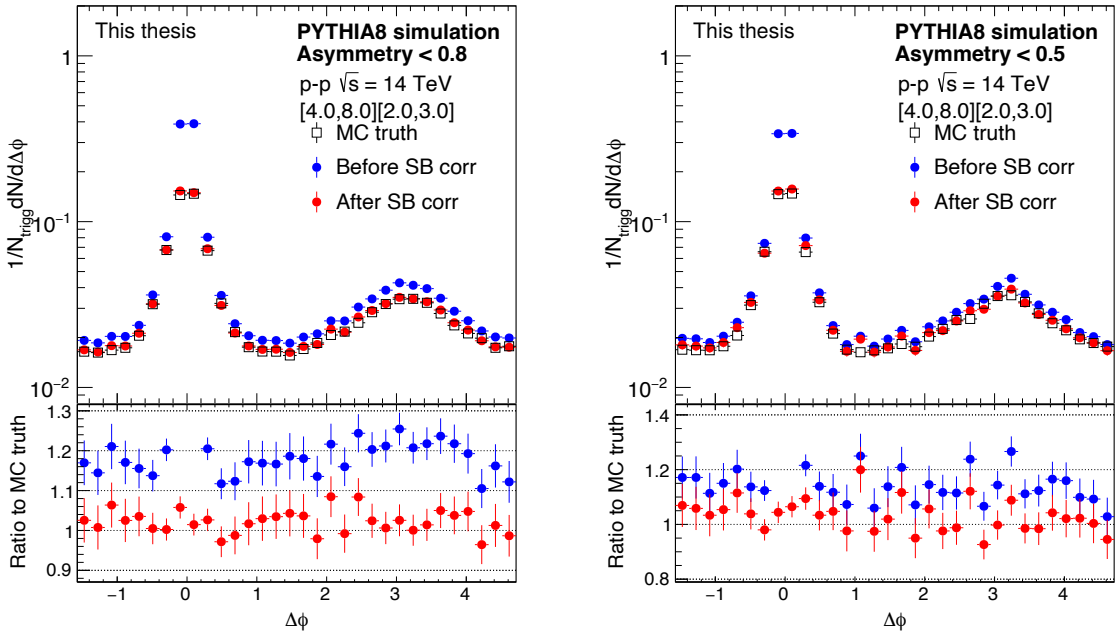

FIGURE 72 The results when asymmetry cut of $\alpha_{\text{thres}} = 0.8$ and $\alpha_{\text{thres}} = 0.5$ is used but the associated particle is weighted with $w = 0.78$ and $w = 0.48$ respectively.

The associated particles however need correction. On PYTHIA level the efficiency is straightforward to determine and it is directly comparable to the asymmetry cut used. In the case of $\alpha_{\text{thres}} = 0.8$ approximately 20% of the associated particles are discarded. Then to correct for this effect, the associated particle is weighted with $w = 0.78$ when the trigger–associated particle pair is filled to the histogram. The results of weighting can be seen in Figure 72. Overall background in the correlation function without SB correction is reduced but the difference to the true correlation is still $\sim 80-90\%$. The SB correction succeeds to bring the measured correlation function to the same level as the MC truth. To further test out the weighting even stronger asymmetry cut of $\alpha_{\text{thres}} = 0.5$ was used. This required weighting the associated particle with $w = 0.48$. The weighted result can be seen in Figure 72 and as can be seen, the SB correlation holds also in this situation.

The sideband correction was tested also in higher p_{T} bins. These results are presented in Figure 73 for the $\alpha_{\text{thres}} = 0.8$ case, with correct weighting. The correction becomes smaller in pp collisions when looking at larger transverse momenta. This is due to the decrease of the combinatorial background when higher p_{T} bins are considered. Only the near side without the sideband correction stays distinctively different compared to the true correlation.

The expectation is that the away side would be more suppressed in the larger collision systems compared to proton-proton due to the saturation effects. Therefore the sideband method was also tested in the case of proton-lead collisions. The simulated data set was produced using PYTHIA Angantyr [141] which is a generalization of the formalism used in PYTHIA proton-proton generator to heavy ion collisions. In the simulations presented here the beam energies are set to $E_{\text{p}} = 4$ TeV for proton and $E_{\text{Pb}} = 1.57$ TeV. These energies amount to a center-of-mass energy of $\sqrt{s_{\text{NN}}} = 5.02$ TeV which corresponds to what was reached at LHC in p–Pb collisions during Run 2. In the simulation, the proton beam travels to the positive z direction which means towards FoCal.

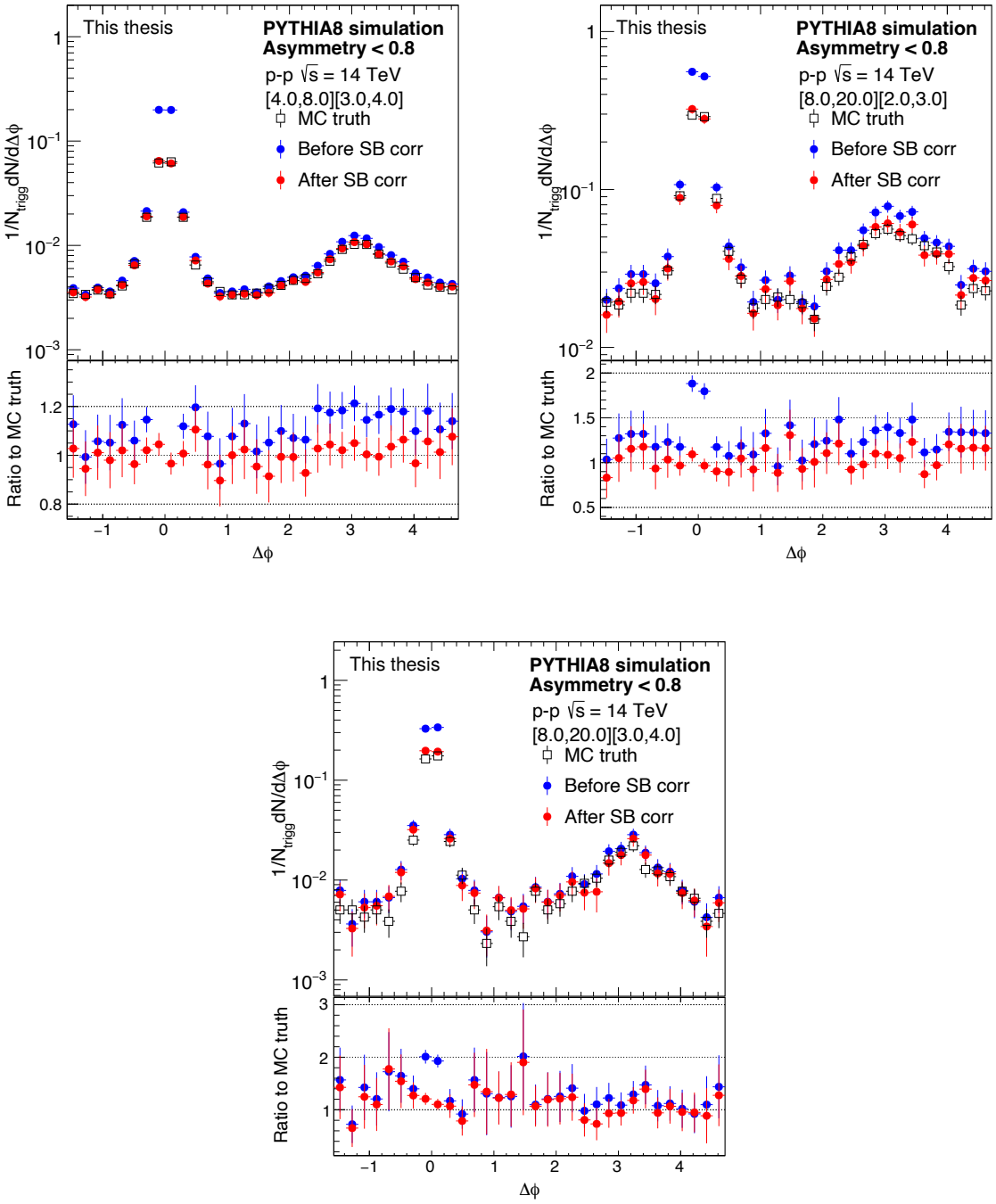

FIGURE 73 The π^0–π^0 correlation functions in higher p_{T} bins. The correlations use asymmetry cut of $\alpha_{\mathrm{thres}} = 0.8$ and therefore the associated particle is weighted with $w = 0.78$.

The results for p–Pb collisions are shown in Figure 74. The same candidate selection criteria as in pp data are used here: the mass window is $m_{\gamma\gamma} = [120, 155]$ MeV$/c^2$, the sideband is $m_{\gamma\gamma} = [50, 115] \cup [160, 200]$ MeV$/c^2$, and $\alpha_{\mathrm{thres}} = 0.8$. Similarly to the pp results the true correlation on the away side is recovered after the sideband correction. However, in pPb, the near side is still problematic even though the most optimal selections for the mass window and the sidebands are used. This indicates that in this case, the background in the sideband does not correspond to the correlated background in the mass window. The combinatorial background is larger in p–Pb compared to pp which may affect the correlation shapes. This requires a

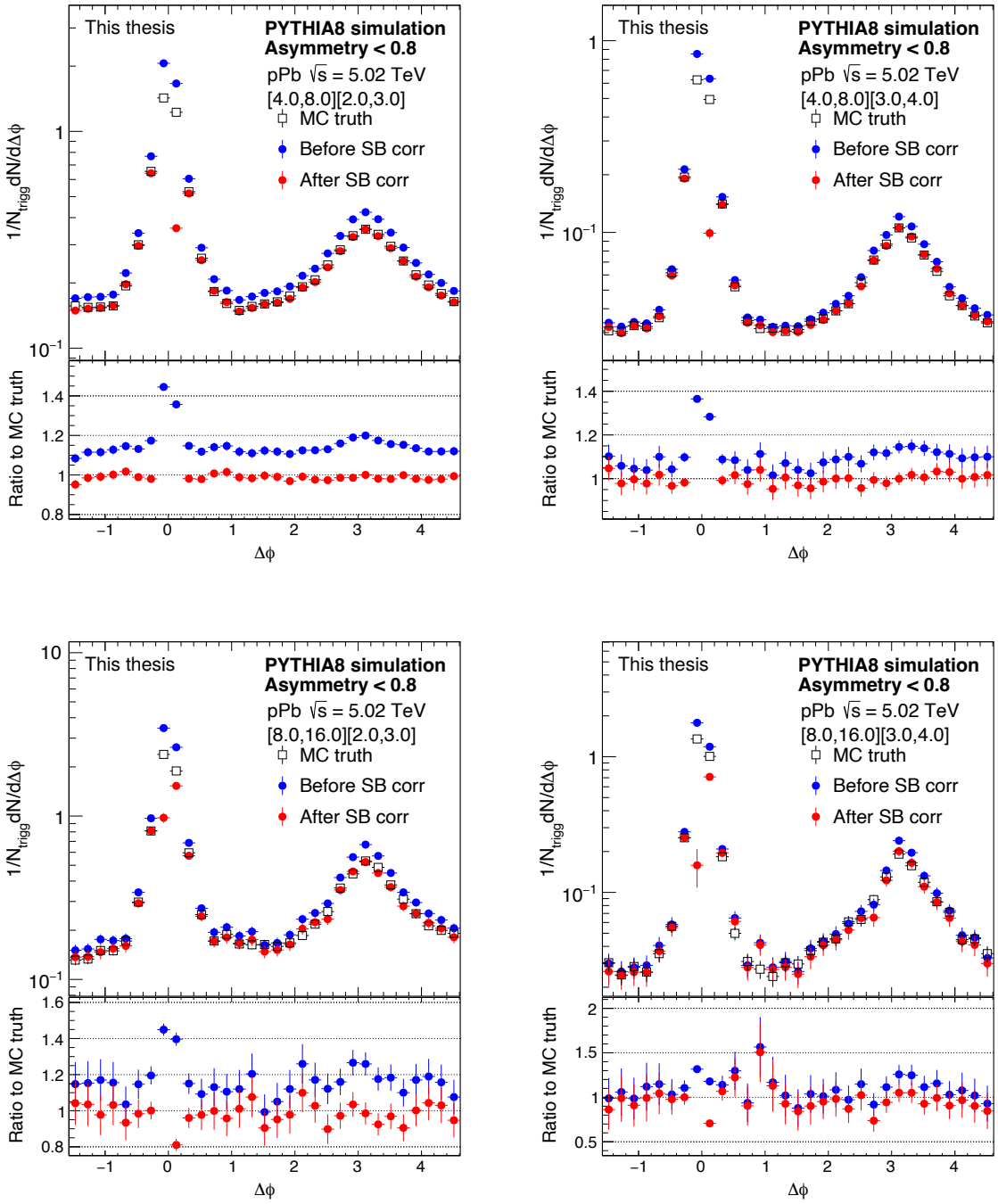

FIGURE 74 π^0–π^0 correlation function in pPb collisions before and after the sideband correction, in four different p_{T} bins.

more detailed study of the combinatorial background which is out of the scope of this thesis work. However, the correction is clearly effective on the away side. The shape on the away side before the correction is different compared to the true correlation which is evident when $p_{\mathrm{T,t}} = [4.0, 8.0]$ GeV$/c$. The correction not only brings the data to the same level as the true correlation but also corrects the shape.

5.2.4 Low mass background

Previous sections about background subtraction focused on the background at the particle level. Now we turn to PYTHIA simulations with particle transport through detector material i.e. full simulation. Figure 75 shows the mass distributions in several p_{T} bins, from full simulation using PYTHIA as the generator. The π^0 peak can be distinguished from the combinatorial background at 135 MeV$/c^2$ but the distribution also features a distinct peak at the low mass region. The extra peak can not be removed with the inclusion of asymmetry cut and therefore affects the analysis by making it challenging to take sideband contributions on the low mass side of the π^0 mass peak. The origin of a low mass peak has been previously studied by the STAR collaboration [142] and in that study, the background originated from the clusterizing algorithm dividing incorrectly one cluster to two or more clusters.

To confirm if the same applies here the low mass background was estimated in a similar manner as in the STAR analysis by generating single photons and transporting the photons through the ALICE geometry. After the clusterization, there should be only one cluster per event but if the clusters have been split into more than two they can contribute to the invariant mass distribution. Thus the invariant mass was then calculated between the clusters of each event to form the background distribution. In Figure 75 the invariant mass distributions calculated from the split clusters are plotted on top of the mass distributions calculated from PYTHIA generated events in several p_{T} bins. When scaled to match the mass distributions from PYTHIA the single photon distribution seems to describe the low mass peak rather well. A small contribution

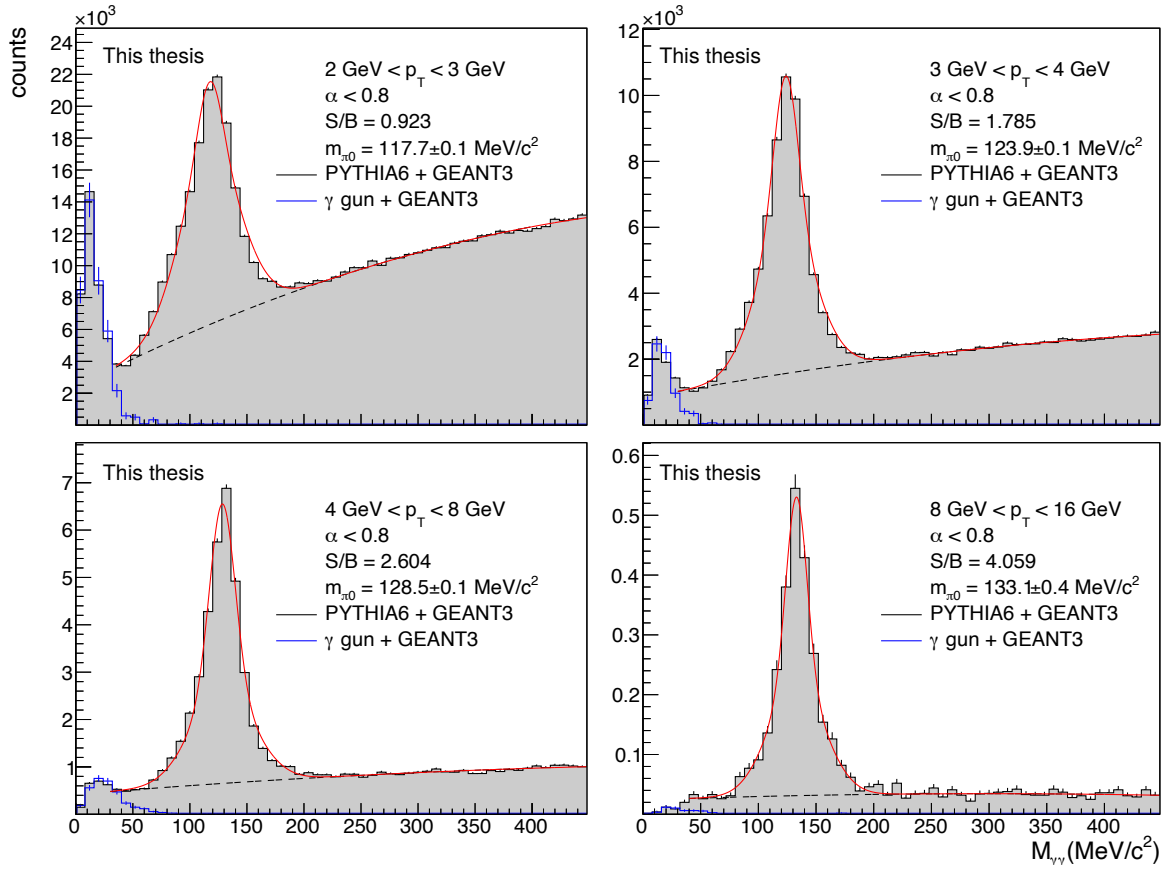

FIGURE 75 Mass distribution for clusters with $\alpha < 0.8$. The low mass background is described with normalized single photon distribution.

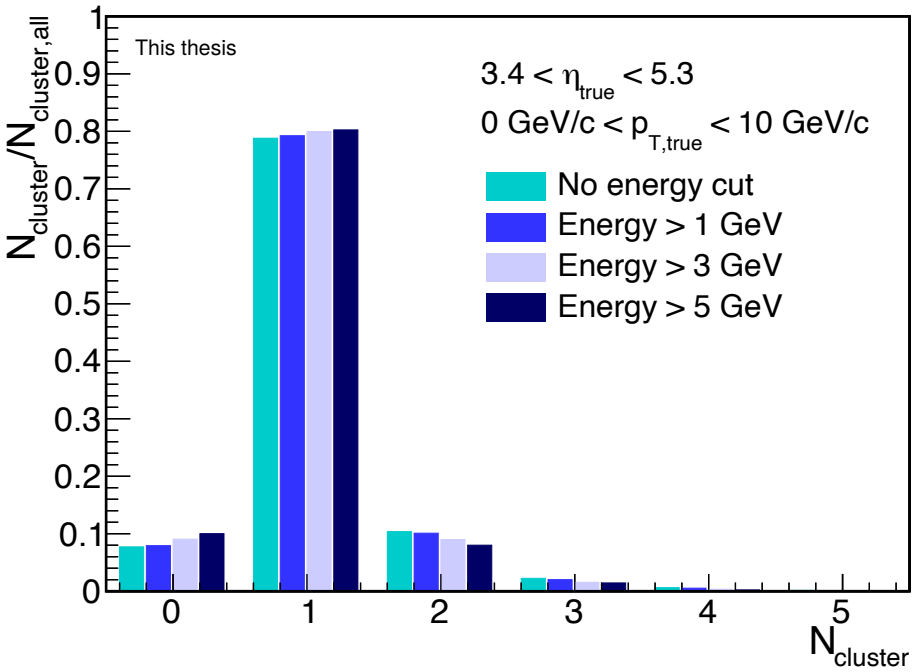

FIGURE 76 Number of clusters created by a single photon in FoCal-E.

from the split clusters can be seen in transverse momentum bin $p_{\mathrm{T}} = [4.0, 8.0]$ GeV/c but at $p_{\mathrm{T}} > 8$ GeV/c these pairs start to be insignificant.

The number of clusters produced by a photon shot to Focal acceptance can be seen in Figure 76. The number of clusters has been considered with different energy cuts but cuts used here do not affect significantly the number of split clusters. Out of all shot photons almost 80% produce only one cluster, as they ideally should. In less than 10% of the cases, the clusterizer fails to find the cluster. These missing clusters are mainly particles that hit the gaps between the FoCal-E supermodules. The probability to find two or three clusters is 10% and $1-2$% respectively. Thus the photon events in which multiple (> 3) clusters are created take up a very small fraction of all of the events. However, single particles producing more than one cluster are numerous enough to form the peak at the low mass region when the combinatorial pairs are calculated.

5.3 FoCal performance on π^0–π^0 correlation

The FoCal detector simulations are performed using particle triggered PYTHIA6 generator, combined with GEANT3 particle transport. The trigger in these simulations is a decay photon in FoCal acceptance. Another requirement is that the decay photon must have $p_{\mathrm{T}} > 2$ GeV/c, otherwise, the event is discarded at the particle level. The triggering condition and p_{T} requirement ensure that a sufficiently large simulation sample is produced in a reasonable timeframe since the particle transport is a very CPU-demanding task.

In principle, the analysis in the case of FoCal-E measured clusters follows the analysis done with PYTHIA simulated neutral pions reconstructed from energy-smeared photons. However, there are some aspects that complicate the measurement in real life. The efficiencies for π^0's reconstructed from clusters, as was shown in Section 5.1, are smaller than in the particle level

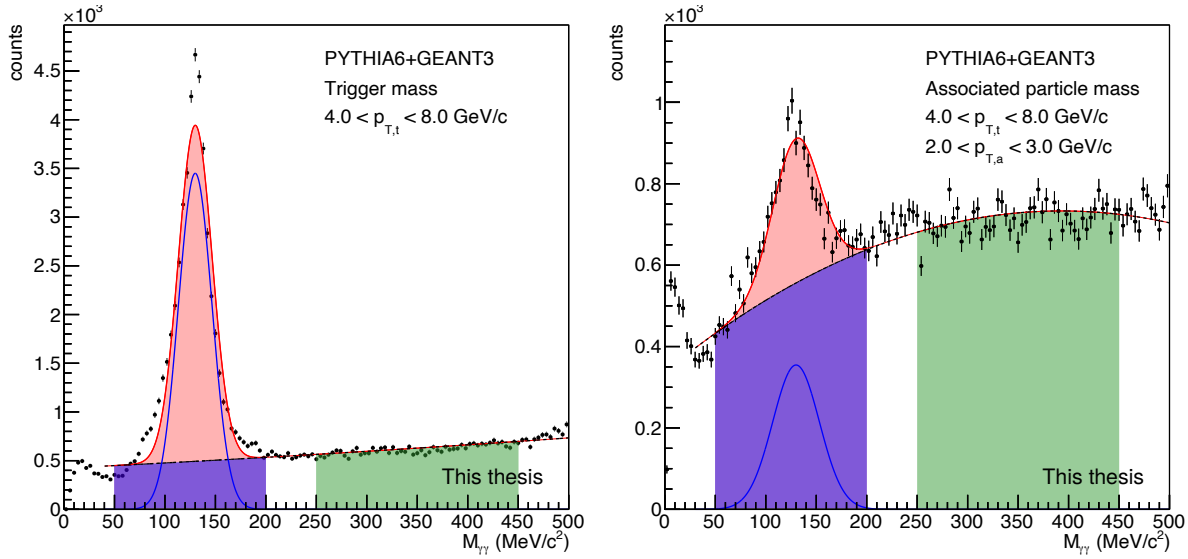

FIGURE 77 Mass distributions for trigger and associated particle calculated from FoCal-E clusters. The mass distribution is fitted with a Gaussian, combined with a polynomial to describe the background. The green area again represents the sideband used in the analysis while the mass window is divided into the π^0's (red) and background (blue).

where efficiency is nearly 100% with the optimal η cuts. The combinatorial background in invariant mass is larger in the realistic simulation, especially when a collision generator such as PYTHIA is used instead of a simple particle gun. Also, the non-physical correlations caused by the detector material and geometry should be considered in the measurement. This can be done via the mixed event method that is covered later in this section. The mixed event distributions are studied but the mixed event is not taken into account in the final correlations due to small statistics.

The invariant mass distributions for trigger and associated particles in the lowest bin are plotted in the case of detector level simulation in Figure 77. An asymmetry cut of $\alpha_{\text{thres}} = 0.8$ has been applied to the data. The associated particle mass distributions have the constraint that they depend on the trigger particle p_{T} which, combined with the lower efficiency, further cuts associated π^0 candidates. For this reason, the signal-to-background ratio is small compared to the particle level mass distributions shown previously in Figure 67. This then reflects also to the different correlation components (Equations (26)–(29)) and their relative sizes. In Figure 78 the components from particle and detector level simulations are shown side by side. The sideband components have been scaled with α, β and $\alpha\beta$ respectively, determined from the mass histograms. The sideband components at detector level are large compared to $f_{\text{mass,mass}}$ whereas, at the particle level, the sideband components are significantly smaller. Therefore when the subtraction in Equation (34) is done the detector level result is more prone to statistical fluctuations.

The final correlation after the sideband subtraction is shown in Figure 79 in four different p_{T} bins. The associated particle are weighted based on the rapidity and transverse momentum of the associated candidate, using the efficiencies calculated in Section 5.1.2. To have as many π^0 in the analysis as possible the candidates are taken from mass window $m_{\gamma\gamma} = [50, 200]$ GeV/c. The sideband is taken only from the higher mass region, in window $m_{\gamma\gamma} = [250, 450]$ GeV/c because of the width of the peak and the low mass region is dominated by the split clusters. As was demonstrated in Section 5.2.2 with this sideband selection $f_{\text{side,side}}$ does not describe

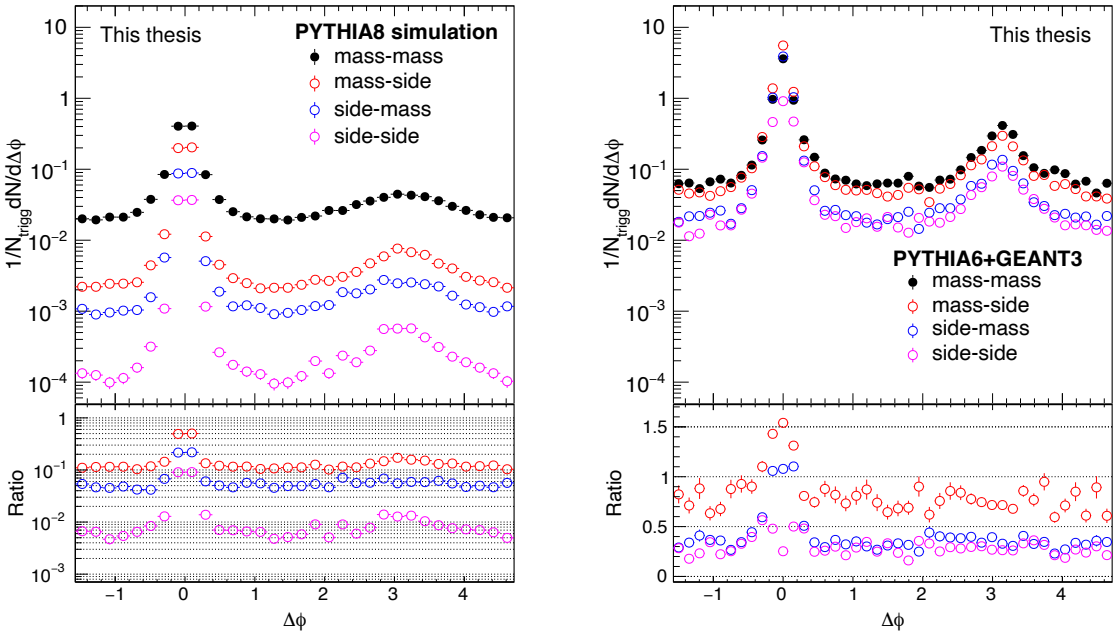

FIGURE 78 The four combinations of correlation components (Equations (26)-(29)) at particle level (left plot) and at detector level (right plot) simulations. The lower panel ratio is the ratio of a sideband component to the $f_{\text{mass,mass}}$ component.

correctly the near side background component formed from the background candidates under the mass peak. Therefore only the away side is considered in this case.

The correlation function without the sideband correction is 2–4 times as large as the Monte Carlo truth, depending on the p_{T} and $\Delta\phi$ bin in question. The sideband correction brings the correlation function to the level of Monte Carlo truth even though the errors are large, due to the lack of available statistics. The sideband corrected correlation functions with the lower associated particle p_{T} bin $[2.0, 3.0]$ GeV$/c$ show some deviation from the true correlation whereas the correlation functions with the associated particle p_{T} bin ($[3.0, 4.0]$ GeV$/c$) are quite consistent with the true correlation. The following points could affect the correlations and would need more investigation:

1. FoCal limitation at lower transverse momentum. In forward rapidities, the particle energies will get higher than at mid-rapidity. This makes it harder to study soft particles at rapidities where FoCal lies. More deviation from the true correlation is seen in the lower associated bin from 2 GeV$/c$ to 3 GeV$/c$ which could indicate that we are at the limits of what FoCal is capable of.
2. Transverse momentum reconstruction. Due to the energy losses to materials the energy of the cluster does not necessarily correspond to the true energy of the particle. This then affects also the reconstructed π^0's. This can be seen as reconstructed particles flowing from higher p_{T} values to lower ones. Because the correlation functions are measured in p_{T} bins some amount of the π^0 are placed in the wrong bin. The efficiency, being defined as a function of p_{T} can correct this effect to some extent but the problem might be approached with unfolding. However, unfolding the p_{T} is beyond the scope of this thesis.

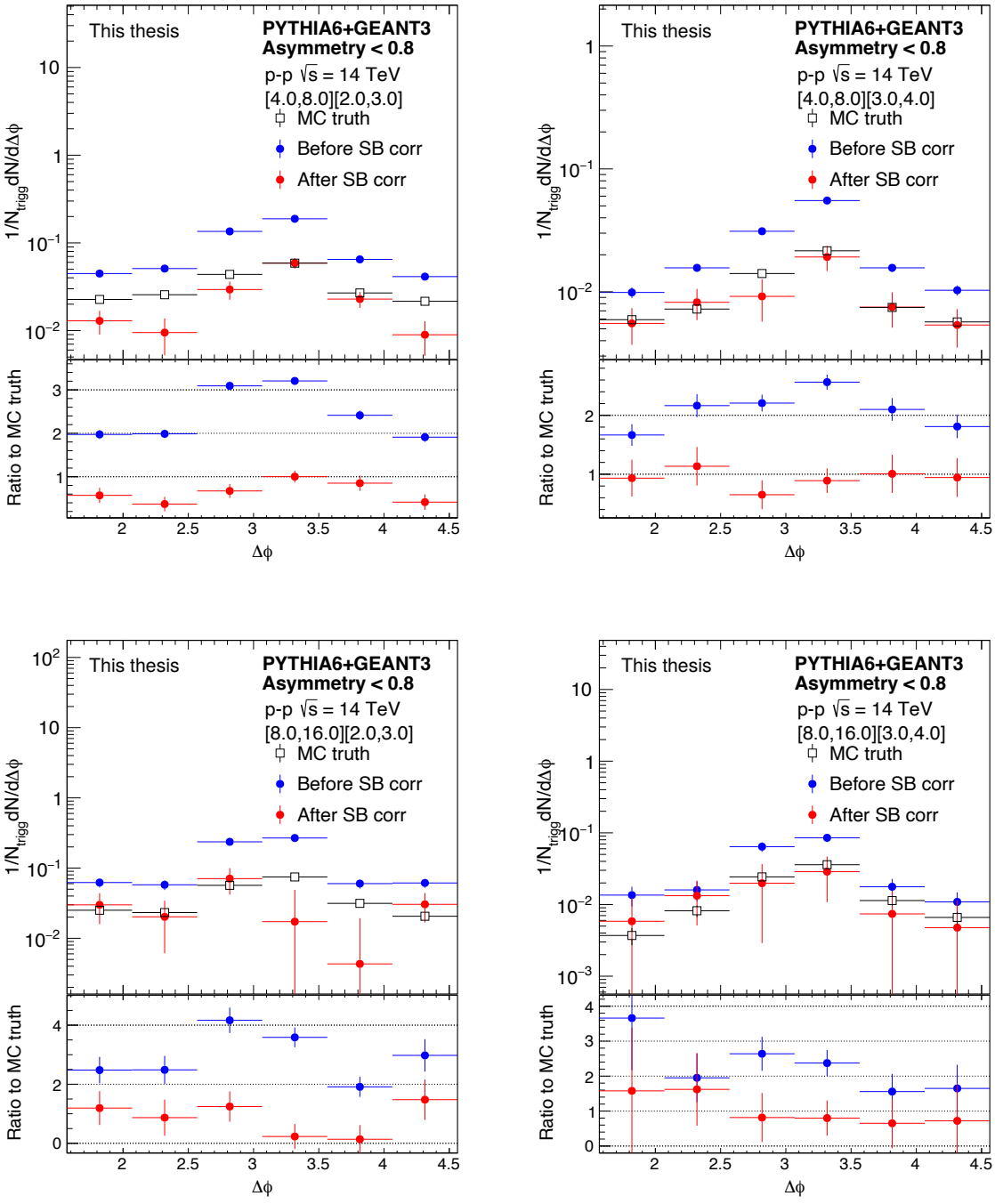

FIGURE 79 The away side of π^0–π^0correlation in four different p_{T} bins, calculated from clusters reconstructed in FoCal-E.

3. The correlations due to the material. The correlations that are caused by the detector material have similar structures event-by-event. As explained in Section 5.1.3, these correlations can be taken into account by constructing the mixed event correlation. In this analysis, the mixed event is not taken into account in the results presented in this section due to insufficient statistics. However, the mixed event distribution was studied to get an idea of how it should be implemented in the full analysis chain.

   To construct the mixed event the associated particles from previous events are saved to a pool and are mixed with the triggers of the current event. In the case of π^0–π^0 correlations events with two π^0's in forward rapidity are somewhat rare and for that reason, the pool size needs to be large enough for reasonable statistics. It would be ideal to use as many of the previous events as possible but a larger pool demands more CPU time. In this simulation study, the pool size is selected to be 100 events.

   The projections of the mixed event to $\Delta\phi$ and $\Delta\eta$ in one p_{T} bin are shown in Figure 80. The distribution is calculated for each correlation component (Equations (26)–(29)). On average the mixed event is constant in $\Delta\phi$, having deviations of approximately $\pm 6-7\%$. The $\Delta\eta$ however is more asymmetric in relation to $\Delta\eta = 0$. It can also be noted that the different components are quite different compared to each other. This suggests that each component should be divided with the mixed event individually, instead of doing the correction only to the sideband corrected results.

Regardless, the simulations demonstrate that both the yield and correlation shape in these kinematics need a correction which in this study is applied via the sideband method. Even though the points listed above are not considered here the sideband method can be used to recover the true correlation with certain limitations. Due to the width of the π^0 peak, as explained previously in this chapter, the sideband correction can most likely to be applied to the away side only. However, for the gluon saturation physics the away side is the crucial correlation to measure.

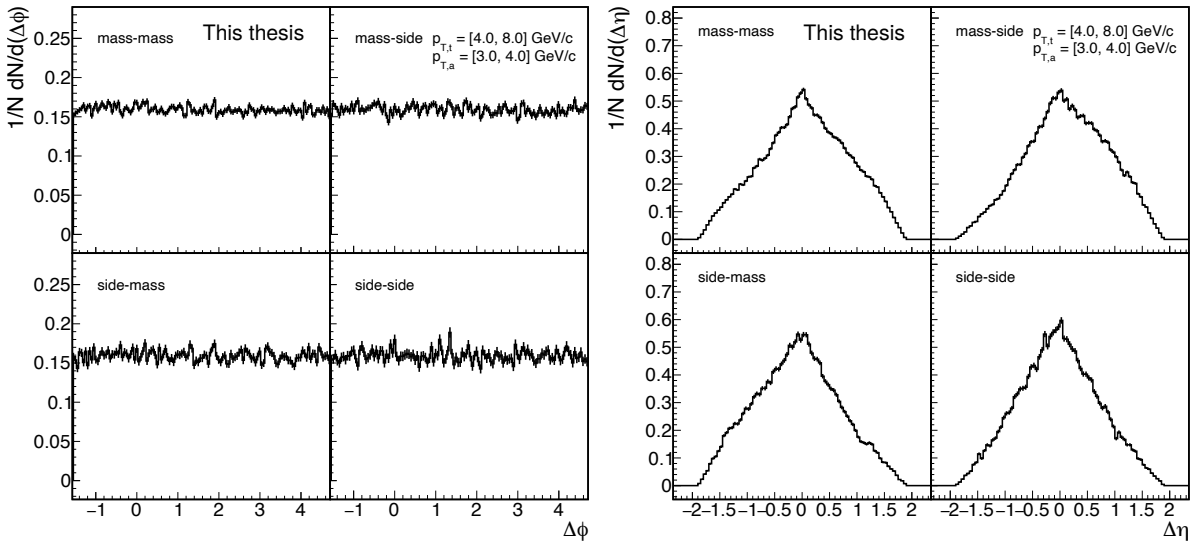

FIGURE 80 Projections of the 2D mixed correlations for all measured correlation components in one p_{T} bin. The left side shows the $\Delta\phi$ projection whereas $\Delta\eta$ projection is on the right side.

6 SUMMARY

In this thesis performance of ALICE forward detectors FIT and FoCal were studied. In the case of FIT, investigating the event plane resolution of FV0, FT0-A and FT0-C via simulations of AMPT-generated events transported through the ALICE Run 3 geometry. FoCal, being a future upgrade to the ALICE setup was tested during 2021 and 2022 and results regarding the analysis of the pad sensors of the electromagnetic calorimeter were presented here. FoCal performance to π^0–π^0 correlations, an observable sensitive to gluon saturation was estimated through simulations.

π^0–π^0 correlation was introduced as one of the physical observables that can be investigated with FoCal. The theoretical models predict suppression on the away side due to the gluon saturation. However, since π^0 needs to be reconstructed from its decay products, we are not considering a two-particle correlation but technically a four-particle correlation. This introduces correlated background to the measurement. The background was estimated via PYTHIA 8 simulations and a method utilizing sidebands from the invariant mass distribution was developed to deal with it. With the correct weighting the method was proven to recover the true π^0–π^0 correlation correctly in the case of proton-proton collisions. In addition to proton-proton, the sideband method was tested in proton-lead collisions. In that case, the method works well on the away side but the near side is not completely recovered.

The method was then tested in a more realistic simulation in which the particle transportation through ALICE setup, FoCal included was performed. These simulations demonstrated that at these energies also the away side peak is different to the Monte Carlo truth, not only in yield but also in shape. Therefore sideband correction is needed for retrieving the true correlation. In the realistic case, the background on the near side is hard to fully be removed but the genuine away side yield and shape are close to the MC truth after the sideband correction. The π^0–π^0 correlation measurement published by the STAR Collaboration shows relative quantities but no actual yields. The need for the sideband correction in FoCal kinematics is evident and these results raise the question if such corrections are needed also at RHIC energies for the absolute yields. π^0–π^0 correlation is part of the FoCal physics goals and therefore this study was important to estimate the performance for said observable.

In addition to the correlation results the FoCal test beam analysis gives an extensive overview of the characteristics of the pad sensor. The results give insights into the full FoCal-E performance from the standpoint of readout parameter selection, bias voltage etc. Clear MIP signals were able to be measured with the tested sensors and a crude estimation was given to the energy resolution at low electron energies. The resolution measurement suffered from issues with data acquisition and calibration. Since the two test beams presented in this work, there have been two additional tests in which the common triggering between FoCal subsystems was successfully tested. For the pad layers, smaller noise levels have been measured and ADC and ToT linearity has been investigated more. While writing this there will be three more test beams planned for 2023.

BIBLIOGRAPHY

1. ATLAS Collaboration. Observation of a new particle in the search for the Standard Model Higgs boson with the ATLAS detector at the LHC. *Physics Letters B* **716,** 1–29 (Sept. 2012).
2. CMS Collaboration. Observation of a new boson at a mass of 125 GeV with the CMS experiment at the LHC. *Physics Letters B* **716,** 30–61 (Sept. 2012).
3. Nayak, T. & Sinhah, B. *Search and Study of Quark-gluon Plasma at the CERN-LHC* in *Physics at the Large Hadron Collider* 131–144 (Springer India, 2009).
4. Greenberg, O. W. Spin and Unitary-Spin Independence in a Paraquark Model of Baryons and Mesons. *Physical Review Letters* **13,** 598–602 (Nov. 1964).
5. Bartoli, B. *et al.* Electron-Positron Interactions at High Energies. *Physical Review D* **6,** 2374–2404 (1972).
6. Bell, J. S. & Jackiw, R. W. A PCAC puzzle: $\pi^0 \to \gamma\gamma$ in the σ-model. *Nuovo Cimento* **60,** 47–61 (1969).
7. Adler, S. L. Axial-Vector Vertex in Spinor Electrodynamics. *Physical Review* **177,** 2426–2438 (1969).
8. Brock, R. *et al.* Handbook of perturbative QCD: Version 1.0. *Reviews of Modern Physics* **67,** 157–248 (1995).
9. Gupta, R. *Introduction to lattice QCD: Course* in *Les Houches Summer School in Theoretical Physics, Session 68: Probing the Standard Model of Particle Interactions* (July 1997), 83–219. arXiv: hep-lat/9807028.
10. Karsch, F., Laermann, E. & Peikert, A. Quark mass and flavour dependence of the QCD phase transition. *Nuclear Physics B* **605,** 579–599 (July 2001).
11. Weber, F. Quark matter in neutron stars. *Journal of Physics G: Nuclear and Particle Physics* **25,** R195 (Sept. 1999).
12. Annala, E., Gorda, T., Kurkela, A., Nättilä, J. & Vuorinen, A. Evidence for quark-matter cores in massive neutron stars. *Nature Physics* **16,** 907–910 (June 2020).
13. Odyniec, G. The RHIC Beam Energy Scan program in STAR and what's next ... *Journal of Physics: Conference Series* **455,** 012037 (Aug. 2013).
14. Senger, P. Astrophysics in the Laboratory—The CBM Experiment at FAIR. *Particles* **3,** 320–335 (Apr. 2020).
15. Chaudhuri, A. K. Viscous Hydrodynamic Model for Relativistic Heavy Ion Collisions. *Advances in High Energy Physics* **2013,** 693180 (2013).
16. Cooper, F. & Frye, G. Single-particle distribution in the hydrodynamic and statistical thermodynamic models of multiparticle production. *Physical Review D* **10,** 186–189 (July 1974).
17. Poskanzer, A. M. & Voloshin, S. A. Methods for analyzing anisotropic flow in relativistic nuclear collisions. *Physical Review C* **58,** 1671–1678 (Sept. 1998).

18. ALICE Collaboration. Higher Harmonic Anisotropic Flow Measurements of Charged Particles in Pb-Pb Collisions at 2.76 TeV. *Physical Review Letters* **107,** 032301 (July 2011).
19. Niemi, H., Denicol, G. S., Holopainen, H. & Huovinen, P. Event-by-event distributions of azimuthal asymmetries in ultrarelativistic heavy-ion collisions. *Physical Review C* **87,** 054901 (May 2013).
20. ALICE Collaboration. Higher harmonic non-linear flow modes of charged hadrons in Pb-Pb collisions at $\sqrt{s_{\mathrm{NN}}} = 5.02$ TeV. *Journal of High Energy Physics* **2020,** 85 (2020).
21. STAR Collaboration. Anisotropic Flow at RHIC. *Acta Physica Hungarica* **24,** 209–214 (Oct. 2005).
22. ALICE Collaboration. Anisotropic Flow of Charged Particles in Pb-Pb Collisions at $\sqrt{s_{\mathrm{NN}}} = 5.02$ TeV. *Physical Review Letters* **116,** 132302 (Apr. 2016).
23. Heinz, U. & Snellings, R. Collective Flow and Viscosity in Relativistic Heavy-Ion Collisions. *Annual Review of Nuclear and Particle Science* **63,** 123–151. eprint: https://doi.org/10.1146/annurev-nucl-102212-170540 (2013).
24. Bernhard, J. E., Moreland, J. S. & Bass, S. A. Bayesian estimation of the specific shear and bulk viscosity of quark–gluon plasma. *Nature Physics* **15,** 1113–1117 (2019).
25. Schenke, B., Jeon, S. & Gale, C. Higher flow harmonics from $(3+1)$D event-by-event viscous hydrodynamics. *Physical Review C* **85,** 024901 (Feb. 2012).
26. Parkkila, J. E., Onnerstad, A. & Kim, D. J. Bayesian estimation of the specific shear and bulk viscosity of the quark-gluon plasma with additional flow harmonic observables. *Physical Review C* **104,** 054904 (Nov. 2021).
27. ALICE Collaboration. The ALICE experiment – A journey through QCD (2022).
28. ATLAS Collaboration. Measurement of the jet radius and transverse momentum dependence of inclusive jet suppression in lead-lead collisions at $\sqrt{s_{\mathrm{NN}}} = 2.76$ TeV with the ATLAS detector. *Physics Letters B* **719,** 220–241 (2013).
29. PHENIX Collaboration. Suppressed π^0 Production at Large Transverse Momentum in Central Au+Au Collisions at $\sqrt{s_{\mathrm{NN}}} = 200$ GeV. *Physical Review Letters* **91,** 072301 (Aug. 2003).
30. STAR Collaboration. Transverse-Momentum and Collision-Energy Dependence of High-p_{T} Hadron Suppression in Au+Au Collisions at Ultrarelativistic Energies. *Physical Review Letters* **91,** 172302 (Oct. 2003).
31. CMS Collaboration. The production of isolated photons in PbPb and pp collisions at $\sqrt{s_{\mathrm{NN}}}$ = 5.02 TeV. *Journal of High Energy Physics* **2020,** 116 (July 2020).
32. ALICE Collaboration. Azimuthal anisotropy of charged jet production in $\sqrt{s_{\mathrm{NN}}} = 2.26$TeV Pb–Pb collisions. *Physics Letters B* **753,** 511–525 (Feb. 2016).
33. Gardim, F. G., Grassi, F., Luzum, M. & Ollitrault, J.-Y. Mapping the hydrodynamic response to the initial geometry in heavy-ion collisions. *Physical Review C* **85,** 024908 (Feb. 2012).
34. d'Enterria, D. & Loizides, C. Progress in the Glauber Model at Collider Energies. *Annual Review of Nuclear and Particle Science* **71,** 315–344. eprint: https://doi.org/10.1146/annurev-nucl-102419-060007 (2021).

35. Drescher, H.-J. & Nara, Y. Effects of fluctuations on the initial eccentricity from the color glass condensate in heavy ion collisions. *Physical Review C* **75,** 034905 (Mar. 2007).

36. Gelis, F., Iancu, E., Jalilian-Marian, J. & Venugopalan, R. The Color Glass Condensate. *Annual Review of Nuclear and Particle Science* **60,** 463–489. eprint: https://doi.org/10.1146/annurev.nucl.010909.083629 (2010).

37. Bartels, J., Golec-Biernat, K. & Kowalski, H. Modification of the saturation model: Dokshitzer-Gribov-Lipatov-Altarelli-Parisi evolution. *Physical Review D* **66,** 014001 (2002).

38. Schenke, B., Tribedy, P. & Venugopalan, R. Fluctuating Glasma Initial Conditions and Flow in Heavy Ion Collisions. *Physical Review Letters* **108,** 252301 (June 2012).

39. Esumi, S. Collective Flow Measurements from the PHENIX Experiment. *Journal of Physics G* **38,** 124010. arXiv: 1110.3223 [nucl-ex] (2011).

40. Soper, D. E. Parton distribution functions. *Nuclear Physics B - Proceedings Supplements* **53,** 69–80 (Feb. 1997).

41. Pumplin, J. *et al.* New Generation of Parton Distributions with Uncertainties from Global QCD Analysis. *Journal of High Energy Physics* **2002,** 012 (July 2002).

42. Lipatov, L. N. The parton model and perturbation theory. *Soviet Journal of Nuclear Physics* **20,** 94–102 (1975).

43. Salam, G. P. An Introduction to leading and next-to-leading BFKL. *Acta Physica Polonica B* **30,** 3679–3705. arXiv: hep-ph/9910492 (1999).

44. Balitsky, I. Operator expansion for high-energy scattering. *Nuclear Physics B* **463,** 99–157 (Mar. 1996).

45. Kovchegov, Y. V. Small-x F_2 Structure Function of a Nucleus Including Multiple Pomeron Exchanges. *Physical Review D* **60,** 034008 (June 1999).

46. ALICE Collaboration. *Letter of Intent: A Forward Calorimeter (FoCal) in the ALICE experiment* tech. rep. (CERN, Geneva, June 2020).

47. Kovchegov, Y. Brief Review of Saturation Physics. *Acta Physica Polonica B* **45,** 2241 (2014).

48. Abdul Khalek, R. *et al.* Snowmass 2021 White Paper: Electron Ion Collider for High Energy Physics (2022).

49. ALICE Collaboration. The ALICE experiment at the CERN LHC. *Journal of Instrumentation* **3,** S08002 (Aug. 2008).

50. ATLAS Collaboration. The ATLAS Experiment at the CERN Large Hadron Collider. *Journal of Instrumentation* **3,** S08003 (Aug. 2008).

51. CMS Collaboration. The CMS experiment at the CERN LHC. The Compact Muon Solenoid experiment. *Journal of Instrumentation* **3,** S08004 (2008).

52. LHCb Collaboration. The LHCb Detector at the LHC. *Journal of Instrumentation* **3,** S08005 (2008).

53. ALICE Collaboration. *Letter of Intent for A Large Ion Collider Experiment [ALICE]* tech. rep. (CERN, Geneva, 1993).

54. Adams, J. *et al.* Experimental and theoretical challenges in the search for the quark-gluon plasma: The STAR Collaboration's critical assessment of the evidence from RHIC collisions. *Nuclear Physics A* **757,** 102–183 (Aug. 2005).

55. Adcox, K. *et al.* Formation of dense partonic matter in relativistic nucleus–nucleus collisions at RHIC: Experimental evaluation by the PHENIX Collaboration. *Nuclear Physics A* **757,** 184–283 (Aug. 2005).

56. ALICE Collaboration. *ALICE Electromagnetic Calorimeter Technical Design Report* tech. rep. (2008).

57. Heinz, U. & Jacob, M. *Evidence for a New State of Matter: An Assessment of the Results from the CERN Lead Beam Programme* 2000. arXiv: nucl-th/0002042 [nucl-th].

58. Arsene, I. *et al.* Quark–gluon plasma and color glass condensate at RHIC? The perspective from the BRAHMS experiment. *Nuclear Physics A* **757,** 1–27 (Aug. 2005).

59. Back, B. *et al.* The PHOBOS perspective on discoveries at RHIC. *Nuclear Physics A* **757,** 28–101 (2005).

60. ALICE Collaboration. *ALICE upgrades during the LHC Long Shutdown 2* 2023. arXiv: 2302.01238.

61. ALICE Collaboration. *Upgrade of the ALICE Experiment: Letter of Intent* tech. rep. (CERN, Geneva, Aug. 2012).

62. Antonioli, P., Kluge, A. & Riegler, W. *Upgrade of the ALICE Readout & Trigger System* tech. rep. (2013).

63. Buncic, P., Krzewicki, M. & Vyvre, P. V. *Technical Design Report for the Upgrade of the Online-Offline Computing System* tech. rep. (2015).

64. Richter, M. A design study for the upgraded ALICE O^2 computing facility. *Journal of Physics: Conference Series* **664,** 082046 (2015).

65. ALICE Collaboration. *Technical Design Report for the Upgrade of the ALICE Inner Tracking System* tech. rep. (2014).

66. *Upgrade of the ALICE Time Projection Chamber* tech. rep. (2013).

67. Mager, M. ALPIDE, the Monolithic Active Pixel Sensor for the ALICE ITS upgrade. *Nuclear Instruments and Methods in Physics Research Section A: Accelerators, Spectrometers, Detectors and Associated Equipment* **824.** Frontier Detectors for Frontier Physics: Proceedings of the 13th Pisa Meeting on Advanced Detectors, 434–438 (2016).

68. Sauli, F. GEM: A new concept for electron amplification in gas detectors. *Nuclear Instruments and Methods in Physics Research Section A: Accelerators, Spectrometers, Detectors and Associated Equipment* **386,** 531–534 (1997).

69. Colella, D. ALICE ITS Upgrade for LHC Run 3: Commissioning in the Laboratory. *Journal of Physics: Conference Series* **2374,** 012058 (2020).

70. ALICE Collaboration. *Technical Design Report for the Muon Forward Tracker* tech. rep. (2015).

71. Uras, A. & the ALICE MFT Working Group. Muon Physics in ALICE: The MFT Upgrade Project. *Journal of Physics: Conference Series* **446,** 012054 (Sept. 2013).

72. ALICE collaboration. Performance of the ALICE VZERO system. *Journal of Instrumentation* **8,** P10016 (Oct. 2013).

73. Broz, M. *et al.* Performance of ALICE AD modules in the CERN PS test beam. *Journal of Instrumentation* **16,** P01017. arXiv: 2006.14982 (2021).

74. Grigoriev, V. *et al.* ALICE T0 detector. *IEEE Transactions on Nuclear Science - IEEE TRANS NUCL SCI* **52,** 605–608 Vol. 1 (Nov. 2004).

75. Rojas, S. The Forward Diffractive Detector for ALICE. *PoS* **LHCP2020,** 221 (2021).

76. Slupecki, M. *The Fast Interaction Trigger for the ALICE Upgrade* PhD thesis (University of Jyväskylä, 2020).

77. ALICE Collaboration. Measurement of inelastic, single- and double-diffraction cross sections in proton–proton collisions at the LHC with ALICE. *The European Physical Journal C* **73,** 2456 (June 2013).

78. Schmidt, B. The High-Luminosity upgrade of the LHC: Physics and Technology Challenges for the Accelerator and the Experiments. *Journal of Physics: Conference Series* **706,** 022002 (Apr. 2016).

79. ALICE Collaboration. *Letter of intent for ALICE 3: A next generation heavy-ion experiment at the LHC* tech. rep. (CERN, Geneva, Mar. 2022).

80. Musa, L. *Letter of Intent for an ALICE ITS Upgrade in LS3* tech. rep. (CERN, Geneva, Dec. 2019).

81. Fabjan, C. W. *et al.* ALICE: Physics Performance Report. *Journal of Physics G* **32,** 1295–2040 (2006).

82. Helenius, I., Eskola, K. J. & Paukkunen, H. Probing the small-x nuclear gluon distributions with isolated photons at forward rapidities in p+Pb collisions at the LHC. *Journal of High Energy Physics* **2014,** 138 (Sept. 2014).

83. Ducloué, B., Lappi, T. & Mäntysaari, H. Isolated photon production in proton-nucleus collisions at forward rapidity. *Physical Review D* **97,** 054023 (Mar. 2018).

84. Kusina, A., Lansberg, J.-P., Schienbein, I. & Shao, H.-S. Gluon Shadowing in Heavy-Flavor Production at the LHC. *Physical Review Letters* **121,** 052004 (Aug. 2018).

85. Eskola, K. J., Paakkinen, P., Paukkunen, H. & Salgado, C. A. EPPS21: a global QCD analysis of nuclear PDFs. *The European Physical Journal C* **82,** 413 (May 2022).

86. Aaij, R. *et al.* Study of prompt D^0 meson production in pPb collisions at $\sqrt{s} = 5$ TeV. *Journal of High Energy Physics* **2017,** 90 (Oct. 2017).

87. Khalek, R. A. *et al.* NNNPDF3.0: Evidence for a modified partonic structure in heavy nuclei. *The European Physical Journal C* **82,** 507. arXiv: 2201.12363 [hep-ph] (2022).

88. Kusina, A. *et al.* Vector boson production in pPb and PbPb collisions at the LHC and its impact on nCTEQ15 PDFs. *The European Physical Journal C* **77** (2017).

89. Khalek, R. A., Ethier, J. J., Rojo, J. & van Weelden, G. nNNPDF2.0: quark flavor separation in nuclei from LHC data. *Journal of High Energy Physics* **2020,** 183 (Sept. 2020).

90. ALICE Collaboration. Coherent J/ψ photoproduction at forward rapidity in ultra-peripheral Pb–Pb collisions at 5.02 TeV. *Physics Letters B* **798,** 134926 (Nov. 2019).

91. Ryskin, M. G. Diffractive J / psi electroproduction in LLA QCD. *Zeitschrift für Physik C Particles and Fields* **57,** 89–92 (1993).

92. Eskola, K. J., Flett, C. A., Guzey, V., Löytäinen, T. & Paukkunen, H. *Next-to-leading order QCD predictions for exclusive J/ψ photoproduction in ultraperipheral Pb+Pb collisions at the LHC* in *Proceedings of the XXIX International Workshop on Deep-Inelastic Scattering and Related Subjects* (2022). arXiv: 2208.06806 [hep-ph].

93. Stasto, A., Wei, S.-Y., Xiao, B.-W. & Yuan, F. On the dihadron angular correlations in forward pA collisions. *Physics Letters B* **784,** 301–306 (Sept. 2018).

94. Marquet, C. Forward inclusive dijet production and azimuthal correlations in pA collisions. *Nuclear Physics A* **796,** 41–60 (Nov. 2007).

95. ALICE Collaboration. Long-range angular correlations on the near and away side in p-Pb collisions at $\sqrt{s_{\rm NN}} = 5.02$ TeV. *Physics Letters B* **719,** 29–41 (2013).

96. STAR Collaboration. Evidence for Nonlinear Gluon Effects in QCD and Their Mass Number Dependence at STAR. *Physical Review Letters* **129,** 092501 (Aug. 2022).

97. Miller, M. L., Reygers, K., Sanders, S. J. & Steinberg, P. Glauber Modeling in High-Energy Nuclear Collisions. *Annual Review of Nuclear and Particle Science* **57,** 205–243 (Nov. 2007).

98. Abelev, B. *et al.* Centrality determination of Pb-Pb collisions at $\sqrt{s_{NN}} = 2.76$ TeV with ALICE. *Physical Review C* **88,** 044909 (Oct. 2013).

99. ALICE Collaboration. Centrality Dependence of the Charged-Particle Multiplicity Density at Midrapidity in Pb-Pb Collisions at $\sqrt{s_{NN}} = 5.02$ TeV. *Physical Review Lett.* **116,** 222302 (June 2016).

100. Luzum, M. & Ollitrault, J.-Y. Eliminating experimental bias in anisotropic-flow measurements of high-energy nuclear collisions. *Physical Review C* **87,** 044907 (Apr. 2013).

101. Borghini, N., Dinh, P. M. & Ollitrault, J.-Y. New method for measuring azimuthal distributions in nucleus-nucleus collisions. *Physical Review C* **63,** 054906 (Apr. 2001).

102. Agakishiev, H. *et al.* Event-plane-dependent dihadron correlations with harmonic subtraction v_n in Au+Au collisions at $\sqrt{s_{\rm NN}} = 200$ GeV. *Physical Review C* **89,** 041901 (Apr. 2014).

103. ALICE Collaboration. Jet-hadron correlations measured relative to the second order event plane in Pb-Pb collisions at $\sqrt{s_{NN}} = 2.76$ TeV. *Physical Review C* **101,** 064901 (June 2020).

104. ALICE Collaboration. Pseudorapidity dependence of the anisotropic flow of charged particles in Pb–Pb collisions at $\sqrt{s_{\rm NN}} = 2.76$ TeV. *Physics Letters B* **762,** 376–388 (2016).

105. PHENIX Collaboration. Pseudorapidity Dependence of Particle Production and Elliptic Flow in Asymmetric Nuclear Collisions of $p+$Al, $p+$Au, $d+$Au, and ^{3}He $+$ Au at $\sqrt{s_{NN}} = 200$ GeV. *Physical Review Lett.* **121,** 222301 (Nov. 2018).

106. Selyuzhenkov, I. & Voloshin, S. Effects of nonuniform acceptance in anisotropic flow measurements. *Physical Review C* **77,** 034904 (Mar. 2008).

107. Lin, Z.-W., Ko, C. M., Li, B.-A., Zhang, B. & Pal, S. Multiphase transport model for relativistic heavy ion collisions. *Physical Review C* **72,** 064901 (Dec. 2005).

108. Wang, X.-N. & Gyulassy, M. HIJING: A Monte Carlo model for multiple jet production in pp, pA and AA collisions. *Physical Review D* **44,** 3501–3516 (1991).

109. Zhang, B. ZPC 1.0.1: a parton cascade for ultrarelativistic heavy ion collisions. *Computer Physics Communications* **109,** 193–206 (1998).

110. Andersson, B., Gustafson, G., Ingelman, G. & Sjöstrand, T. Parton Fragmentation and String Dynamics. *Physics Reports* **97,** 31–145 (1983).

111. Fries, R., Greco, V. & Sorensen, P. Coalescence Models for Hadron Formation from Quark-Gluon Plasma. *Annual Review of Nuclear and Particle Science* **58,** 177–205 (Nov. 2008).

112. Li, B.-A. & Ko, C. M. Formation of superdense hadronic matter in high energy heavy-ion collisions. *Physical Review C* **52,** 2037–2063 (Oct. 1995).

113. Ma, G.-L. & Lin, Z.-W. Predictions for $\sqrt{s_{NN}} = 5.02$ TeV Pb + Pb collisions from a multiphase transport model. *Physical Review C* **93,** 054911 (May 2016).

114. Feng, Z., Huang, G.-M. & Liu, F. Anisotropic flow of Pb+Pb from a multi-phase transport model. *Chinese Physics C* **41,** 024001 (Feb. 2017).

115. Loizides, C., Kamin, J. & d'Enterria, D. Improved Monte Carlo Glauber predictions at present and future nuclear colliders. *Physical Review C* **97,** 054910 (May 2018).

116. Agostinelli, S. *et al.* Geant4—a simulation toolkit. *Nuclear Instruments and Methods in Physics Research Section A: Accelerators, Spectrometers, Detectors and Associated Equipment* **506,** 250–303 (2003).

117. Fabjan, C. W. & Gianotti, F. Calorimetry for Particle Physics. *Reviews of Modern Physics* **75,** 1243–1286 (2003).

118. Fukuda, S. *et al.* The Super-Kamiokande detector. *Nuclear Instruments and Methods in Physics Research Section A: Accelerators, Spectrometers, Detectors and Associated Equipment* **501,** 418–462 (2003).

119. CMS Collaboration. *The CMS electromagnetic calorimeter project: Technical Design Report* (CERN, Geneva, 1997).

120. CMS Collaboration. Particle-flow reconstruction and global event description with the CMS detector. *Journal of Instrumentation* **12,** P10003 (2017).

121. Yao, W.-M. *et al.,* (Particle Data Group). Review of Particle Physics. *Journal of Physics G* **33,** 1 (2006).

122. Leo, W. *Techniques for Nuclear and Particle Physics Experiments: A How-to Approach* 2nd ed. (Springer-Verlag Berlin Heidelberg GmbH, 1994).

123. Landau, L. D. On the energy loss of fast particles by ionization. *Journal of Physics* **8,** 201–205 (1944).

124. Ochando, C. & on behalf of the CMS Collaboration. HGCAL: A High-Granularity Calorimeter for the Endcaps of CMS at HL-LHC. *Journal of Physics: Conference Series* **928,** 012025 (Nov. 2017).

125. Blau, D. Performance of the ALICE electromagnetic calorimeters in LHC Runs 1 and 2 and upgrade projects. *Journal of Instrumentation* **15,** C03025–C03025 (Mar. 2020).

126. Aharrouche, M. *et al.* Energy linearity and resolution of the ATLAS electromagnetic barrel calorimeter in an electron test-beam. *Nuclear Instruments and Methods in Physics Research Section A: Accelerators, Spectrometers, Detectors and Associated Equipment* **568,** 601–623 (2006).

127. Aphecetche, L *et al.* PHENIX calorimeter. *Nuclear Instruments and Methods in Physics Research Section A: Accelerators, Spectrometers, Detectors and Associated Equipment* **499,** 521–536 (2003).

128. Bombardi, G. *et al. HGCROC-Si and HGCROC-SiPM: the front-end readout ASICs for the CMS HGCAL* in *2020 IEEE Nuclear Science Symposium and Medical Imaging Conference (NSS/MIC)* (2020), 1–4.

129. Orita, T. *et al.* The current mode Time-over-Threshold ASIC for a MPPC module in a TOF-PET system. *Nuclear Instruments and Methods in Physics Research Section A: Accelerators, Spectrometers, Detectors and Associated Equipment* **912,** 303–308 (2018).

130. *HGCROC2/2A Datasheet* CERN gitlab project for CMS HGCROC tests. Accessed: 2022-11-14.

131. *Geant4 documentation – Physics List Guide* https://geant4-userdoc.web.cern.ch/UsersGuides/PhysicsListGuide/html/physicslistguide.html. Accessed: 2023-02-22.

132. *The Proton Synchrotron* https://home.cern/science/accelerators/proton-synchrotron. Accessed: 2023-03-21.

133. *The Super Proton Synchrotron* https://home.cern/science/accelerators/super-proton-synchrotron. Accessed: 2023-03-21.

134. Peitzmann, T. *et al.* Results from the EPICAL-2 ultra-high granularity electromagnetic calorimeter prototype. *Nuclear Instruments and Methods in Physics Research Section A: Accelerators, Spectrometers, Detectors and Associated Equipment* **1045,** 167539 (2023).

135. *langaus.C File Reference* https://root.cern.ch/doc/v614/langaus_8C.html. Accessed: 2023-02-22.

136. Bierlich, C. *et al.* A comprehensive guide to the physics and usage of PYTHIA 8.3. *SciPost Physics Codebases.* (2022). arXiv: 2203.11601 [hep-ph].

137. Colamaria, F. D meson-hadron angular correlations in pp and p-Pb collisions with ALICE at the LHC. *Journal of Physics: Conference Series* **509,** 012103 (May 2014).

138. Workman, R. L. *et al.,* (Particle Data Group). Review of Particle Physics. *Progress of Theoretical and Experimental Physics* **2022.** 083C01 (Aug. 2022).

139. ALICE collaboration. Calibration of the photon spectrometer PHOS of the ALICE experiment. *Journal of Instrumentation* **14,** P05025 (May 2019).

140. Brun, R, Bruyant, F, Maire, M, McPherson, A. C. & Zanarini, P. *GEANT 3: user's guide Geant 3.10, Geant 3.11; rev. version* (CERN, Geneva, 1987).

141. Bierlich, C., Gustafson, G., Lönnblad, L. & Shah, H. The Angantyr model for heavy-ion collisions in Pythia8. *Journal of High Energy Physics* **2018,** 134 (Oct. 2018).

142. STAR Collaboration. Inclusive π^0, η, and direct photon production at high transverse momentum in $p+p$ and $d+$Au collisions at $\sqrt{s_{NN}} = 200$ GeV. *Physical Review C* **81,** 064904. arXiv: 0912.3838 [hep-ex] (2010).

Appendices

APPENDIX A VOLTAGE SCAN RESULTS (2022 TEST BEAM)

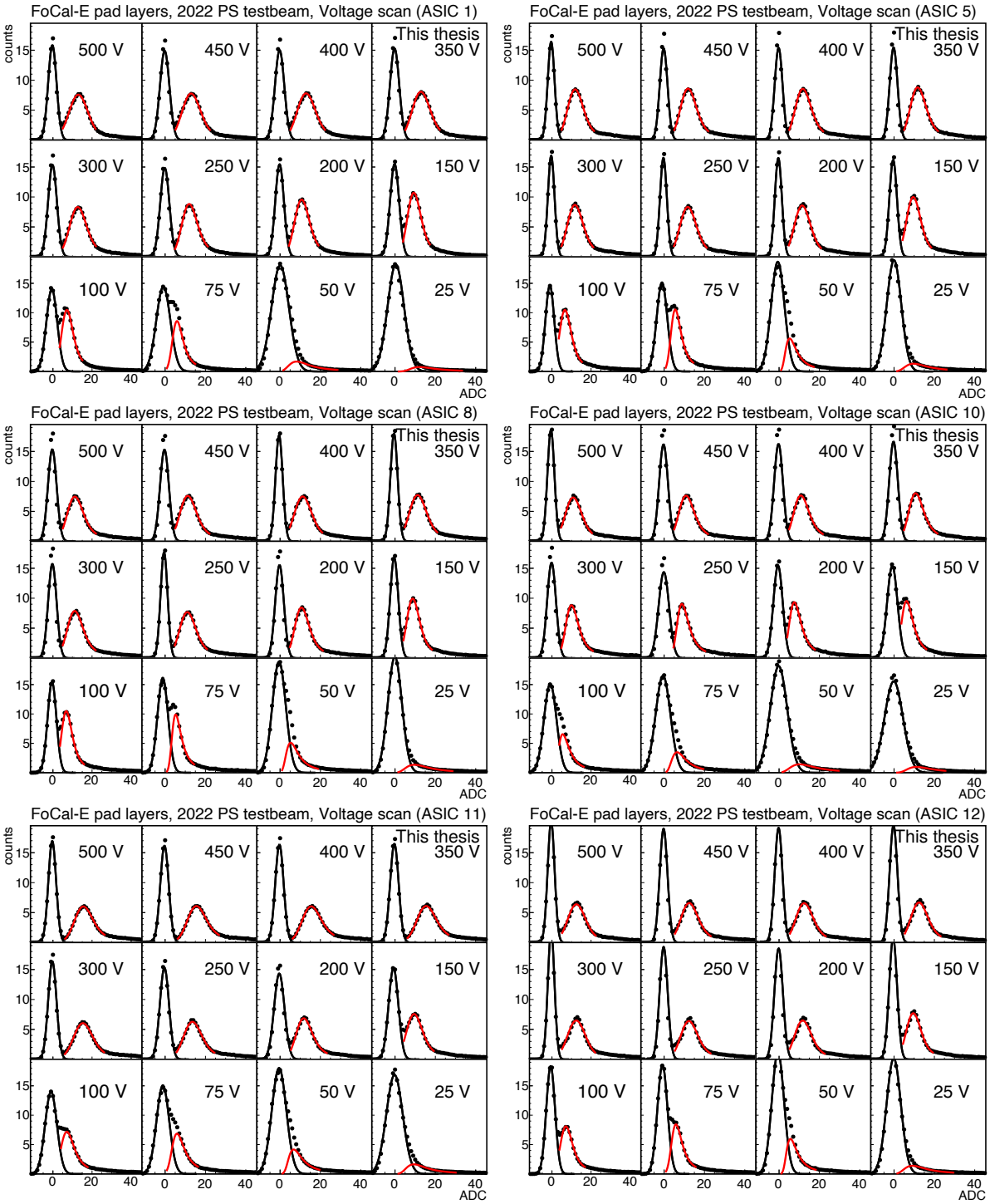

FIGURE 81 Voltage scan results after noise removal with Gaussian fit to the pedestal and Langaus to the MIP peak.

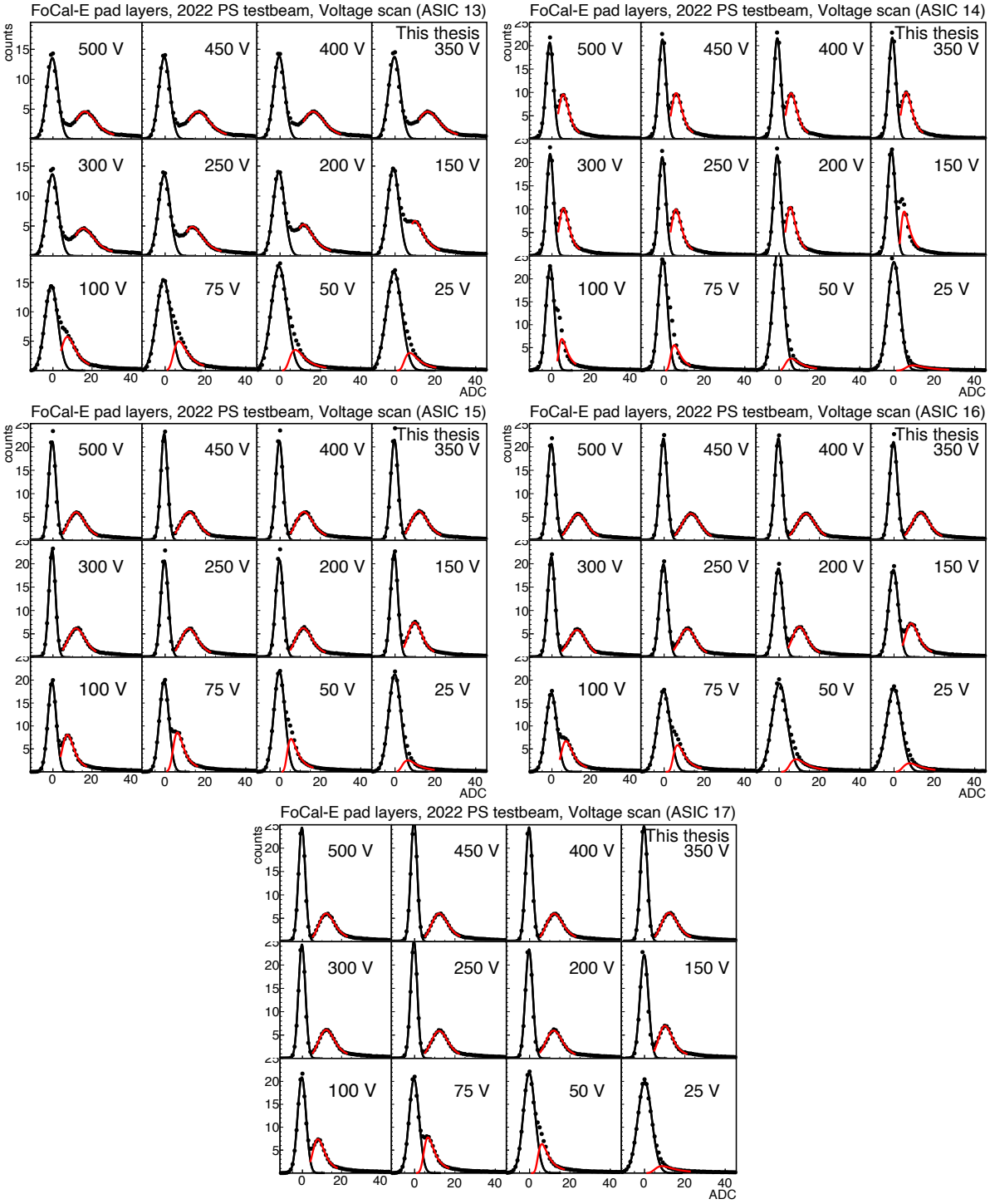

FIGURE 82 Voltage scan results after noise removal with Gaussian fit to the pedestal and Langaus to the MIP peak.

APPENDIX B POSITION SCAN RESULTS (2022 TEST BEAM)

The following figures in this appendix show the ADC distributions after noise subtractions for each channel, layer-by-layer. The layer has been indicated as the ASIC number in the header on top of each figure. In each channel the pedestal has been fitted with a Gaussian (black curve) while the MIP peak has been fitted with Landau + Gaussian (red curve). The physical channel number in the board has been printed in each panel, as well as the MIP peak position from the fit. If the data quality in a channel was poor so that the MIP peak was not visible the panel has been colored red.

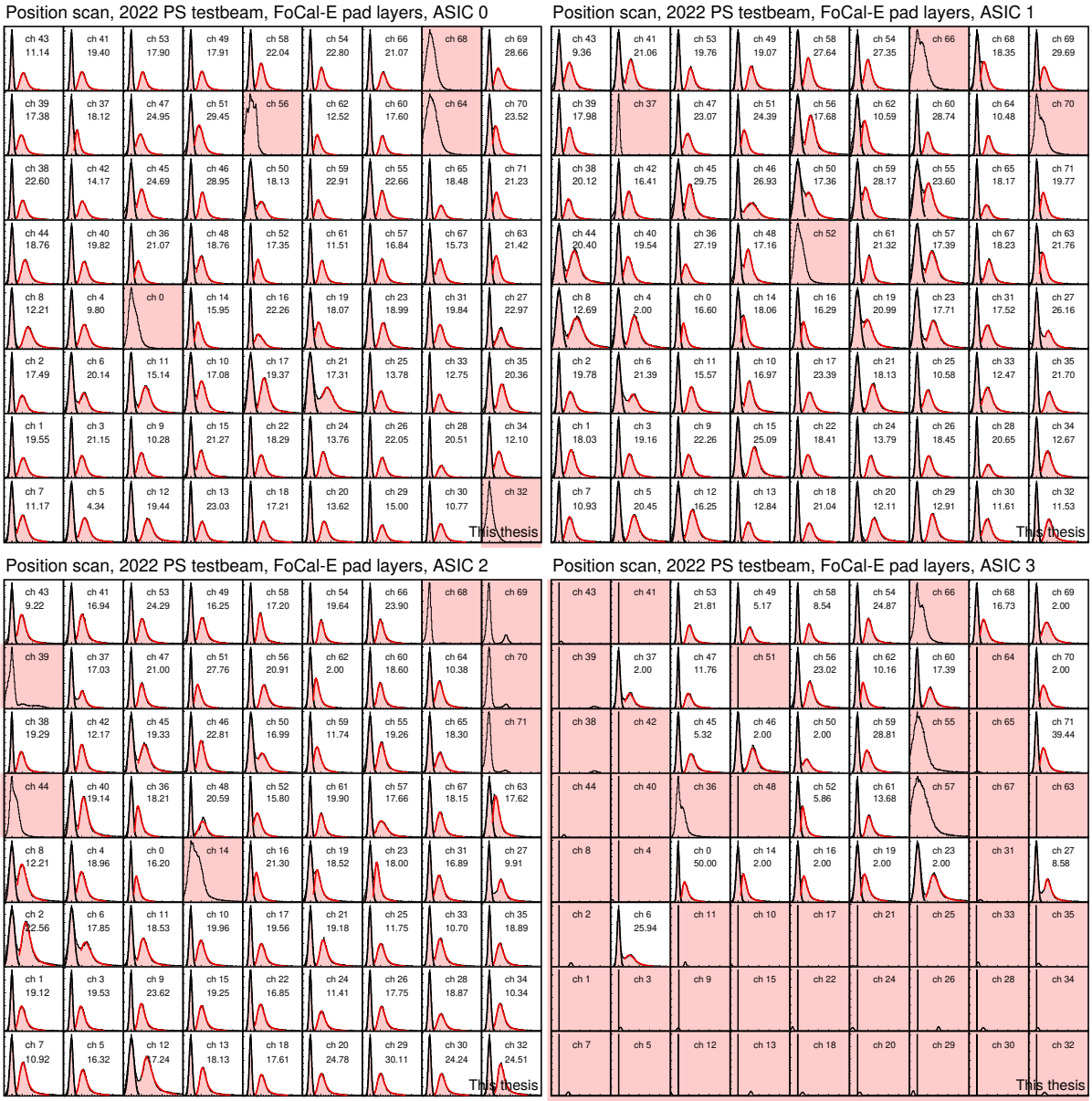

Position scan, 2022 PS testbeam, FoCal-E pad layers, ASIC 4

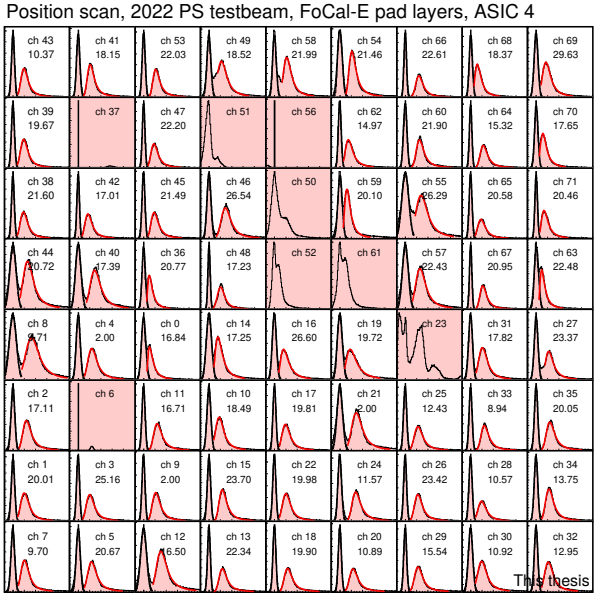

Position scan, 2022 PS testbeam, FoCal-E pad layers, ASIC 5

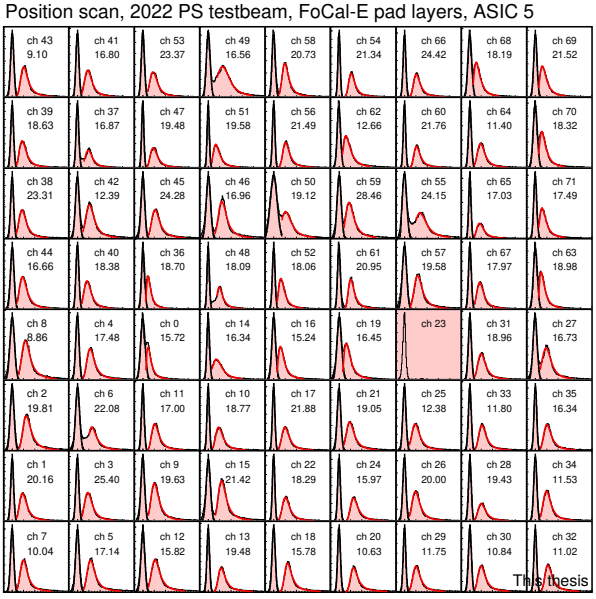

Position scan, 2022 PS testbeam, FoCal-E pad layers, ASIC 6

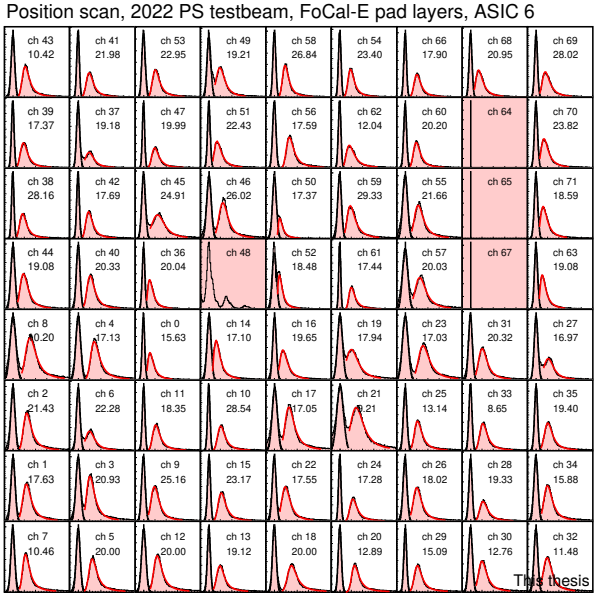

Position scan, 2022 PS testbeam, FoCal-E pad layers, ASIC 7

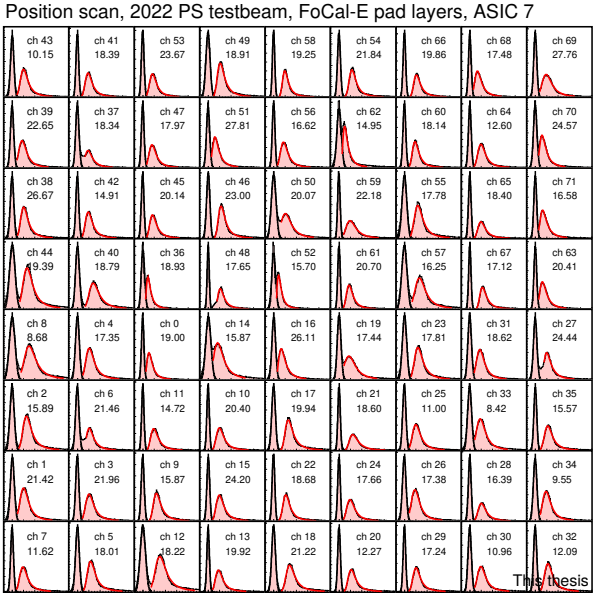

Position scan, 2022 PS testbeam, FoCal-E pad layers, ASIC 8

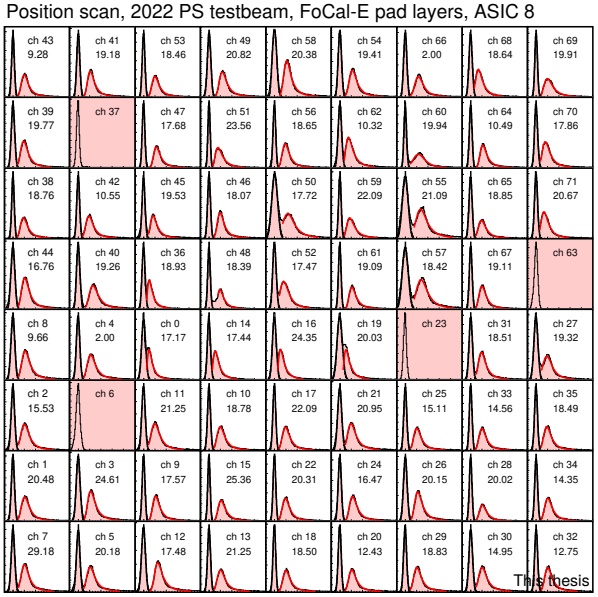

Position scan, 2022 PS testbeam, FoCal-E pad layers, ASIC 9

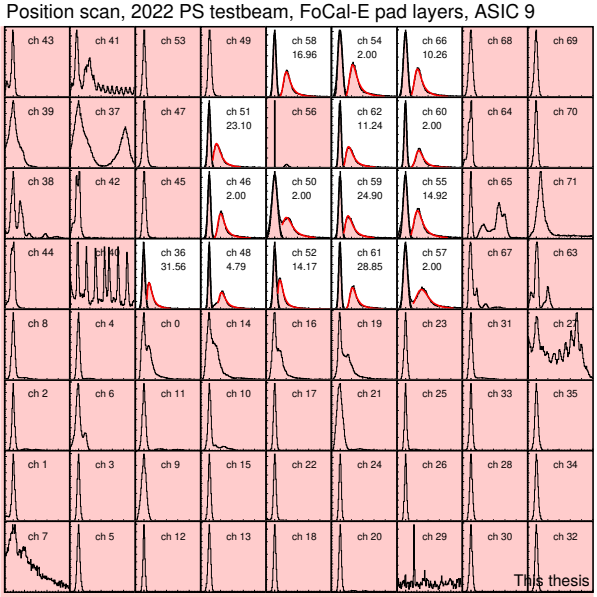

Position scan, 2022 PS testbeam, FoCal-E pad layers, ASIC 10

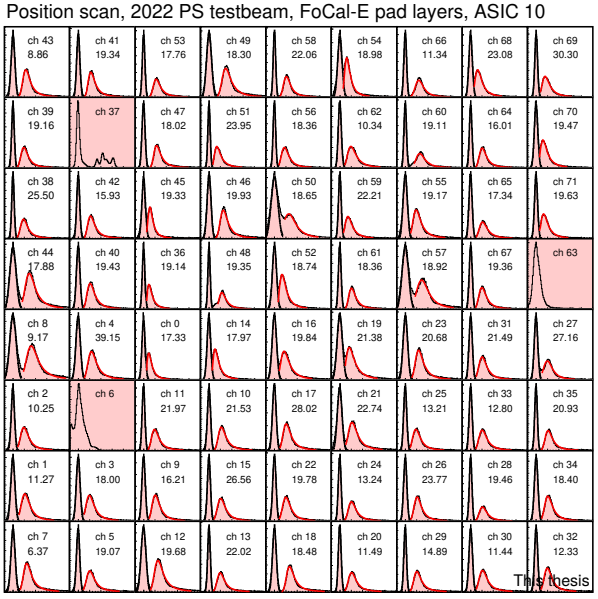

Position scan, 2022 PS testbeam, FoCal-E pad layers, ASIC 11

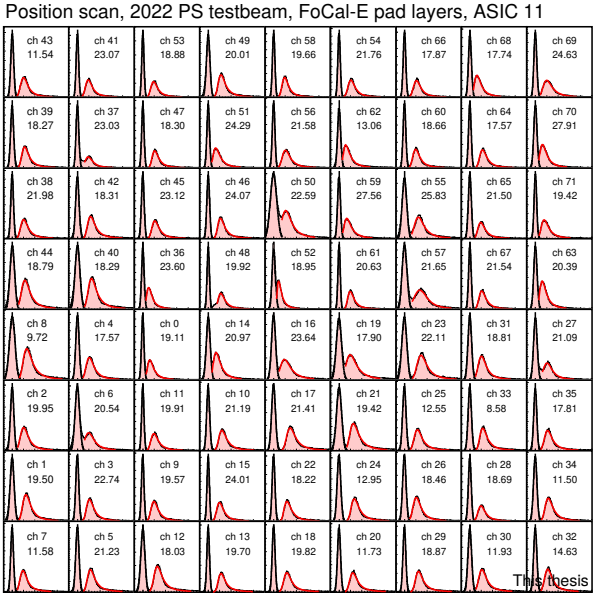

Position scan, 2022 PS testbeam, FoCal-E pad layers, ASIC 12

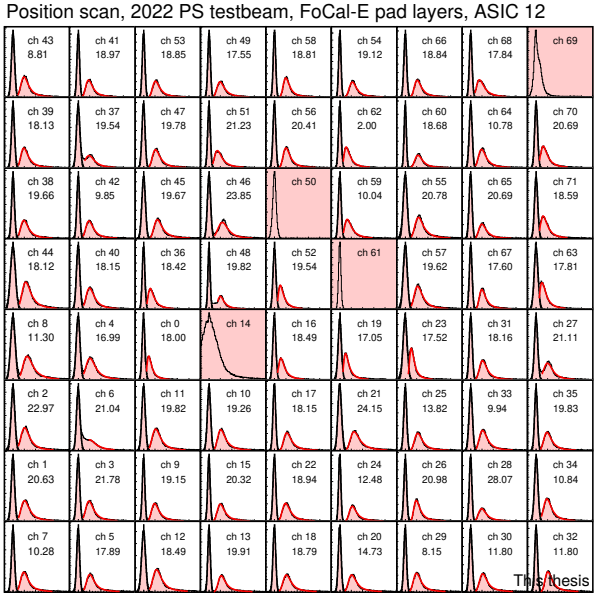

Position scan, 2022 PS testbeam, FoCal-E pad layers, ASIC 13

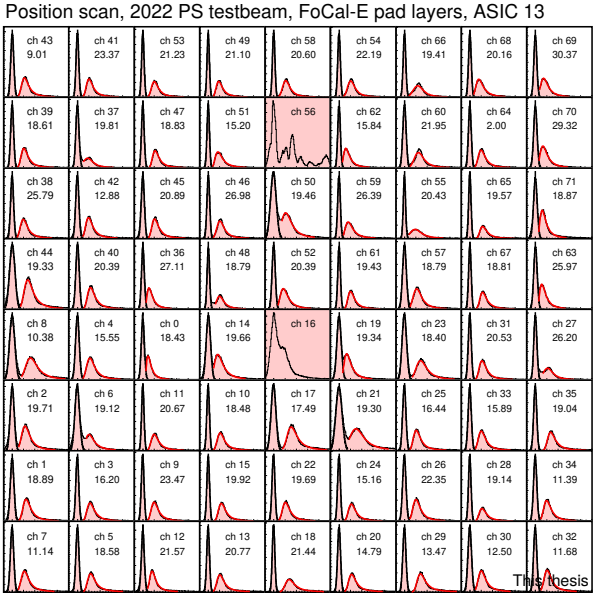

Position scan, 2022 PS testbeam, FoCal-E pad layers, ASIC 14

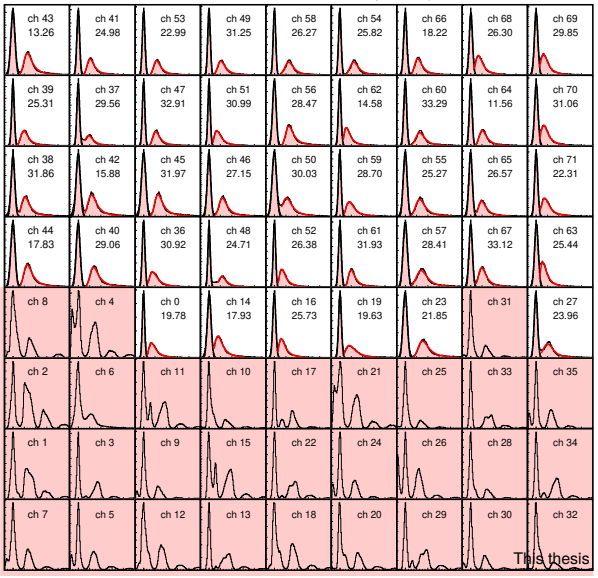

Position scan, 2022 PS testbeam, FoCal-E pad layers, ASIC 15

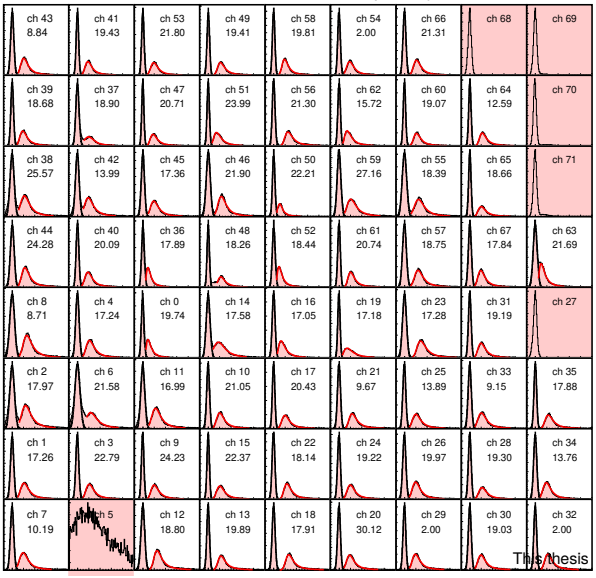

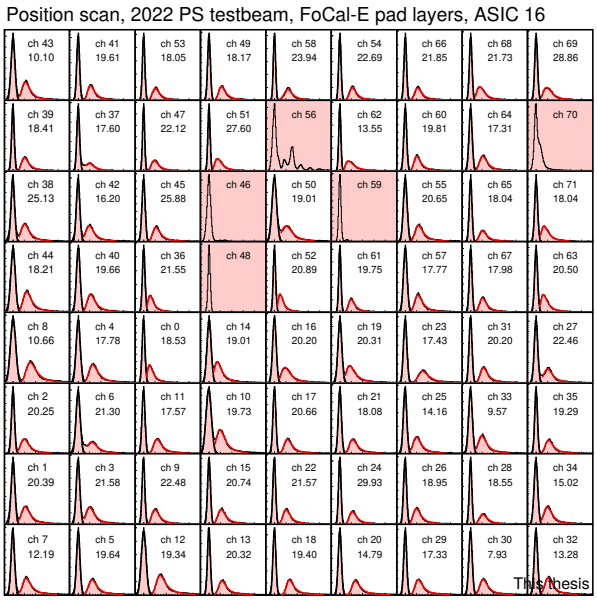
Position scan, 2022 PS testbeam, FoCal-E pad layers, ASIC 16
ch 43 10.10
ch 41 19.61
ch 53 18.05
ch 49 18.17
ch 58 23.94
ch 54 22.69
ch 66 21.85
ch 68 21.73
ch 69 28.86
ch 39 18.41
ch 37 17.60
ch 47 22.12
ch 51 27.60
ch 56
ch 62 13.55
ch 60 19.81
ch 64 17.31
ch 70
ch 38 25.13
ch 42 16.20
ch 45 25.88
ch 46
ch 50 19.01
ch 59
ch 55 20.65
ch 65 18.04
ch 71 18.04
ch 44 18.21
ch 40 19.66
ch 36 21.55
ch 48
ch 52 20.89
ch 61 19.75
ch 57 17.77
ch 67 17.98
ch 63 20.50
ch 8 10.66
ch 4 17.78
ch 0 18.53
ch 14 19.01
ch 16 20.20
ch 19 20.31
ch 23 17.43
ch 31 20.20
ch 27 22.46
ch 2 20.25
ch 6 21.30
ch 11 17.57
ch 10 19.73
ch 17 20.66
ch 21 18.08
ch 25 14.16
ch 33 9.57
ch 35 19.29
ch 1 20.39
ch 3 21.58
ch 9 22.48
ch 15 20.74
ch 22 21.57
ch 24 29.93
ch 26 18.95
ch 28 18.55
ch 34 15.02
ch 7 12.19
ch 5 19.64
ch 12 19.34
ch 13 20.32
ch 18 19.40
ch 20 14.79
ch 29 17.33
ch 30 7.93
ch 32 13.28
This thesis
Position scan, 2022 PS testbeam, FoCal-E pad layers, ASIC 17
ch 43 9.12
ch 41
ch 53
ch 49
ch 58 18.85
ch 54 24.48
ch 66 19.89
ch 68 20.10
ch 69 21.89
ch 39
ch 37
ch 47
ch 51 25.88
ch 56 18.71
ch 62 10.03
ch 60 23.13
ch 64 14.16
ch 70 22.52
ch 38 26.91
ch 42 10.45
ch 45
ch 46 27.17
ch 50
ch 59 24.92
ch 55 24.15
ch 65 16.85
ch 71 16.84
ch 44 19.47
ch 40 20.40
ch 36 22.59
ch 48 18.69
ch 52 21.89
ch 61 18.64
ch 57 18.57
ch 67 18.59
ch 63
ch 8 9.41
ch 4 2.00
ch 0 16.51
ch 14 2.00
ch 16 20.13
ch 19 2.00
ch 23 14.03
ch 31 16.92
ch 27 26.38
ch 2 10.77
ch 6
ch 11 46.12
ch 10 16.71
ch 17 24.10
ch 21 34.34
ch 25 13.17
ch 33 11.81
ch 35 2.00
ch 1 20.42
ch 3 21.10
ch 9 26.15
ch 15 18.25
ch 22 19.01
ch 24 12.13
ch 26 20.49
ch 28 20.51
ch 34 9.46
ch 7 10.00
ch 5
ch 12 18.85
ch 13 22.98
ch 18 19.84
ch 20 11.21
ch 29 13.91
ch 30 10.88
ch 32 12.95
This thesis

APPENDIX C ELECTRON SHOWERS LAYER-BY-LAYER (2022 TEST BEAM)

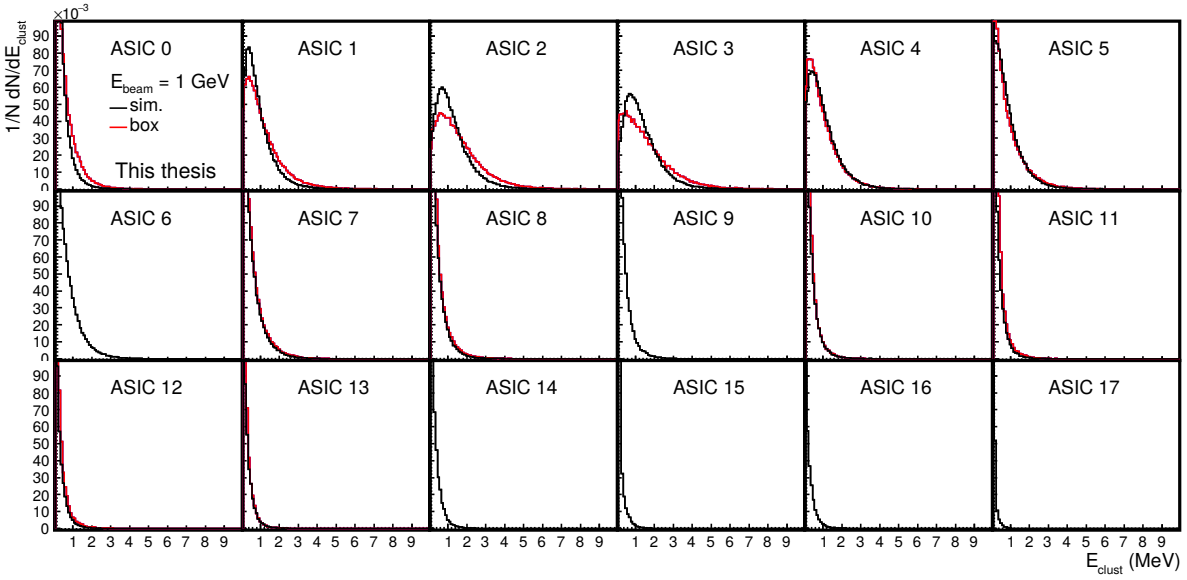

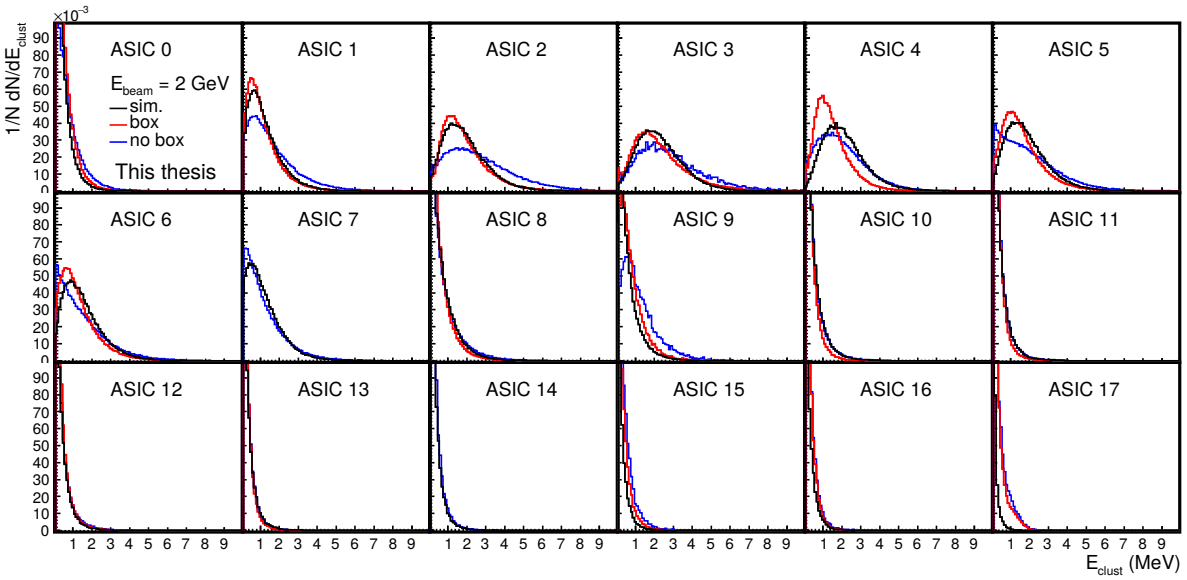

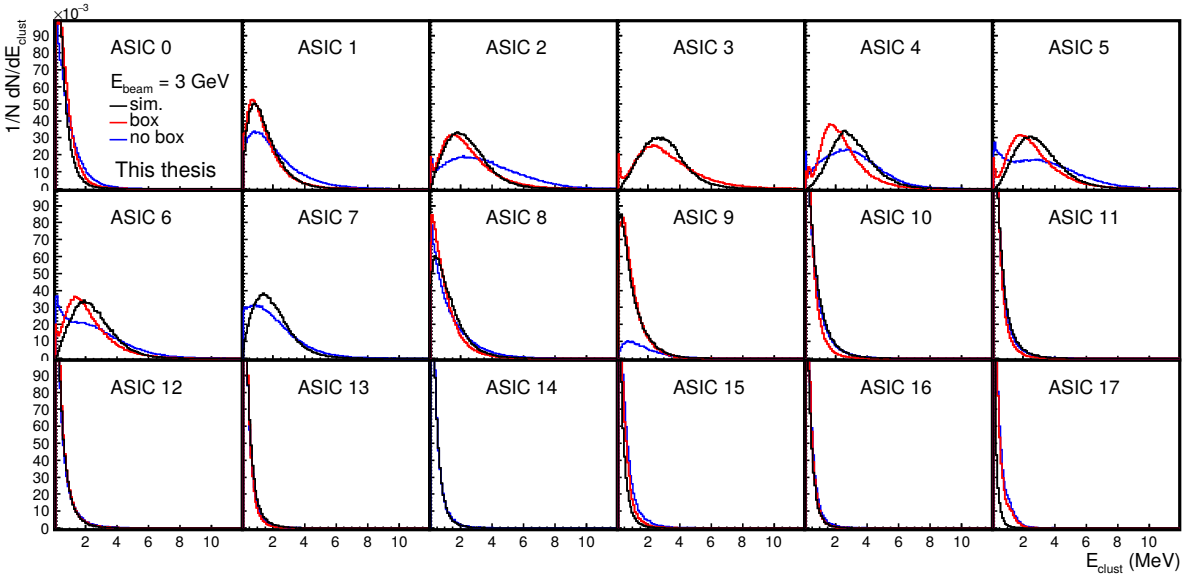
1/N dN/dE_clust
×10^-3
ASIC 0
E_beam = 3 GeV
sim.
box
no box
This thesis
ASIC 1
ASIC 2
ASIC 3
ASIC 4
ASIC 5
ASIC 6
ASIC 7
ASIC 8
ASIC 9
ASIC 10
ASIC 11
ASIC 12
ASIC 13
ASIC 14
ASIC 15
ASIC 16
ASIC 17
E_clust (MeV)

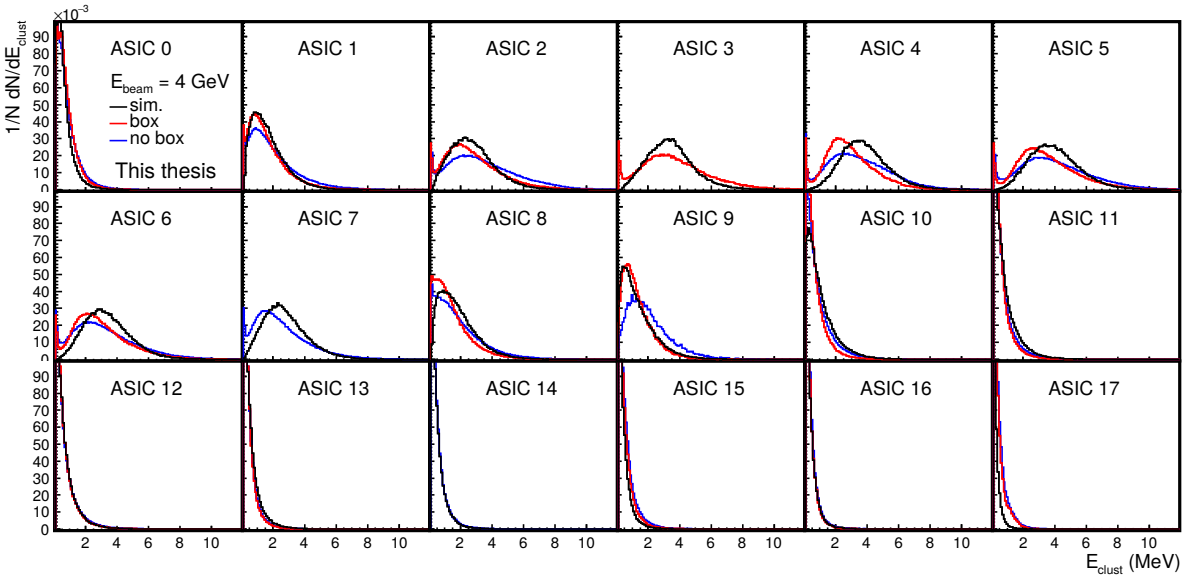
1/N dN/dE_clust
×10^-3
ASIC 0
E_beam = 4 GeV
sim.
box
no box
This thesis
ASIC 1
ASIC 2
ASIC 3
ASIC 4
ASIC 5
ASIC 6
ASIC 7
ASIC 8
ASIC 9
ASIC 10
ASIC 11
ASIC 12
ASIC 13
ASIC 14
ASIC 15
ASIC 16
ASIC 17
E_clust (MeV)